Doctoral Thesis

A Study on Charge Transport and Recombination Properties for Organic Photovoltaic Devices

Song Yi Park

Department of Energy Engineering

(Energy Engineering)

Graduate School of UNIST

2020

A Study on Charge Transport and Recombination Properties for Organic Photovoltaic Devices

Song Yi Park

Department of Energy Engineering

(Energy Engineering)

Graduate School of UNIST

A Study on Charge Transport and Recombination Properties for Organic Photovoltaic Devices

A thesis/dissertation

submitted to the Graduate School of UNIST

in partial fulfillment of the

requirements for the degree of

Doctor of Philosophy

Song Yi Park

11/25/2019 of submission

Approved by

_____

Advisor

Jin Young Kim

A Study on Charge Transport and Recombination Properties for Organic Photovoltaic Devices

Song Yi Park

This certifies that the thesis/dissertation of Song Yi Park is approved.

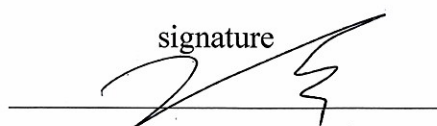11/25/2019 of submission

signature

Advisor: Jin Young Kim

signature

Myoung Hoon Song: Thesis Committee Member #1

signature

Tae-Hyuk Kwon: Thesis Committee Member #2

signature

Han Young Woo: Thesis Committee Member #3

signature

Jung Hwa Seo: Thesis Committee Member #4;

Abstract

Now organic solar cells exhibited excellent device performance with power conversion efficiency over 16%. Therefore, it has a great potential for various practical application such as large-area flexible devices, indoor photovoltaic applications, colorful devices, and so on. Fundamental study is important for further development of organic solar cells. Charge carrier recombination and transport properties should be investigated which is related to the photocurrent and/or energy losses leading to poor device performance. This thesis deals with a relationship between solvent additives, morphology and bimolecular recombination by using diphenyl ether and diphenyl sulfide as universal and non-halogenated solvent processing additives.(Chapter 2 and 3) Diphenyl ether acts like theta solvent to photovoltaic polymers, helps to form ideal bulk-heterojunction film morphologies and suppress bimolecular charge recombination regardless photovoltaic polymers. Diphenyl sulfide exhibited fast and field-independent photocurrent saturation with negligible bimolecular recombination led to efficient charge separation and collection, which resulted in the highest power conversion efficiency up to 9.08% in PTB7-Th:PC$_{71}$BM devices. Charge recombination and transport characteristics are different with incident light intensities. In chapter 4, device properties are investigated under various light intensities with three semi-crystalline polymers by modulating the intra- and intermolecular noncovalent coulombic interactions. With the polymers which exhibited compact molecular packing structures, high power conversion efficiency was achieved even in low light intensity. P2FDTBT$_{BO}$ devices exhibited a low efficiency of 3.69% under standard light. However the efficiency was dramatically enhanced by 2.3 times (8.33% PCE) under dim light, showing negligible decrease in open-circuit voltage and remarkable increase in fill factor, which is due to the exceptionally high R_{sh} of over 1000 kΩ cm^2. This work provides an important tips to further optimize organic solar cells for indoor applications with low-power electronic devices such as Internet of Things (IoT) sensors, etc. Conventional bulk-heterojunction (BHJ) organic solar cells (OSCs) generally guarantee high power conversion efficiency, but poor reproducibility of active layer's morphologies and complicated device optimization processes limit further commercialization. In chapter 5, bilayer organic solar cells (OSCs) are characterized with 5 different non-fullerene acceptors which are distinguished by Stokes shift. Bilayer-heterojunction was formed using orthogonal solvent system for donor and acceptor, and it was confirmed by various experimental techniques. ITIC-Th1, IDIC and its derivatives (Stokes shift 38~74 nm) exhibits 9-11% PCEs in bilayer-heterojunction OSCs with high fill factor ~0.70, whereas NIDCS-HO (Stokes shift 133 nm) exhibits poor PCE around 2%. The high efficiencies were enabled by their efficient self Föster energy transfer (FRET) with long exciton diffusion lengths (20-30 nm), and long-range FRET from donor to acceptor (with significant spectral overlap between emission of donor and absorption of acceptor). The bilayer devices have negligible bimolecular and monomolecular recombination. This work suggest that small Stokes shift materials have a great potential for high-performance bilayer OSCs with long exciton diffusion lengths.

Table of Contents

List of Figures

List of Tables

List of Abbreviations

Abbreviation	Description
OSC	organic solar cell
PCE	power conversion efficiency
BHJ	bulk-heterojunction
HTL	hole transport layer
ETL	electron transport layer
PCBM	phenyl-c$_{61}$-butyric acid methyl ester
AM	air mass
HOMO	highest occupied molecular orbital
LUMO	lowest unoccupied molecular orbital
EQE	external quantum efficiency
IQE	internal quantum efficiency
CT	charge transfer
NW	nanowire
PEDOT:PSS	poly(3,4-ethylenedioxythiophene) polystyrene sulfonate
SRH	shockley-read-hall
SCLC	space-charge-limited current
TFL	trap-filled limit
TOF	tome-of-flight
FET	field-effect transistors
CELIV	charge extraction by linearly increasing voltage
PSC	polymer solar cell
PC$_{71}$BM	[6,6]-phenyl-c$_{71}$-butyric acid methyl ester
DIO	1,8-diiodoocatne
ODT	1,8-octanedithiol
CN	1-chloronaphthalene
DPE	diphenyl ether
PTB7	poly[[4,8-bis[(2-ethylhexyl)oxy]benzo[1,2-b:4,5-b']dithiophene-2,6-diyl][3-fluoro-2-[(2-ethylhexyl)-carbonyl]thieno-[3,4-b]thiophenediyl]]
PPDT2FBT	poly[(2,5-bis(2-hexyldecyloxy)phenylene)-*alt*-(5,6-difluoro-4,7-di(thiophen-2-yl)benzo[c][1,2,5]-thiadiazole)]
CB	chlorobenzene
P3HT	poly(3-hexylthiophene)
PBDTTPD	poly(di(2-ethylhexyloxy)benzo[1,2-*b*:4,5-*b'*]dithiophene-*co*-octylthieno[3,4-*c*]pyrrole-4,6-dione)

PCDTBT	poly[n-9'-heptadecanyl-2,7-carbazole-*alt*-5,5-(4,7-di-2-thienyl-2',1',3'-benzothiadiazole]
RMS	root mean square
AFM	atomic force microscopy
GIWAXS	grazing incidence wide angle x-ray scattering
TCB	1,2,4-trichlorobenzene
TMB	1,2,4-trimethylbenzene
PDFQx-3T	poly(2,2′:5′,2′′-terthiophene-*alt*-2,3-bis(3,4-bis(octyloxy)phenyl)-6,7-difluroquinoxaline
DPS	diphenyl sulfide
DPSe	diphenyl selenide
DPX	diphenyl chalcogenide
PTB7-Th	poly[4,8-bis(5-(2-ethylhexyl)thiophen-2-yl)benzo[1,2-b:4,5-b′]dithiophene-co-3-fluorothieno[3,4-b]thiophene-2-carboxylate]
MeOH	methanol
IoT	Internet of Things
BT	benzothiadiazole
PTTBT$_{BO}$	poly(5,6-bis(butyloctyloxy)-4-(thieno[3,2-b]thiophene-2-yl)-benzo[*c*][1,2,5]thiadiazole)
PDTBT$_{BO}$	poly(5,6-bis(butyloctyloxy)-4-(2,2′-bithiophene-5-yl)-benzo[*c*][1,2,5]thiadiazole)
P2FDTBT$_{BO}$	poly(5,6-bis(butyloctyloxy)-4-(3,3′-difluoro-2,2′-bithiophene-5-yl)-benzo[*c*][1,2,5]thiadiazole)
ITIC	3,9-bis(2-methylene-(3-(1,1-dicyanomethylene)-indanone))-5,5,11,11-tetrakis(4-hexylphenyl)-dithieno[2,3-d:2′,3′-d′]-s-indaceno[1,2-b:5,6-b′]dithiophene
PDI	polydispersity index
GPC	gel permeation chromatography
TGA	thermogravimetric analysis
DSC	differential scanning calorimetry
CV	cyclic voltammetry
PBDB-T-2F	poly[(2,6-(4,8-bis(5-(2-ethylhexyl-3-fluoro)thiophen-2-yl)-benzo[1,2-b:4,5-b']dithiophene))-alt-(5,5-(1',3'-di-2-thienyl-5',7'-bis(2-ethylhexyl)benzo[1',2'-c:4',5'-c']dithiophene-4,8-dione)]
IDIC	indacenodithiophene endcapped with 1,1-dicyanomethylene-3-indanone
IDICO1	2,2'-((2z,2'z)-((4,4,9,9-tetrahexyl-4,9-dihydro-s-indaceno[1,2-b:5,6-b']dithiophene-2,7-diyl)bis(methaneylylidene))bis(5-octyl-3-oxo-2,3-dihydro-1h-indene-2,1-diylidene))dimalononitrile

IDICO2	2,2'-((2z,2'z)-((4,4,9,9-tetrahexyl-4,9-dihydro-s-indaceno[1,2-b:5,6-b']dithiophene-2,7-diyl)bis(methaneylylidene))bis(6-octyl-3-oxo-2,3-dihydro-1h-indene-2,1-diylidene))dimalononitrile
NIDCS-HO	(2e,2′e)-3,3′-(2,5-bis(hexyloxy)-1,4-phenylene)bis(2-(5-(4-(n-(2-ethylhexyl)-1,8-naphthalimide)yl)-thiophen-2-yl)acrylonitrile)
TEM	transmission electron microscopy
DCM	dichloromethane
SS	Stokes shift
FRET	Förster Resonance Energy Transfer

Chapter 1. Introduction

1.1 Organic Solar Cells (OSCs)

Sunlight, infinite energy resource, can be converted into electricity using solar cells. The solar power generation system is sustainable, environmental-friendly and safe, so this energy conversion system has been attracted a great attention over the past decades. Solar cells basically consist of semiconductors. Representative inorganic photovoltaic semiconductors are Si, Ge and GaAs which provide ~20% of power conversion efficiencies (PCEs) on average in solar panels. Organic semiconductors including conjugated polymers and small molecules also can be utilized as photovoltaic materials, and this device is called as organic solar cell (OSC). Organic semiconductors have many strengths compared to inorganic semiconductors; 1) easily tunable band gap by designing molecule's structures, 2) light weight, 3) solution processible (low production cost), 4) flexible, 5) semi-transparent, and so on.

In 1986, first successful organic solar cells were demonstrated by Tang. Active layer was bilayer structure with CuPc and PV molecules deposited by vacuum evaporation, and PCE was 0.95% with high fill factor (FF) of 0.65.[1] Using C_{60} and its derivatives (phenyl-C_{61}-butyric acid methyl ester (PCBM)) as an acceptor material, PCEs were greatly improved in OSCs. In 1992-1993, ultrafast photoinduced electron transfer in conducting polymer, MEH-PPV, and fullerene (C_{60}) was demonstrated by F. Wudl and A. J. Heeger groups.[2-3] After 2 years later, bulk-heterojunction (BHJ) concept was suggested to overcome limited exciton diffusion length problem of organic semiconductors.[4-5] In 2001, 2.5% PCE was demonstrated using MDMO-PPV and PCBM.[6] To further optimization of donor and acceptor's domain interfaces, small amount of solvent processing additives (such as 1,8-octanedithiol and 1,8-diiodooctane) were introduced in solution of active layer leading to greatly improved short-circuit current density (J_{SC}), fill factor (FF) and PCEs.[7-8]

New device architectures also have been suggested to improve device performance such as introduction of optical spacer, tandem solar cells, ternary blend solar cells, etc. In 2006, efficient polymer solar cells (PSCs) was demonstrated by introducing solution based TiO_x as optical spacer. With TiO_x, J_{SC} was greatly improved by ~50% (7.5 to 11.1 mA cm^{-2}) which contributed by optical interference effect.[9] In 2007, J. Y. Kim *et al.* reported efficient tandem polymer solar cells (PSCs) with 6.2% of PCEs by introducing 'inverted tandem cell' structures of low band-gap BHJ (PCPDTBT:PCBM) as front cell and higher band-gap BHJ (P3HT:PCBM) as back cell with TiO_x as intermediate layer.[10] In addition, ternary blend BHJ solar cells have been a great attention to achieve high PCEs with complementary absorption by third components.[11-12]

Recently, high-performance OSCs with >16% PCE were reported with non-fullerene acceptors.[13-14] These results suggest that OSCs still have more room and great potential to further optimization and

commercialization.

1.1.1 Working Principle of OSCs

OSCs basically consist of electrodes, hole and electron transport layers (HTL and ETL, respectively) and active layer as shown in **Figure 1. 1a** and **1b**. While all components are essential to achieve high PCEs, active layer is most key part in OSCs. Two components of electron donor and acceptor are needed to generate charge carriers efficiently. Generally, conjugated polymers and small molecules (fullerene or non-fullerene) are used as donor and acceptor materials, and molecular structures of representative materials are shown in **Figure 1. 1c**. Device operation processes of OSCs consist of 4 steps; 1) exciton generation, 2) exciton diffusion, 3) exciton dissociation into charge carriers and 4) charge carrier collection, and these processes are summarized in **Figure 1. 2**.
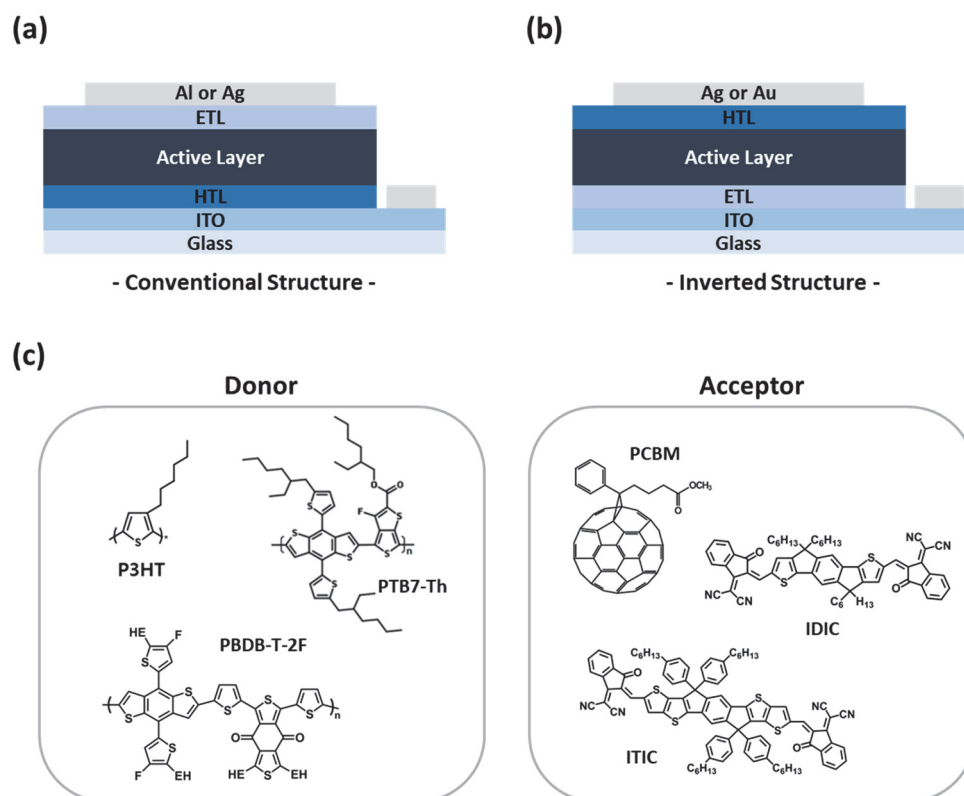
Figure 1. 1. Device structures of OSCs - (a) Conventional structure and (b) inverted structure. (c) Representative donor and acceptor materials.

When the light is incident into organic semiconductors, 'exciton' is created which is also expressed as electron-hole pairs bound by electrostatic Coulomb force. Excitons can be created when the material absorbs photons with higher energy than bandgap.

Then excitons diffuse in donor or acceptor phases. Since exciton diffusion length (L_D) of organic semiconductors (typically conjugated polymers) is around 10 nm, bilayer-heterojunction OSCs have limitations to achieve high PCEs. BHJ OSCs are one of excellent solutions to overcome such short L_D problem. Due to randomly mixed states of donor and acceptor molecules in BHJs, generated excitons efficiently diffuse to donor and acceptor interfaces before recombination.

Exciton binding energy of organic semiconductors is around 0.3~0.5 eV, because the materials typically have low relative dielectric constants from 2 to 4.[15] This binding energy is not sufficient to dissociate into charge carriers at room temperature, so appropriate electron accepting material is needed which have energy difference of lowest unoccupied molecular orbital (LUMO) or highest occupied molecular orbital (HOMO) levels. When excitons reach to the donor and acceptor interfaces, they are dissociated into free charge carriers due to energy difference of LUMO levels of donor and acceptor. (In case of excitons generated in A, they are dissociated into free charge carriers by energy difference of HOMO levels of donor and acceptor.) Then, the charge carriers are collected to each electrode.
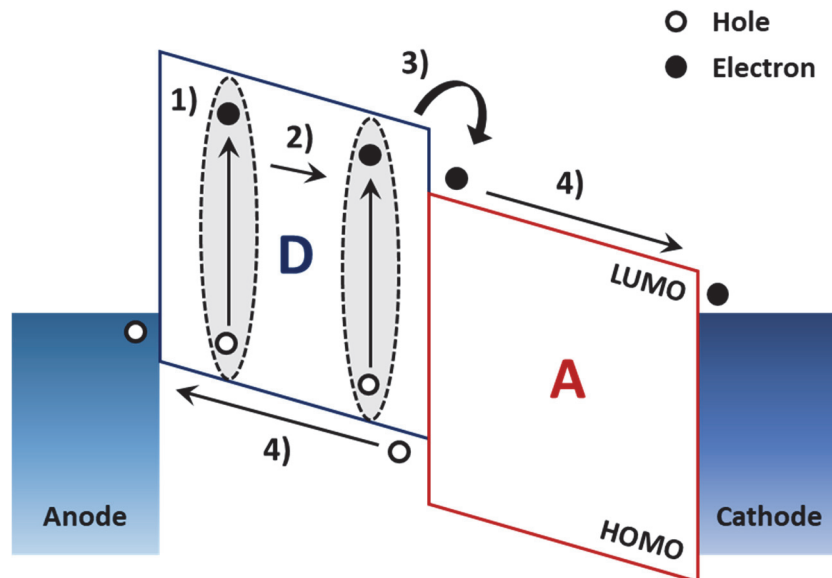
Figure 1. 2. Device operation processes of OSCs. 1) Exciton generation, 2) Exciton diffusion, 3) Exciton dissociation into free charge carriers and 4) charge carrier collection to the electrodes.

1.1.2 Characterization of OSCs

When the sunlight passes through the atmosphere of the earth, it is attenuated by scattering and absorption; most active component of absorption of certain wavelength is water vapor which leads to a wide variety of absorption band at many wavelengths. (Nitrogen, oxygen and carbon dioxide molecules also contribute to this process.) Scattering atmosphere of sunlight plays a role in removing higher frequencies from direct sunlight. As a result, the solar spectrum is strongly confined between far infrared and near ultraviolet. Considering the attenuation of sunlight by scattering and absorption, concept of 'air mass coefficient' is suggested that defines the direct optical path length through the earth's atmosphere, expressed as a ratio relative to the path length at the zenith. To characterize solar cells, solar spectrum of 'AM1.5G' is commonly used as standardized conditions with light intensity of 100 mW cm^{-2}. The solar irradiance spectrum of AM1.5G and AM1.0 are shown in **Figure 1.3**.
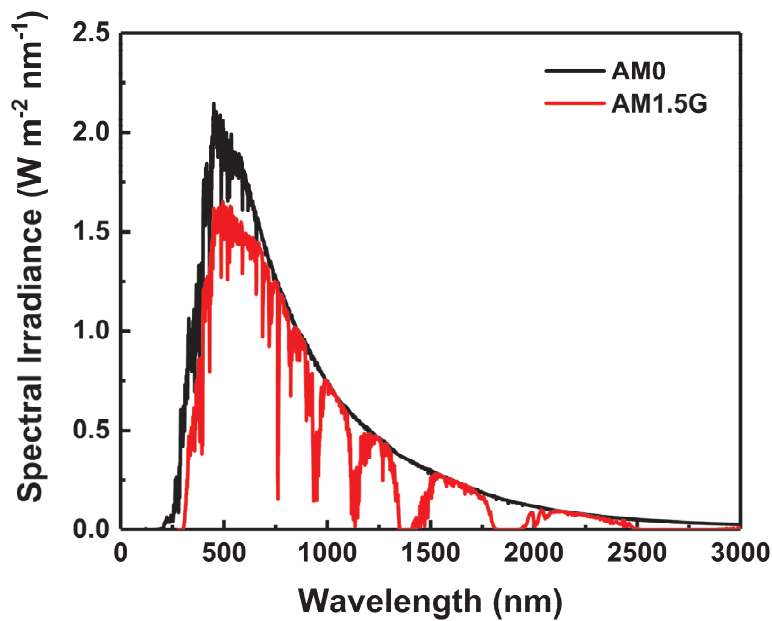
Figure 1. 3. Solar irradiance spectrum.

Power conversion efficiency (PCE) of solar cell is determined by ratio of maximum power (P_{max}) divided by incident power (P_{in}) from measuring current density–voltage (*J-V*) under AM1.5G light illumination. From the *J-V* measurements, three parameters can be obtained: short-circuit current density (J_{SC}, current density at 0 V), open-circuit voltage (V_{OC}, voltage at $J = 0$ mA cm^{-2}) and fill factor (FF). PCE can be expressed by equation (Eq.) 1-1, and typical *J-V* curve is shown in **Figure 1.4a**. Total
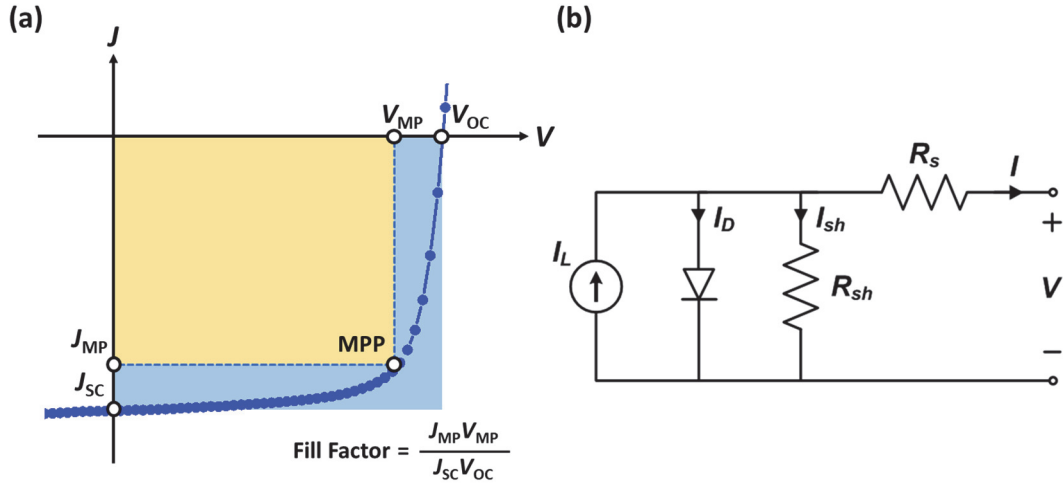
Figure 1. 4. (a) Typical *J-V* characteristics measured under AM1.5G and (b) equivalent circuit of solar cell.

$$\eta = \frac{P_{max}}{P_{in}} = \frac{J_{SC}\,V_{OC}\,FF}{P_{in}} \qquad (1\text{-}1)$$

output current density (thus, *J*) is expressed by $J_{ph} - J_D - J_{sh}$, where J_{ph} is photogenerated current density, J_D is diode current density and J_{sh} is shunt current density, and corresponding equivalent circuit of solar cell is shown in **Figure 1.4b**. *J-V* relationship of solar cell can be expressed with modified Shockley diode equation:

$$J = J_s \left[\exp\left(\frac{q(V - JR_s A)}{nkT}\right) - 1\right] + \frac{V - JR_s A}{R_{sh} A} - J_{ph} \qquad (1\text{-}2)$$

where J_s is saturation current density of the diode, *n* is the ideality factor, *k* is the Boltzmann constant, *A* is the device area, R_s is series resistance, R_{sh} is shunt resistance. Series and shunt resistance are related to the internal resistance of the photovoltaic devices as shown in **Figure 1.4b**.

Intrinsic diode properties of OSCs can determine overall device performance. In dark *J-V* curve (**Figure 1.5**), current flow shape can be divided by three regions; current flows dominantly through R_{sh} and R_s, and current injection (diode). To avoid leakage current, R_{sh} should be high. For efficient current injection, R_s should be low. Therefore high rectification ratio with high R_{sh} and low R_s from dark *J-V* curve generally provides high PCEs without leakage current and any resistance effect in forward bias,

respectively.
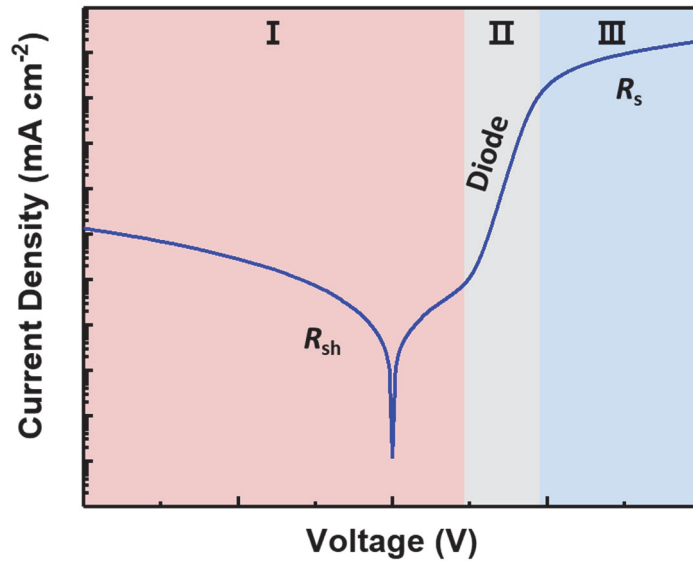
Figure 1. 5. Typical dark *J-V* curve which is divided by three regions; current flows dominantly through (I) shunt resistance (R_{sh}) and (II) series resistance (R_s), and (III) current injection (diode).

External and internal quantum efficiency (EQE and IQE, respectively) are important Figure of merit of the photovoltaic devices. EQE the ratio of the number of extracted charge carriers into electrodes to the number of incident photons. IQE is the ratio of the number of the extracted charge carriers to the number of absorbed incident photons in active layer. They can be expressed by Eq. (1-3);

$$EQE = \frac{electrons/sec}{photons/sec}, \; IQE = \frac{electrons/sec}{absorbed \; photons/sec} \tag{1-3}$$

For the ideal devices, IQE can reach to the 100% which means once a photon is absorbed, generated exciton is efficiently separated into hole and electron, and collected to electrodes without any recombination. IQE is always higher than EQE. These parameters can be measured with following equations;

$$EQE = \frac{(current)/(charge\ of\ one\ electron)}{(total\ power\ of\ photons)/(energy\ of\ one\ photon)}, \quad IQE = \frac{EQE}{1 - Reflectance} \qquad (1\text{-}4)$$

Both EQE and IQE depend on the light absorption and charge collection. Total area of EQE spectrum is proportional to J_{SC} which can be calculated by integral of multiplication of photon flux and EQE as a function of wavelengths (which depend on material's absorption spectrum). Detail of this relationship is expressed by Eq. (1-4);

$$J_{SC} = q \int_{\lambda_{min}}^{\lambda_{max}} \Phi(\lambda) EQE(\lambda) d\lambda \qquad (1\text{-}5)$$

where $\Phi(\lambda)$ is the photon flux of solar spectrum. The calculated J_{SC} from EQE is usually used to verify whether J_{SC} from J-V curve is measured correctly or not.

1.1.3 Various Strategies to Achieve High PCE in OSCs

Three parameters of J_{SC}, V_{OC} and FF determine device performance of OSCs. In this section, various strategies are discussed to achieve high PCE in OSCs, although all three parameters correlate each other.

Firstly, J_{SC} is basically related to the number of incident photons and dissociated charge carriers. With regard to the number of incident photons, using small bandgap photovoltaic material is most simple way to achieve high photocurrent.[14, 16] In addition, introduction of metal nanoparticles (typically Ag, Au or Cu) in the devices also can enhance J_{SC} due to enhanced electric field by surface plasmon resonance effect leading to increase the number of incident photons.[17-19] With regard to the number of dissociated charge carriers, interfacial area between donor and acceptor molecules affect device performance, especially J_{SC}. Since organic semiconductors typically have short L_D, large interfacial area between donor and acceptor can help to efficient exciton diffusion and dissociation before monomolecular recombination. Introduction of small amount of solvent processing additive in solution of active layer is most facile and effective method to enlarge the interfacial area.[20-21] Solvent processing additive should have higher boiling point than host solvent and selectively soluble properties of donor and acceptor molecules. This property provides finely modulated internal morphologies of active layer leading to dramatically enhanced PCE including J_{SC}. Thermal annealing and solvent vapor annealing

method are also effective methods to control film morphologies.

V_{OC} of OSCs is defined by energy difference of electron and hole quasi-Fermi levels (E_{Fn} and E_{Fp}, respectively), thus $V_{OC} = (1/q)(E_{Fn} - E_{Fp})$. Quasi-Fermi level of electron is located below LUMO level of acceptor and quasi-Fermi level of hole is located above HOMO level of donor. Therefore, intrinsically, choosing proper combination of donor and acceptor can provide high V_{OC}; low HOMO and high LUMO levels for donor and acceptor, respectively. There are a lot of factors affect V_{OC} such as carrier density, charge transfer (CT) states, work function of electrodes, recombination, donor/acceptor interface area, morphology, and so on.[22] Minimizing energy loss is a key factor to maximize V_{OC}, so it depends on the intrinsic properties of photovoltaic material. To avoid V_{OC} losses, it is a key factor that to reduce density of trap states *via* morphology control for well phase separation of active layer. Lifetime of CT states is also highly related to V_{OC}, and increasing lifetime of CT states can improve V_{OC}.

FF represents how "square" *J-V* curve is. In other words, FF is related to how difficultly or easily photogenerated carriers can be extracted to the electrodes, so high FF usually guarantees the quality of photovoltaic devices. Current injection (diode characteristics), R_s and R_{sh} highly correlate with FF. If R_{sh} is low, currents tend to flow through the R_{sh} in reverse bias instead of actual device. In addition, if R_s is high, currents also cannot flow well in forward bias. (Details are shown in **Figure 1.4b** of equivalent circuit) Therefore to obtain "square" *J-V* (thus, high FF), high R_{sh} and low R_s is essential. Unintended leakage current usually occurs when the devices have shorting problem. Due to high absorption coefficient, ~100 nm thick active layer is enough to absorb whole incident light in case of OSCs. Thickness of HTL or ETL is typically around 10-30 nm. Therefore roughness of substrates or bottom electrode should be low below a few ten nm to prevent shortage. Indium tin oxide (ITO) is generally used as transparent bottom electrode in OSCs, and ITO rarely shows shortage problem. However in case of Ag nanowires (NWs) which also representative transparent electrode, if surface roughness of Ag NWs is too rough and peak height greater than 100 nm, the devices are easily shorted, resulting in huge current loss originated by leakage current. Buffer layer, thus HTL and ETL, plays an important role. Due to BHJ structures in OSCs, both donor and acceptor materials directly contact with electrodes resulting in undesirable recombination near electrodes. Due to such recombination (high R_s), currents cannot flow efficiently leading to lowering FF. Therefore appropriate buffer layers is needed to achieve high FF, and representative charge transport layers are as following; HTL – poly(3,4-ethylenedioxythiophene) polystyrene sulfonate (PEDOT:PSS), MoO_3, Va_2O_5, etc. and ETL – ZnO, TiO_x, PDINO, etc.

1.1.4 Advantages and Applications of OSCs

Inorganic semiconductors (Si, GaAs, CIGS, etc.) based solar cells showed high PCE at least over 20%, and base material of most commercialized solar cells is Si. Although Si solar cells have many strengths such as high PCEs, high stability, cost effectiveness (due to abundant of Si), etc., there are critical disadvantages such as heavy weight, opaque properties (when it is installed on the ground, sun light cannot reach behind the solar panels), complex processing condition to fabricate devices, and so on. OSC is potential photovoltaic devices to overcome such disadvantages of Si solar cells.

Due to high absorption coefficient of organic semiconductors, thickness of active layer is around 100 nm which is enough to absorb incident sun light, while cell thickness of Si solar cells is typically around 100-500 μm. Therefore OSCs have lighter weight than Si solar cell obviously. Furthermore because of the thin active layer, OSCs have semi-transparent properties while Si solar cell is opaque. By appropriately designing organic semiconductors, absorption and bandgap properties can be easily tuned which means color of active layer is easily modulated. Hence aesthetically pleasing colored photovoltaic devices can be fabricated.

The active layer of OSCs is deposited by thermal evaporation or solution-processing. Deposition by thermal evaporation is normally using small molecules, and polymer-based active layer is deposited by solution-processing. In case of solution-processing methods, it has a powerful advantages that large-area devices can be fabricated via slot-die or roll-to-roll processing with flexible substrates. Since flexible substrates have light weight, the flexible OSCs have a great potential to portable electronic devices as shown in **Figure 1.6**.

Potential Applications of Organic Solar Cells

Colorful Semi-Transparent OSCs

Roll-to-Roll Processable

Flexible Application
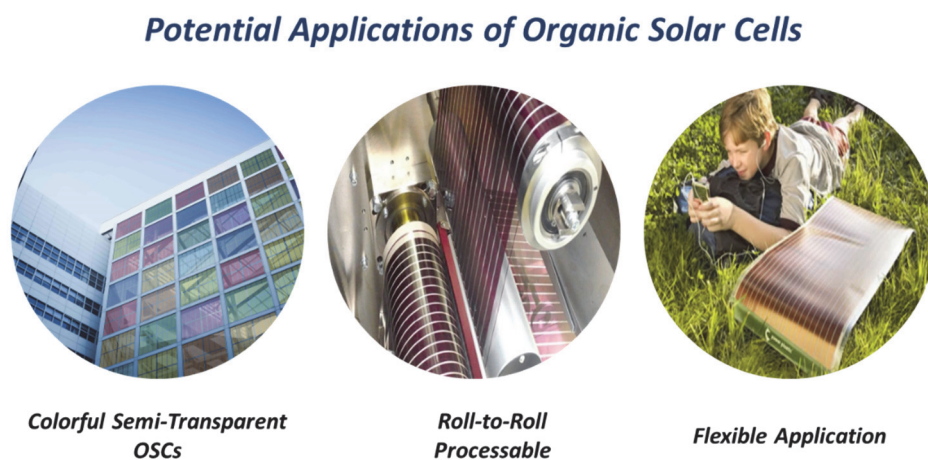
Figure. 1. 6. Potential applications of OSCs.

1.2 Charge Transport and Recombination of OSCs

1.2.1 Recombination Mechanisms

Charge recombination is generally divided into two type of recombination; radiative and non-radiative. Radiative recombination is also divided into two types; band-to-band radiative recombination and stimulated emission. The band-to-band recombination is occurred when electron excited to conduction band is came back to valence band with light emission. This effect is related to how light-emitting diodes can generate photons, and this recombination processes are usually occurred in direct bandgap materials. Stimulated emission is related to lasers. In OSCs, non-radiative recombination is general loss mechanisms of energy and extracted charge carriers. In this section, type of non-radiative recombination and their detailed properties are discussed.

When the light is absorbed to semiconductors, electron is excited to conduction band (or LUMO level in organic materials) and hole is generated in valence band (or HOMO level) at the same time. Excited electron and hole pairs (i.e., excitons) are bound by electrostatic Coulomb force, and the excitons can be easily recombined if there is insufficient energy for separation into free charge carriers. This is known as geminate (or monomolecular) recombination of excitons.

Excitons can be dissociated into weaker bound electron-hole pairs when appropriate combination of donor and acceptor materials are used with sufficient energy difference. These weaker bound state of electron-hole pairs are called as CT states. The CT states of electron-hole pairs are separated easily into free charge carriers by internal electric field in the devices or thermal energy.[23-24] It can be quenched with geminate recombination, but it is not a major loss mechanism in typical high-performance OSCs.

At early stage in OSCs, organic semiconductors have low carrier mobilities and disordered structures in thin film state. With the low mobilities, charge carriers move slowly within donor and acceptor phases which results to make many chances to recombine electrons and holes each other. This situation is well matched with Langevin theory that the important factor related to recombination is the rate of how often holes and electrons meet each other rather than time in which recombination even takes place. The Langevin recombination rate is expressed by equation (1-6);

$$R_L = k_L\left(np - n_i^2\right) = \frac{e}{\varepsilon_0 \varepsilon_r}(\mu_n + \mu_p)(np - n_i^2) \tag{1-6}$$

where k_L is the Langevin recombination prefactor, $\varepsilon_0\varepsilon_r$ is the dielectric permittivity of the active layer, μ_n is electrons mobility, μ_p is holes mobility, n is the electron concentration, p is the hole concentration and n_i is the intrinsic carrier concentration. In real experimental situation, non-geminate recombination

is often reduced, and the time dependent recombination is also observed compared to Langevin model which is only applied in low-mobility system.[25]

Trap-assisted (or Shockley-Read-Hall, SRH) recombination is occurred when the charge carriers are trapped in the state of deep level in the bandgap or trap sites of interfacial defects or impurities in materials. In addition, bimolecular recombination is also important loss mechanism in OSCs. Monomolecular and bimolecular recombination is the main loss mechanisms in OSCs, and the recombination have been investigated via various methods; transient photoconductivity, transient absorption spectroscopy, time-delayed dual pulse experiment, light intensity dependent measurements, etc. The light intensity dependent measurement is the simplest technique that can be conducted by just varying light intensity of incident light sources via neutral density filters, etc. It is obvious that charge transport and extraction properties are different by incident light intensities. If light intensity is lower than 1 sun intensity by an order of magnitude, generated photocurrents also reduced by an order of magnitude. In this low light intensity situation, photocurrents can be affected more by trap sites, diode currents (under dark) compared to intense light intensity (1 sun). From fitting J_{SC} vs. light intensity (I_{light}) and V_{OC} vs. I_{light} graphs, information of bimolecular and monomolecular recombination can be obtained, respectively. In general, J_{SC} is proportional to I_{light}^{s}. With a log-log scale plot of J_{SC} vs. I_{light} graphs, if the graphs showed nearly linear dependence (thus, $s \to 1$), bimolecular recombination is relatively weak in this system. (**Figure 1.7a**) On the contrary, if the s is lower and far from than 1, it indicates that carrier losses exist which originated from bimolecular recombination. Information of monomolecular (trap assisted or SRH) recombination can be obtained from V_{OC} vs. I_{light} graphs. V_{OC} is expressed by equation (1-7);

$$V_{OC} = \frac{E_{gap}}{q} - \frac{kT}{q} \ln \left[\frac{(1-P_D)\gamma N_C^2}{P_D G} \right] \tag{1-7}$$

where E_{gap} is the energy difference between the $HOMO_{donor}$ and $LUMO_{acceptor}$, q is the elementary charge, T is temperature in Kelvin, P_D is the dissociation probability of the electron (e)-hole (h) pairs, γ is the Langevin recombination constant, N_C is the effective density of states, and G is the generation rate of bound electron-hole pairs. If V_{OC} exhibited linear dependence on $\ln(I_{light})$ in semi log plots, only bimolecular recombination is loss mechanism in the given system. If slope of V_{OC} vs. $\ln(I_{light})$ graphs is higher than kT/q, it indicates that additional trap-assisted recombination is involved. (**Figure 1.7b**) Detailed experimental examples are shown from Chapter 2 to Chapter 5.
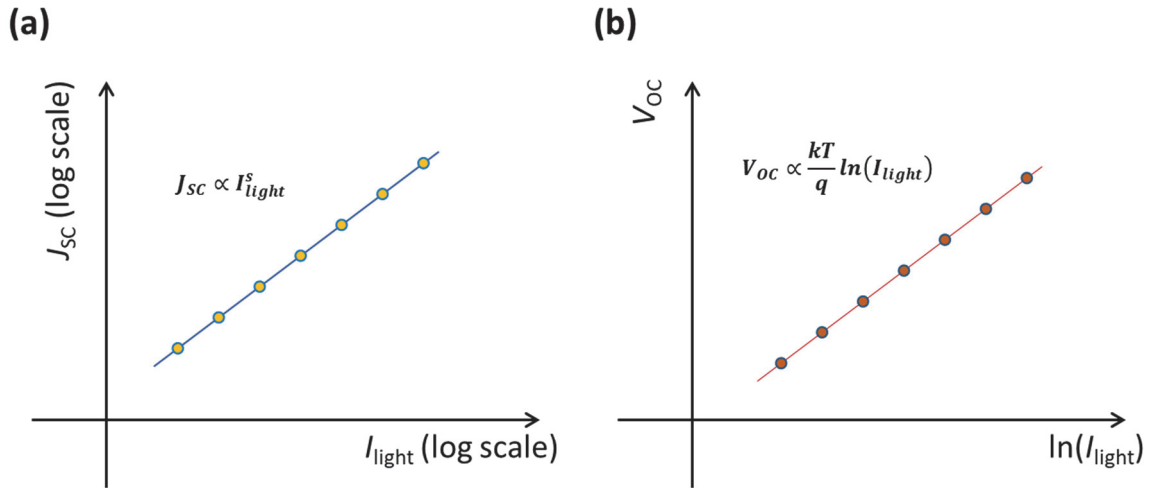
Figure. 1. 7. Schematic graphs of (a) J_{SC} vs. I_{light} and (b) V_{OC} vs. I_{light} characteristics for typical OSCs.

Charge recombination is also related to the energy loss in OSCs. Energy loss is determined by energy difference between optical bandgap (E_g) and eV_{OC}. Energy of CT states (E_{CT}) is determined by energy difference of quasi-Fermi level of HOMO and LUMO for donor and acceptor materials. Therefore $E_g - E_{CT}$ can be tuned by modifying and designing molecular structures of donor and acceptor. Energy loss originated by charge recombination is defined by difference between E_{CT} and eV_{OC}. $E_{CT} - eV_{OC}$ is typically attributed by both radiative and non-radiative recombination. In the Shockley-Queisser limit, maximum V_{OC} is achievable of $E_g - 0.3$ eV due to radiative recombination. Additional energy losses are occurred by non-radiative recombination, and this is expressed by equation (1-8);

$$\Delta V_{OC,NR} = -\frac{kT}{q} \ln (\phi) \tag{1-8}$$

where ϕ is the radiative efficiency of the system.[26] To achieve high photocurrent and open-circuit voltages, it is important to avoid recombination losses by using appropriate donor and acceptor combination, morphology control, appropriate charge transport layers, and so on.

1.2.2 Charge Transport Properties and Characterizations

In OSCs, photocurrent generation and extraction are greatly important to achieve high PCEs. Balance of hole and electron mobilities are highly important factors to affect charge transport and extraction in OSCs. Photocurrent density (J_{ph}) can be expressed by equation (1-9) which suggested and derived by Sokel and Hughes[27];

$$J_{ph} = qGL \left[\frac{\exp{(V_{eff}/V_t)}+1}{\exp{(V_{eff}/V_t)}-1} - 2\frac{V_t}{V} \right]$$
(1-9)

where L is thickness of active layer, V_{eff} is the effective voltage that determined by voltage drop across the active layer (V_0-V) and $V_t = kT/q$, and this equation considers both drift and diffusion of charge carriers and assume that recombination of charge carriers is negligible. According to the equation (1-9), J_{ph} vs. V_{eff} graphs show two regimes: a linear dependence of J_{ph} within small biases (regime 1) and J_{ph} saturation within high biases (regime 2). (**Figure 1.8a**)
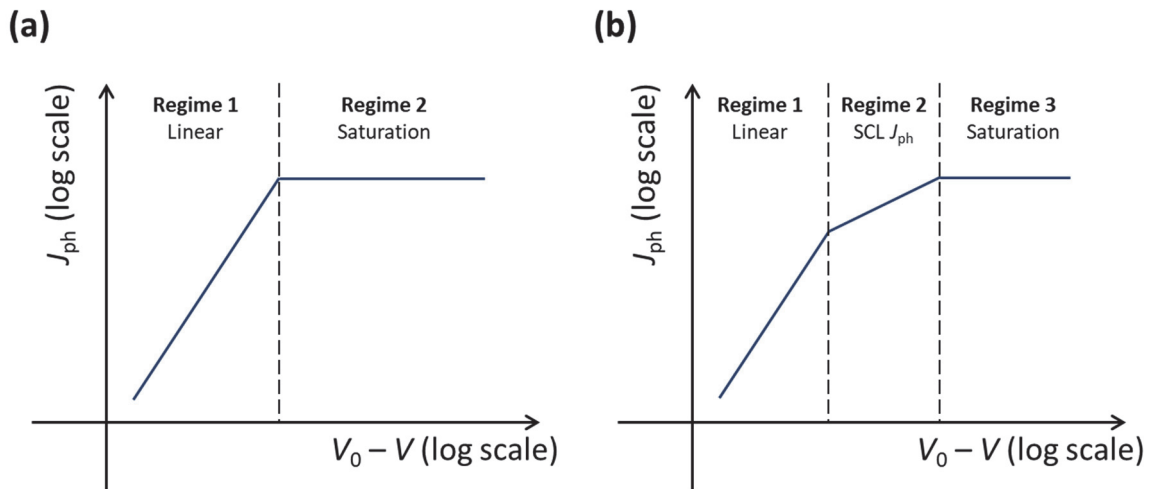
Figure. 1. 8. Schematic graphs of photocurrent density (J_{ph}) versus effective voltage (V_{eff}) characteristics for the devices with (a) balanced hole and electron densities and (b) imbalanced hole and electron densities.

Photocurrent extraction is influenced by mean carrier drift length w. The charge carriers are readily extracted out when the electron and hole drift lengths (w_n and w_p, respectively) are larger than L. However if w_n is greatly higher than w_p (thus, $w_n \gg w_p$) and w_p is smaller than L ($w_p < L$), a positive space charge is formed near the anode, resulting in three regimes for J_{ph} vs. V_{eff} graphs. (**Figure 1.8b**) The imbalanced electron and hole densities (or mobilities) provide space-charge-limited J_{ph} which follows equation (1-10);

$$J_{ph} \le (qG)^{0.75} \left(\frac{9}{8}\varepsilon_0\varepsilon_r\mu_h\right)^{0.25} \sqrt{V} \qquad (1\text{-}10)$$

where μ_h is hole mobility. The fill factor of OSCs is often limited by this space-charge-limited J_{ph}.

For single carrier devices with semiconductors, J-V curves exhibit 4 regions as shown in **Figure 1.9**. In region 1, current follows Ohm's law. Region 2 and region 4 shows trap-limited and trap-free space-charge-limited current (SCLC) behavior. Region 3 is trap-filled limit (TFL) region.

Electron and hole mobilities (μ_e and μ_h, respectively) can be measured by various techniques such as time-of-flight (TOF), field-effect transistor (FET), SCLC, charge extraction by linearly increasing voltage (CELIV), etc. Calculating the mobilities via SCLC is most common methods in OSC research field, since current flow direction is same with the photovoltaic devices. To observe SCLC regime, the devices should be fabricated with ohmic contact between semiconductor and electrodes to do not limit current injection by contact barrier, and space charge should be formed with appropriate charge transport layer and electrodes, thus, single-carrier devices. If the active layer does not have traps under high voltages, the current density follows by Mott-Gurney equation (1-11);

$$J = \frac{9}{8}\mu\varepsilon_0\varepsilon_r\frac{V^2}{L^3} \qquad (1\text{-}11)$$

By fitting this equation to the J-V curves of single-carrier devices, mobilities are calculated.

Furthermore, trap densities in a give system can be calculated by fitting onset voltage of TFL region (V_{TFL}) with equation (1-12);

$$V_{TFL} = \frac{eN_tL^2}{2\varepsilon_0\varepsilon_r} \qquad (1\text{-}12)$$

where N_t is trap density.
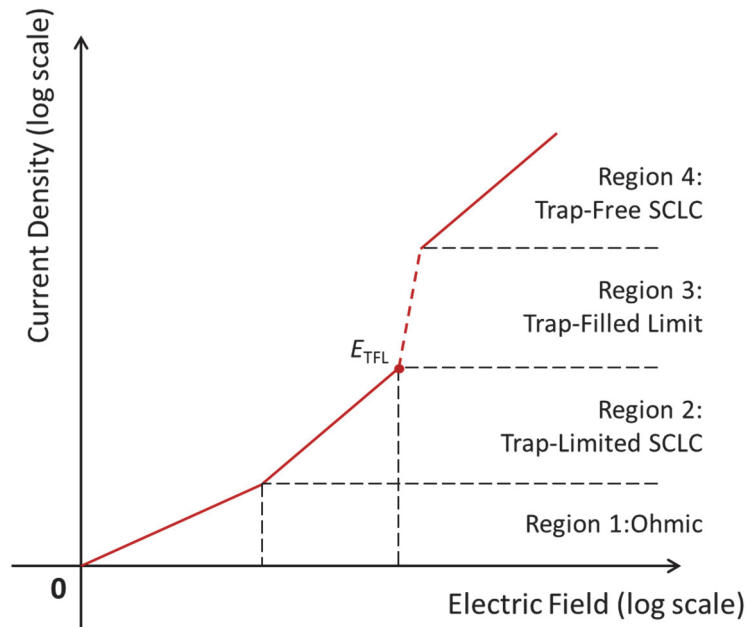
Figure. 1. 9. A Schematic relationship between current density and electric field of single-carrier devices. This graph follows space-charge-limited current (SCLC) theory.

Chapter 2. A Universal Processing Additive for High-Performance Polymer Solar Cells

This chapter is reproduced in part with permission of "RSC Adv., Vol. 7, Pages 7476-7482". Copyright 2017, The Royal Society of Chemistry.

2.1 Research Backgrounds

Polymer solar cells (PSCs) based on bulk-heterojunction (BHJ) which blends an electron-donor polymer and an electron-acceptor fullerene derivative have attracted much interest due to their many advantages including low-cost solution processability, light-weight, and mechanical flexibility for portable photovoltaic devices.[28-30] The power conversion efficiencies (PCEs) of PSCs have gradually improved up to 10% by intensive developments such as synthesizing efficient semiconducting polymers,[31] controlling the morphology of the active layer,[32-36] utilizing ternary blend system,[35, 37-39] introducing additional interfacial layer,[40-42] and designing device architectures.[43-44]

The morphology optimization of the active layer is one of the effective strategies to produce high-efficiency PSCs with given materials. Several methods have been introduced to control the morphology of the active layer such as thermal annealing, solvent-vapor annealing, and introduction of processing additive. Thermal annealing process has benefits to crystallization and nanoscale phase separation of photoactive components, which enlarge interfacial area and enhance charge-carrier mobility.[45-46] Solvent-vapor annealing results in short π-π stacking distance by increasing the degree of crystallinity within the active layer.[47-48]

Compared to other methods, processing additive is the simplest and fastest way for morphology optimization of the active layer. This method only needs introduction of small amount of processing additives into the BHJ solution without any post treatments. Representative processing additives are 1,8-octanedithiol (ODT),[30, 49-51] 1-chloronaphthalene (CN),[52-55] 1,8-diiodooctane (DIO),[56-59] and diphenyl ether (DPE).[16, 32, 60] These additives dramatically enhanced the device performance by improving exciton dissociation and charge transport induced by formation of donor-acceptor (D-A) bicontinuous interpenetrating network. K. H. Park *et al.* demonstrated the ODT helps polymer orientation, leading to closer packing of polymer chains and increased charge-carrier mobility.[51] Y. Kim *et al.* reported great enhancement of PCE from 3.61% to 7.08% for quinoxaline polymer based solar cells by using CN additive. They found that the CN promotes nanoscale phase separation via improved miscibility of the polymer and [6,6]-phenyl-C_{71}-butyric acid methyl ester (PC$_{71}$BM). This gave rise to

balanced hole and electron mobility and dramatic enhancements in J_{SC} and FF.[53] In addition, the device processed with DIO exhibited high device efficiency of 10% for poly[[4,8-bis[(2-ethylhexyl)oxy]benzo[1,2-b:4,5-b']dithiophene-2,6-diyl][3-fluoro-2-[(2-ethylhexyl)-carbonyl]thieno-[3,4-b]thiophenediyl]] (PTB7):PC$_{71}$BM-based PSCs. It is well known that DIO selectively dissolves PCBM aggregates in the BHJ film, allowing PCBM molecules to be intercalated into polymer domains.[58] C. H. Y. Ho *et al.* recently investigated an influence of DIO concentration on morphology and charge-carrier mobility within the active layer in PTB7:PC$_{71}$BM PSCs. They found that the amount of DIO in mother solvent affects an electron mobility, but not hole mobility. Optimized DIO concentration led to PCE enhancement from 4.2% to 7.0% by balanced hole and electron mobility.[57]

Introduction of DPE into BHJ film resulted in high PCE of 8.64% by balanced hole and electron mobility and nano-fibrillar morphologies of the active layer in poly[[(2,5-bis(2-hexyldecyloxy)phenylene)-*alt*-(5,6-difluoro-4,7-di(thiophen-2-yl)benzo[c][1,2,5]-thiadiazole)] (PPDT2FBT):PC$_{71}$BM PSCs.[32] H. Choi *et al.* also utilized mixed solvent of chlorobenzene (CB) and DPE in small bandgap PSCs. The addition of DPE into CB led to remarkable PCE enhancement from 3.24% to 9.40% This improvement was attributed to continuous and well-distributed polymer networks in both lateral and vertical directions of the active layer.[16]

In this work, we demonstrate the effects of various processing additives on device performance as a function of polymer crystallinity. Four processing additives - DPE, DIO, CN, and ODT were used to compare photovoltaic characteristics, morphologies, and charge carrier recombination rates. Especially, PSCs with DPE were exhibited high-performance regardless of polymer crystallinity. The results indicate that DPE has universal benefits to photovoltaic performances as the processing additive in all kinds of polymers.

2.2 Experimental Details

General: The AFM height and phase images were obtained by using a Veeco AFM microscope in a tapping mode. Light intensity dependence of J_{SC} was measured with neutral density filters. GIWAXS measurements were carried out at the PLS-II 9A U-SAXS beam line of Pohang Accelerator Laboratory.

Fabrication and characterization of PSCs: The device configuration of PSCs was conventional structure of Glass/ITO/PEDOT:PSS/Active Layer/Al. Firstly, patterned ITO coated glass substrates were cleaned in an ultra-sonicator in order of deionized water, acetone, and isopropyl alcohol, and then the substrates were dried in an oven at 100 °C overnight. The PEDOT:PSS (Baytron AI 4083) layer was spin coated on the substrate at 4000 rpm for 40 s, then baked on a hot plate at 140 °C for 10 minutes in the air. After baking, the substrates were moved into a glove box filled with nitrogen. P3HT (number-average molecular weight (M_n) = 60 kDa, polydispersity index (PDI) = 1.4) was purchased from Organic Semiconductor Materials (OSM, Republic of Korea). PBDTTPD (weight-average molecular weight (M_w) = 39.5 kDa, PDI = 2.2), PTB7 (M_w = 10.8 kDa, PDI = 2.4), PCDTBT (M_w = 33 kDa, PDI = 2.3) were purchased from 1-Material. PPDT2FBT (M_n = 42.6 kDa, PDI = 2.8) was synthesized by ourselves.[5] The PSCs based on five donor polymers were fabricated using different experimental conditions including solution concentration, D:A ratio and amount of processing additives (DPE, DIO, CN and ODT). Solutions for P3HT:$PC_{61}BM$ (1:0.8, w/w), PPDT2FBT:$PC_{71}BM$ (1:1.5, w/w), PBDTTPD:$PC_{71}BM$ (1:1.5, w/w), PTB7:$PC_{71}BM$ (1:1.25, w/w), and PCDTBT:$PC_{71}BM$ (1:4, w/w) were dissolved in chlorobenzene (CB) with polymer concentration of 13, 14, 8, 12, and 7 mg/ml with 2, 3, 5, 3, and 3vol% of additives, respectively. Except PBDTTPD (110 °C), the other solutions were stirred at 60 °C overnight. After coating active layer, the substrates were brought into a high vacuum chamber (~10^{-6} Torr), and Al (100 nm) was deposited by thermal evaporation process. In case of P3HT PSCs, after deposition of the Al layer, the devices were thermally annealed at 150 °C for 10 minutes to obtain optimum device performance. The device area was 13 mm^2. Measurements were conducted in the glove box using a high quality optical fiber to lead the light from a Xenon arc lamp solar simulator. *J-V* characteristics were measured under AM 1.5G illumination (100 mW/cm^2) with a Keithley 2635A source measurement unit, and EQE was measured in the air using an EQE system (Model QEX7) by PV measurements Inc. (Boulder, Colorado).

2.3 Results and Discussion
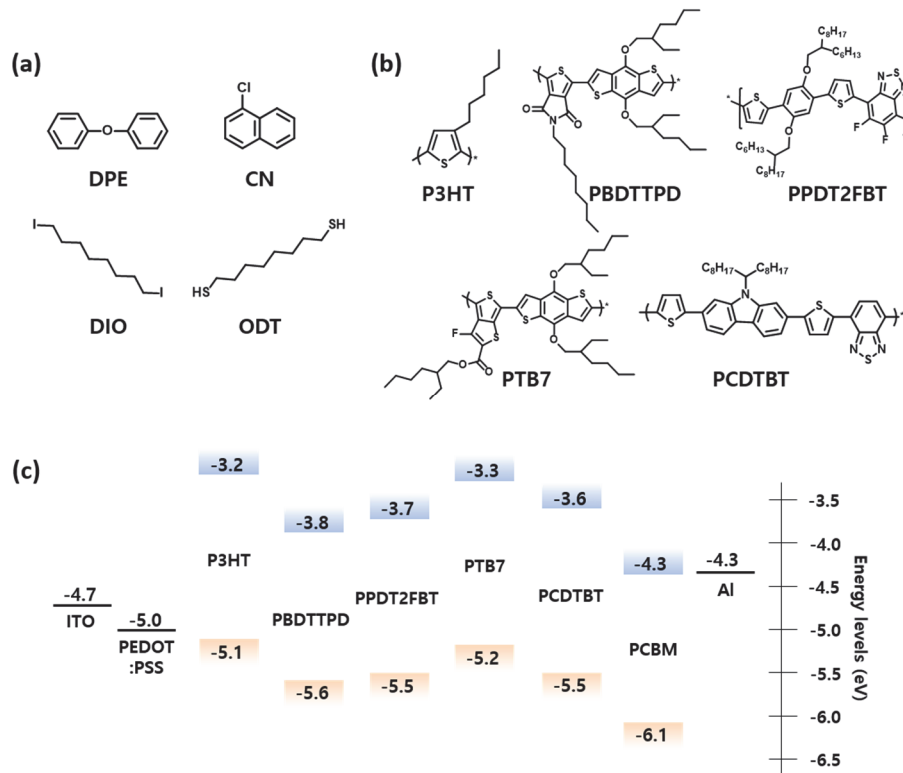
Figure 2. 1. Molecular structure of (a) processing additives and (b) donor polymers. (c) Energy band diagram of components of PSCs.

Molecular structure of processing additives (DPE, DIO, CN, and ODT) are prepared in **Figure 2.1a**. As the non-halogenate and non-thiol solvent, DPE has a strength in terms of the environmental-friendly solvent to use in PSCs.[61] Five photovoltaic polymers with different crystallinity are chosen as donor polymers for the photoactive layer in PSCs (**Figure 2.1b**). We classify those polymers according to the degree of crystallinity, where poly(3-hexylthiophene) (P3HT) is a highly crystalline polymer; poly(di(2-ethylhexyloxy)benzo[1,2-*b*:4,5-*b′*]dithiophene-*co*-octylthieno[3,4-*c*]pyrrole-4,6-dione) (PBDTTPD), PPDT2FBT, and PTB7 are semi-crystalline polymers; and poly[N-9'-heptadecanyl-2,7-carbazole-alt-5,5-(4,7-di-2-thienyl-2',1',3'-benzothiadiazole]) (PCDTBT) is an amorphous polymer.

We fabricated PSCs using simple and conventional structure of ITO/PEDOT:PSS/polymer:PCBM/Al. **Figure 2.1c** presents energy band diagrams of the components of the PSCs. We only focused on the effect of processing additives on device performance in the PSCs based on different donor polymers without any interlayers. The CB was used as the main solvent for depositing the active layer via spin-coating method. The detailed methods for device fabrication are

described in Experimental section. **Figure 2.2a-e** exhibit current density versus voltage (*J-V*) characteristics of the PSCs with different donor polymers and processing additives. External quantum efficiency (EQE) curves of corresponding PSCs are shown **in Figure 2.2f** and **Figure 2.3**. Furthermore, the detailed photovoltaic parameters for all PSCs are summarized in **Table 2.1**.

There is no significant effect of processing additives on the performance of P3HT:PCBM PSCs. The control device without additive already showed high PCE of 3.29% compared to those of the devices with additives. However, introduction of all processing additives led to slight increase in fill factor (*FF*). Among various processing additives, the device with DPE showed the highest *FF* of 0.70 and PCE of 3.77%. The devices with DIO and CN also achieved high device efficiencies of 3.68% and 3.73%, respectively. In contrast, the device with ODT showed lower open-circuit voltage (V_{OC}) of 0.55 V compared to other devices (0.61-0.62 V).
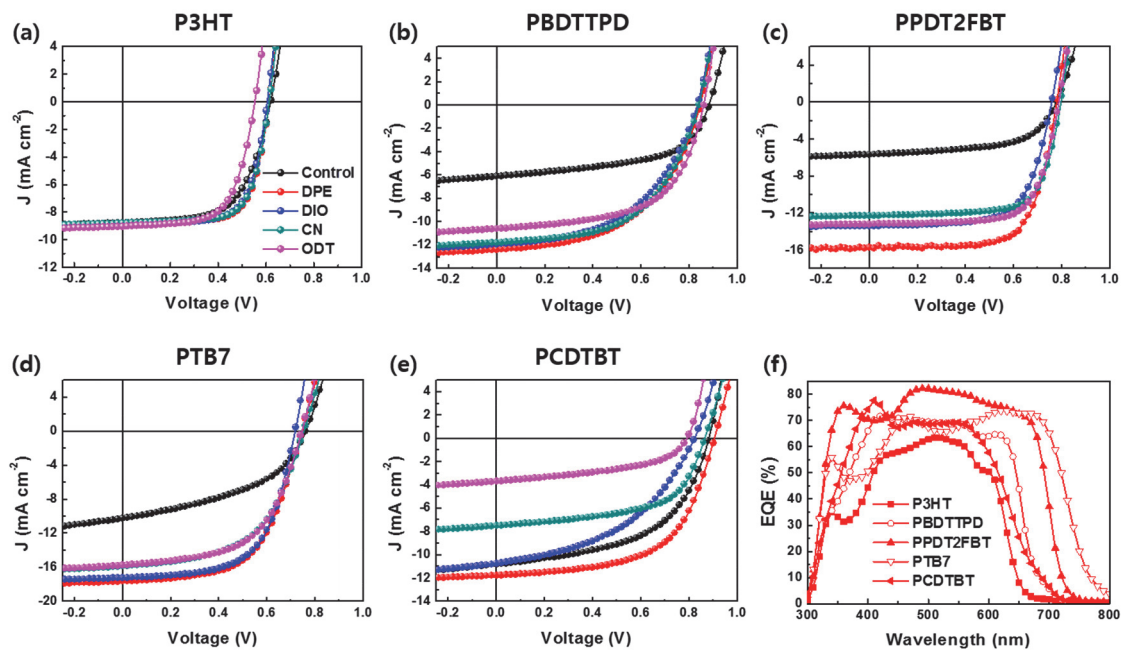
Figure 2. 2. *J-V* characteristics of BHJ PSCs based on (a) P3HT, (b) PBDTTPD, (c) PPDT2FBT, (d) PTB7, and (e) PCDTBT with different processing additives. (f) EQE spectra of all PSCs with DPE.
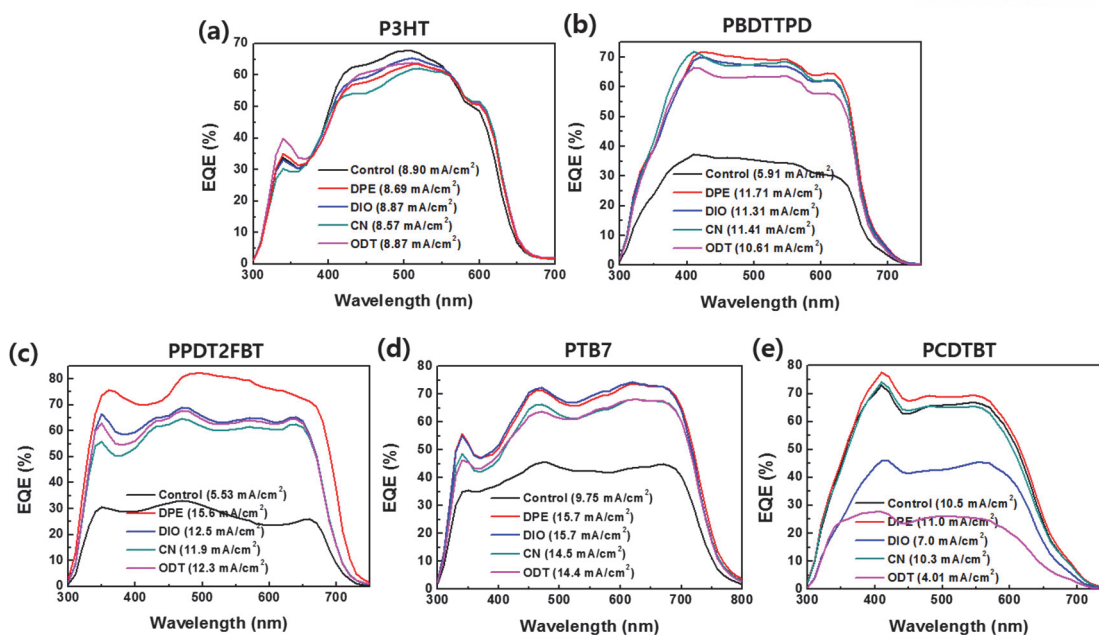
Figure 2. 3. EQE spectra of PSCs based on (a) P3HT, (b) PBDTTPD, (c) PPDT2FBT, (d) PTB7 and (e) PCDTBT. Note that calculated J_{SC} is indicated in parentheses.

There are huge differences in the device performances between the PBDTTPD-based devices with and without processing additives. The device without additive exhibited PCE of 2.98% with short-circuit current density (J_{SC}) of 6.10 mA cm^{-2}, V_{OC} of 0.88 V, and FF of 0.55. It is noticeable that all devices with additive showed high PCE over 5% that are mostly attributed to remarkable increase in J_{SC} (up to 12.41 mA cm^{-2}). Same tendencies were observed in PPDT2FBT and PTB7-based devices. Introduction of additive has great effect on the performance of the devices based on semi-crystalline polymer (PPDT2FBT: 3.23% → 8.64% and PTB7: 3.48 → 7.70%). In particular, both PPDT2FBT and PTB7 devices with DPE exhibited the highest J_{SC} and PCE among the devices with various processing additives. Compared to other donor polymers, different tendency was observed in the device based on PCDTBT which is known as one of the amorphous polymers in the PSCs. Control device without additive showed PCE of 5.07%. Apart from the device with DPE, other processing additives resulted in significant decrease in FF or J_{SC}. In contrast, DPE improved the device efficiency up to 6.27% due to simultaneous increases in all photovoltaic parameters.

Table 2. 1. Detailed photovoltaic parameters of the devices with different donor polymers and processing additives

Polymer	Additives	J_{SC} [mA cm^{-2}]	V_{OC} [V]	FF	PCE [%]
P3HT	Control	8.76	0.62	0.61	3.29
	DPE	8.85	0.61	0.70	3.77
	DIO	8.91	0.61	0.68	3.68
	CN	8.79	0.61	0.69	3.73
	ODT	9.02	0.55	0.64	3.18
PBDTTPD	Control	6.10	0.88	0.55	2.98
	DPE	12.4	0.85	0.52	5.40
	DIO	11.9	0.83	0.51	5.03
	CN	11.8	0.84	0.54	5.37
	ODT	10.6	0.86	0.58	5.32
PPDT2FBT	Control	6.16	0.84	0.63	3.23
	DPE	15.7	0.78	0.71	8.64
	DIO	13.4	0.76	0.68	6.84
	CN	12.3	0.80	0.71	6.97
	ODT	13.2	0.79	0.71	7.32
PTB7	Control	10.2	0.76	0.45	3.48
	DPE	17.6	0.75	0.59	7.70
	DIO	17.2	0.72	0.61	7.55
	CN	15.9	0.75	0.55	6.57
	ODT	15.7	0.74	0.57	6.65
PCDTBT	Control	10.8	0.88	0.53	5.07
	DPE	11.7	0.91	0.59	6.27
	DIO	10.7	0.82	0.45	3.97
	CN	7.49	0.87	0.58	3.78
	ODT	3.68	0.79	0.48	1.38
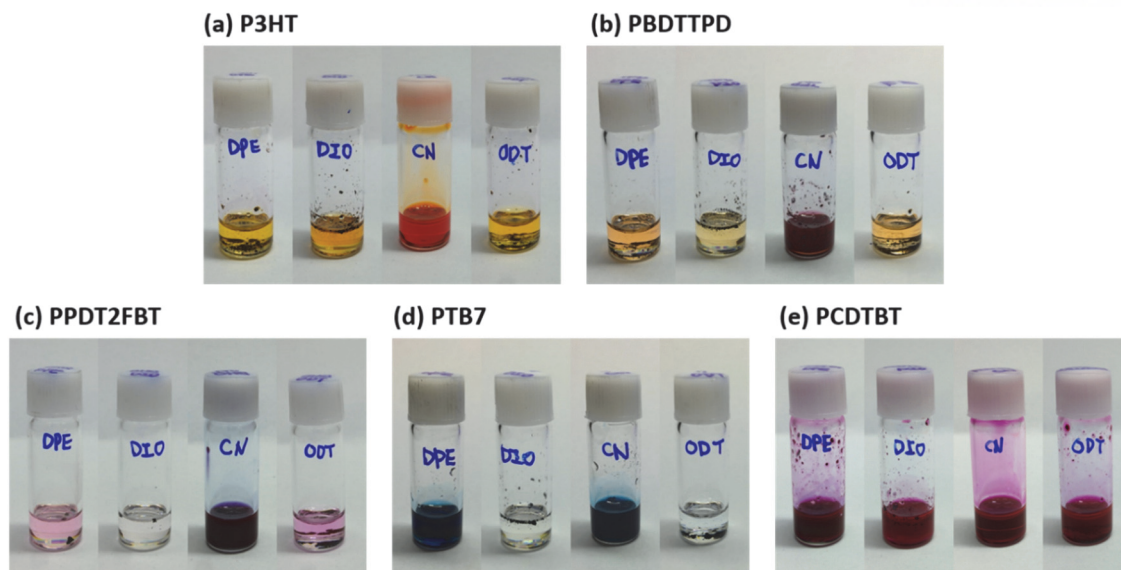
Figure 2. 4. Solubility test for five donor polymers in different processing additives (concentration: 2.5 mg/ml).

To understand the reason why DPE gives rise to the highest PCE among various processing additives, we checked solubility of five donor polymers in each processing additive. As shown in **Figure 2.4**, it is easily noticed that CN is a good solvent for all polymers, while other additives seem to act as the poor solvent. Interestingly, the colors of polymer solutions dissolved in DPE were deeper than those of the solutions dissolved in DIO and ODT. These imply that DPE satisfies the theta condition at 60 °C which solutions are stirred overnight to fabricate active layers of PSCs, indicating DPE can play a role as theta solvent for all polymers among poor solvents.[62] In theta solvent, polymer coils act like ideal chains because the interaction between a theta solvent and a polymer is balanced at theta point (The enthalpy of mixing is zero).[63] Therefore, DPE can be widely used as the beneficial processing additive for BHJ PSCs regardless of polymer crystallinity.

The morphologies of BHJ films with different processing additives were investigated by atomic force microscopy (AFM). Those AFM topography images are shown in **Figure 2.5**. The BHJ film based on P3HT without additive had uniform surface with low root-mean-square (RMS) roughness of 1.12 nm (**Figure 2.5a**). The PCBM cannot aggregate freely in intense interaction between crystalline polymer chains, so it is hard to phase separation during solvent evaporation.[64] After introducing processing additives, small or large islands were observed which may be attributed to separation and growth of PCBM molecules. Among BHJ films with additives, the film with DPE exhibited the lowest RMS roughness of 4.89 nm (DIO: 6.74 nm, CN: 5.54 nm, and ODT: 7.53 nm).
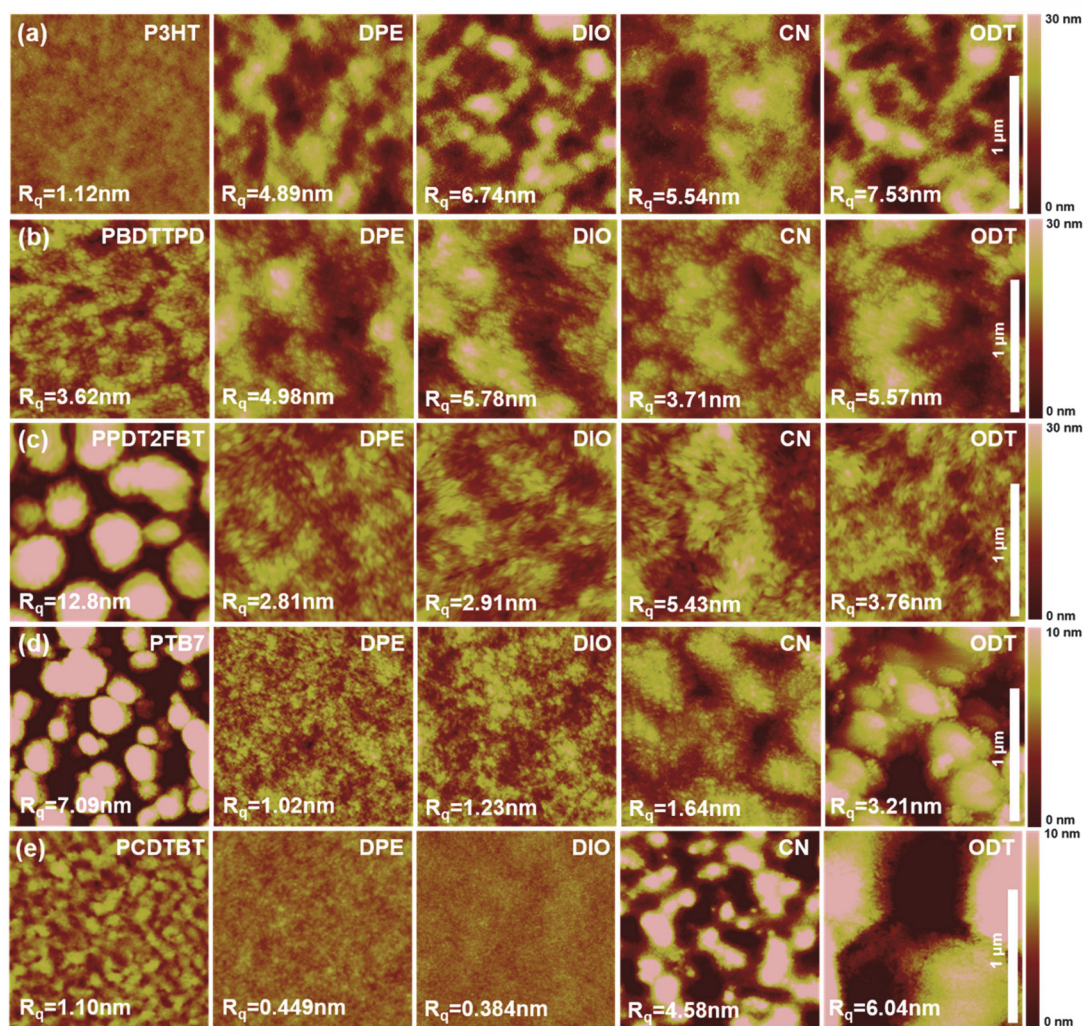
Figure 2. 5. AFM topographical images of (a) P3HT, (b) PBDTTPD, (c) PPDT2FBT, (d) PTB7, and (e) PCDTBT BHJ films without processing additives (1st column), and with DPE (2nd column), DIO (3rd column), CN (4th column), and ODT (5th column) deposited on ITO/PEDOT:PSS substrates. Root mean square values of roughness for each films are given at the left-bottom corner of each image.

Similar to P3HT, introduction of processing additive increased surface roughness of BHJ films based on PBDTTPD (**Figure 2.5b**). Unlike P3HT system, these rough surface morphologies remarkably enhanced the performance of PBDTTPD:$PC_{71}BM$ devices. The film with CN had lower roughness of 3.71 nm compared to films with other additives (DPE: 4.98 nm, DIO: 5.78 nm, and ODT: 5.57 nm). However, all devices exhibited similar PCEs regardless of kinds of additive. We found that there is no correlation between surface roughness and device performance.

The morphologies of BHJ film based on PPDT2FBT can be significantly modulated by processing additives (**Figure 2.5c**). The film without additive showed uneven surface with large domains (few hundreds of nanometers in diameter).[32] This morphology led to poor device performance. In contrast,

introduction of processing additives induced uniform and smooth surface morphology. Among additives, smoothest surface roughness and nanofibrillar structure by DPE resulted in the highest device efficiency.

The morphologies of BHJ films based on PTB7 were analogous to PPDT2FBT system (**Figure 2.5d**). Processing additives led to uniform film with smooth surface roughness. However, films with CN and ODT exhibited larger agglomerations compared to those with DPE and DIO. This difference gave rise to distinction of J_{SC}. Specifically, more even and smoother surface by DPE and DIO resulted in higher PCEs.

The PCDTBT:PC$_{71}$BM BHJ films with DPE and DIO exhibited smooth surface roughness compared to films with CN and ODT (without additive: 1.10 nm, DPE: 0.449 nm, DIO: 0.384 nm, CN: 4.58 nm, ODT: 6.04 nm) **(Figure 2.5e)**. The J_{SC} difference of the device based on PCDTBT can be attributed to morphological changes by different additives.

According to AFM results of various BHJ films, although smooth and uniform surface induced by introduction of additive has a tendency to give rise to higher device performance, those morphologies do not guarantee the highest PCEs at all times.

To investigate the change of molecular ordering and orientation in BHJ films as a function of processing additives we measured grazing incidence wide angle X-ray scattering (GIWAXS). However, there were no significant changes of polymer chain packing and intermolecular ordering by different processing additives (**Figure 2.6**). These indicate that processing additives play a role in changing phase separation of polymer and PCBM domain, but not the strength of intermolecular ordering or the direction of polymer chain packing. The line-cuts of GIWAXS patterns and detailed crystallographic parameters were shown in **Figure 2.7** and **Table 2.2**. The GIWAXS results do not support the effect of different additives on device performance.
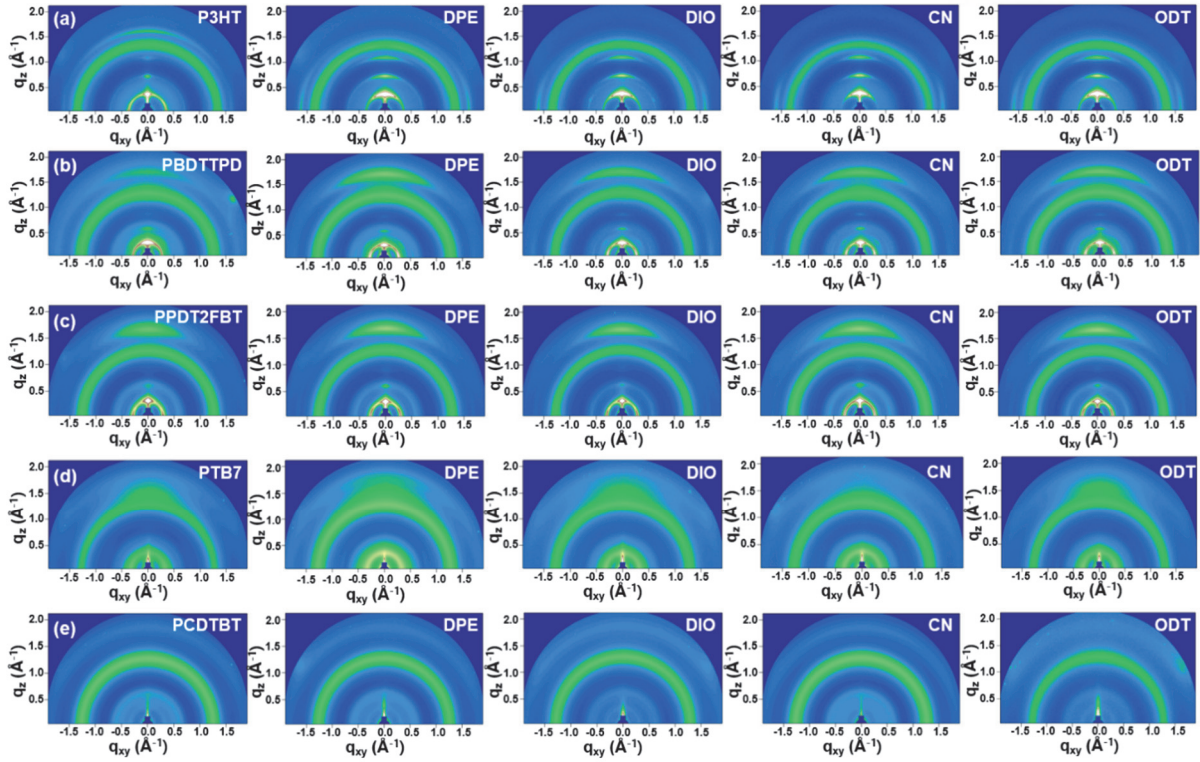
Figure 2. 6. GIWAXS patterns of (a) P3HT, (b) PBDTTPD, (c) PPDT2FBT, (d) PTB7, and (e) PCDTBT BHJ films without processing additives (1st column), and with DPE (2nd column), DIO (3rd column), CN (4th column), and ODT (5th column) on Si substrates.
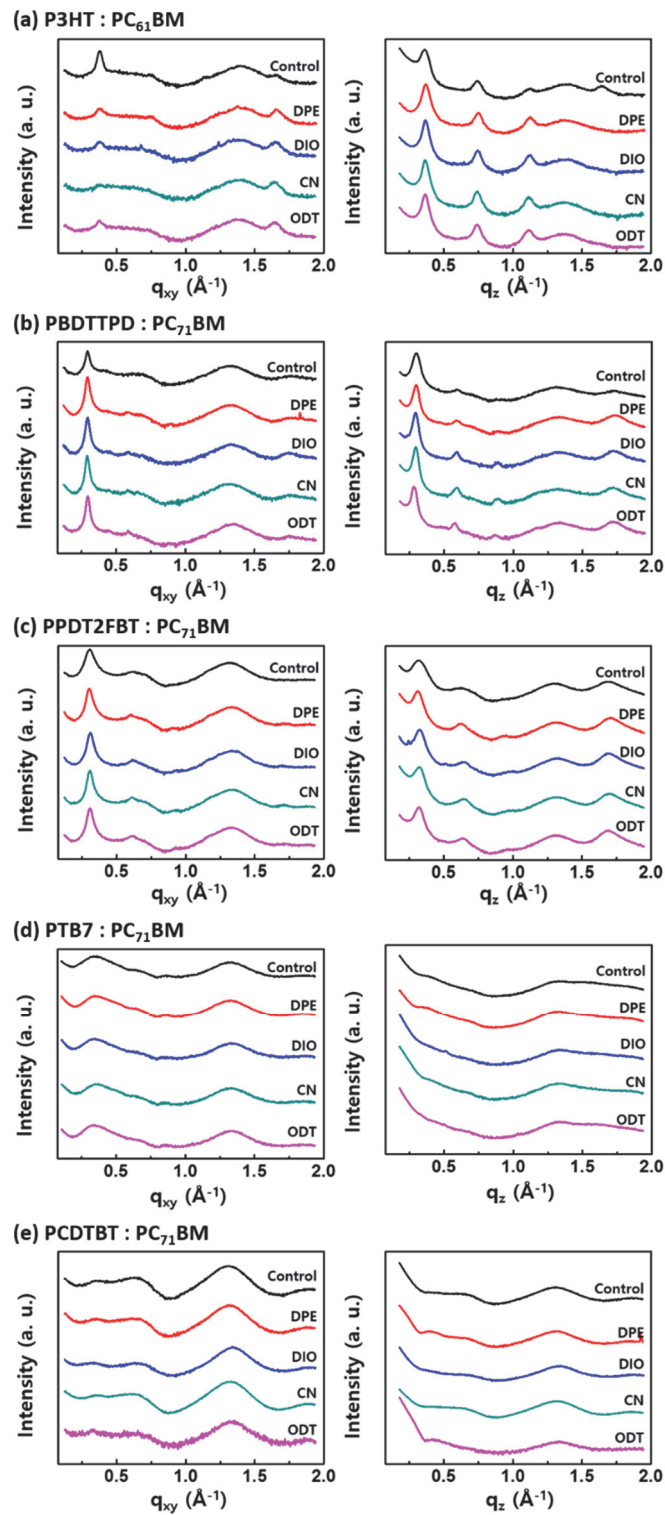
Figure 2. 7. GIWAXS linecut profiles of (a) P3HT, (b) PBDTTPD, (c) PPDT2FBT, (d) PTB7 and (e) PCDTBT BHJ films.

Table 2.2. Crystallographic parameters of polymer:PCBM BHJ films.

Polymer	Additive	GIWAXS parameters							
		Lamella spacing (q_{xy})		π-π stacking (q_{xy})		Lamella spacing (q_z)		π-π stacking (q_z)	
		q [Å^{-1}]	d [Å]	q [Å^{-1}]	d [Å]	q [Å^{-1}]	d [Å]	q [Å^{-1}]	d [Å]
P3HT	Control	0.3786	16.5958	1.6565	3.7930	0.3625	17.3329	1.6465	3.8161
	DPE	0.3768	16.6751	1.6568	3.7924	0.3703	16.9678	-	-
	DIO	0.3750	16.7552	1.6489	3.8105	0.3672	17.1111	-	-
	CN	0.3637	17.2757	1.6424	3.8256	0.3647	17.2284	-	-
	ODT	0.3745	16.7775	1.6426	3.8251	0.3656	17.1859	-	-
PBDTTPD	Control	0.2943	21.3496	1.7662	3.5575	0.3004	20.9161	1.7355	3.6204
	DPE	0.2932	21.4297	1.7592	3.5716	0.2982	21.0704	1.7357	3.6200
	DIO	0.2942	21.3569	1.7472	3.5961	0.2941	21.3641	1.7251	3.6422
	CN	0.2921	21.5104	1.7647	3.5605	0.2962	21.2126	1.7221	3.6486
	ODT	0.2947	21.3206	1.7431	3.6046	0.2812	22.3442	1.7207	3.6515
PPDT2FBT	Control	0.3049	20.6074	-	-	0.3193	19.6780	1.6888	3.7205
	DPE	0.3015	20.8397	1.7168	3.6598	0.3123	20.1191	1.7047	3.6858
	DIO	0.3102	20.2553	-	-	0.3250	19.3329	1.6903	3.7172
	CN	0.3068	20.4797	1.7128	3.6684	0.3241	19.3866	1.6965	3.7036
	ODT	0.3083	20.3801	-	-	0.3198	19.6472	1.6918	3.7139
PTB7	Control	0.3480	18.0551	-	-	-	-	-	-
	DPE	0.3478	18.0665	-	-	0.3638	17.2710	-	-
	DIO	0.3450	18.2121	-	-	-	-	-	-
	CN	0.3573	17.5852	-	-	-	-	-	-
	ODT	0.3455	18.1858	-	-	-	-	-	-
PCDTBT	Control	0.3517	17.8652	-	-	-	-	1.8735	3.3537
	DPE	0.3451	18.2069	-	-	0.3948	15.9149	1.8768	3.3478
	DIO	0.3327	18.8854	-	-	-	-	1.8867	3.3303
	CN	0.3587	17.5165	-	-	-	-	1.8701	3.3598
	ODT	0.3297	19.0573	-	-	0.4182	15.0244	-	-
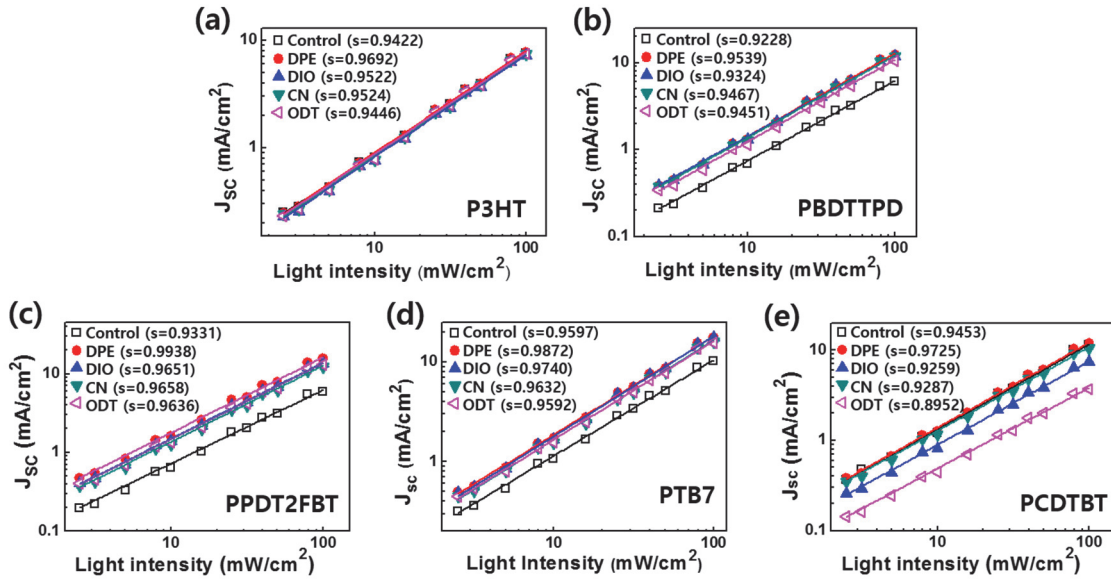
Figure 2. 8. The J_{SC} dependence on light intensity for PSCs based on P3HT, PBDTTPD, PPDT2FBT, PTB7, and PCDTBT without processing additives (control), and with DPE, DIO, CN, and ODT.

Morphological changes of BHJ films by different additives are deeply related to the degree of bimolecular recombination. The J_{SC} dependence on light intensity can provide the information about bimolecular recombination in the active layer.[60, 65] Therefore, we compared the J_{SC} dependence on light intensity (J_{SC} vs light intensity) of the devices as a function of processing additives. The logarithmic plots of J_{SC} vs light intensity for each PSC with are shown in **Figure 2.8**. According to the power-law J_{SC} dependence on the light intensity, the linear curves were fitted using Equation (2-1).

$$J_{SC} \propto I^s \tag{2-1}$$

where I is the intensity of incident light and s is an exponent constant for PSCs. As s is closer to unity, bimolecular recombination is more suppressed.[65] We calculate standard deviations of slopes differed by processing additives for each PSC. The device based on P3HT showed the lowest standard deviation of 0.009, indicating that processing additives have a little effect on bimolecular recombination of crystalline polymer. In contrast, the highest standard deviation of 0.0253 was observed for the devices based on PCDTBT. Morphology of amorphous polymers could be highly influenced by processing additives. Other semi-crystalline polymers (PBDTTPD, PPDT2FBT, and PTB7) have moderate standard deviation of 0.01 ~ 0.02. The J_{SC} vs light intensity results are consistent with J-V characteristics and AFM images. All PSCs with DPE exhibited the highest s values. These results obviously support

the improvements in J_{SC} and FF by reduced bimolecular recombination. Furthermore, DPE, which is universal additive and theta solvent, minimizes bimolecular recombination by optimizing the morphology of BHJ film, thereby leading to best device performance.

2.4 Conclusion

In conclusion, we successfully investigate the influence of various processing additives on the performance of the devices based on five donor polymers with different crystallinity. Morphologies of BHJ films based on donor polymers with crystallinity are easily influenced by processing additives. Although morphological changes are not consistent with device performance, all PSCs with DPE achieve the highest device efficiency regardless of polymer crystallinity. These high PCEs are obviously attributed to minimized bimolecular recombination within the active layer by introduction of DPE. In other words, DPE results in ideal morphology in BHJ system by acting as theta solvent. This work can offer an effective way to control the morphology of BHJ film and optimize the device performance by using universal processing additive in the BHJ PSCs.

Chapter 3. Non-Halogenated Diphenyl-Chalcogenide Solvent Processing Additives for High-Performance Polymer Bulk-Heterojunction Solar Cells

3.1 Research Backgrounds

Polymer:fullerene bulk-heterojunction solar cells (PSCs) have attracted great attention over the past two decades due to their many unique advantages such as their compatibility with simple and low-cost fabrication processes; large-area process-ability using scalable solution-based printing techniques; light-weight and mechanical flexibility[66-67]. Recently, high power conversion efficiencies (PCEs) over 11%, which are comparable with amorphous silicon solar cells, have been reported using newly designed conjugated polymers and non-fullerene acceptors.[68-69] High-performance PSCs can be achieved using several device fabrication strategies; using appropriate electron or hole transport layers[70-71], morphology control of bulk-heterojunction (BHJ) active layers[72-73], tandem structured devices[10, 20], photocurrent enhancement with surface plasmon resonance effects, and so on.[17, 74-75] Among these strategies, morphology control of active layer is the most fundamentally important factor to influence device performance. It has been demonstrated that film morphology can be easily adjusted by using solvent processing additives such as 1,8-diiodoocatne (DIO), 1,8-octanedithiol (ODT), 1-chloronaphthalene (CN), 1,2,4-trichlorobenzene (TCB), diphenyl ether (DPE) etc., and these solvent additives help to enhance device performance.[32, 41, 73, 76-82]

So far, reports of high-performance PSCs have almost always involved optimization with halogenated solvents such as chlorobenzene (CB) and 1,2-dichlorobenzene, due to their excellent solvation of conjugated polymers. In addition, the most commonly reported solvent additives such as DIO, TCB and CN also include halogen atoms. However, halogenated solvents are hazardous to the natural environment and human health through either vapor or dermal exposure. Therefore, it would be highly desirable to use non-halogenated solvents to process PSCs, if possible.

Recently, environmental-friendly processed PSCs have been reported using anisole, 1,2,4-trimethylbenzene (TMB), 2-methylanisole, *o*-xylene and toluene as host solvent, and 1,2-dimethyl-naphthalene and 1-phenylnaphthalene as solvent additives.[83-87] With these non-halogenated solvent systems, the high PCE was achieved over 11% suggesting great potential of non-halogenated solvents.[83] As non-halogenated solvent processed PSCs have attracted considerable attention recently, non-

halogenated solvent processing additives merit further investigation for the continued development of environmentally friendly PSCs.

DPE is an excellent example of an effective non-halogenated solvent additive which promotes the formation of effective film morphologies and enhanced PCE values in a wide range of conjugated polymers. In particular, it is one of the most effective additives for use with semi-crystalline polymer based BHJs. For instance, poly[(2,5-bis-(2-hexyldecyloxy)phenylene)-alt-(5,6-difluoro-4,7-di(thiophene-2-yl)benzo[c][1,2,5]-thiadiazole)] (PPDT2FBT):[6:6]-phenyl-C_{71}-butyric acid methyl ether ($PC_{71}BM$) PSCs showed great PCE enhancement from 3.23% to 8.64% upon introduction of DPE.[20] Furthermore, DPE is especially effective in thick active-layer PSCs, which produce larger short-circuit current densities (J_{SC}) through complete absorption of incident light, since it produces desirable morphologies throughout the whole film.[88-89] Y. Li *et al.* reported 8% of PCE (with high $J_{SC} = 17.19$ mA cm^{-2}) in 270 nm thick of poly(2,2′:5′,2″-terthiophene-*alt*-2,3-bis(3,4-bis(octyloxy)phenyl)-6,7-difluroquinoxaline) (PDFQx-3T):$PC_{71}BM$ PSCs which showed well phase-separated film morphologies with low RMS roughness of 1.6 nm and low bimolecular recombination.[90]

Although DPE has been demonstrated as one of the most effective solvent additives discovered to date, a detailed understanding of why it is effective, and investigation of structurally related compounds is lacking. For instance, it might be expected that diphenyl sulfide (DPS) and diphenyl selenide (DPSe), which have similar molecular structures to DPE, may also be good candidates for non-halogenated solvent additives and yield improved device performance. Indeed, Y. Xia *et al.* reported that the PCE of a newly synthesized donor polymer:$PC_{71}BM$-based PSCs was greatly improved from 0.21% to 4.43% when DPS was used as a solvent additive.[91] Although DPS showed outstanding properties as solvent additive, there are still no reports which thoroughly investigate the structure-property-function relationships for this additives (DPE, DPS and DPSe, so called DPX) to PSC performances.

In this work, the photovoltaic characteristics of poly[4,8-bis(5-(2-ethylhexyl)thiophen-2-yl)benzo[1,2-b:4,5-b′]dithiophene-co-3-fluorothieno[3,4-b]thiophene-2-carboxylate] (PTB7-Th):$PC_{71}BM$ PSCs were investigated using the series of DPX additives with CB as the main solvent. Compared to control devices (without additives), all three DPX additives dramatically enhanced the short-circuit current density (J_{SC}) from 13.0 mA cm^{-2} to over 16.0 mA cm^{-2} due to desirable, phase-separated film morphologies. The PSCs using DPS showed the best photovoltaic performance among the three solvent additives, with up to 9.08% PCE, while devices using DPE also showed high PCEs of 8.85%. Devices with DPSe, however, exhibited significantly lower PCEs of 5.91% or less, largely due to low open-circuit voltages (V_{OC}) of only 0.68 V (compared to ~0.80 V for the other additives). Analysis of the carrier dynamics in these devices reveals that the low PCE in DPSe devices originates from high surface recombination. Devices with DPS, however, exhibited negligible bimolecular recombination and efficient charge separation and extraction. Furthermore, DPX additives were investigated using

TMB as a main solvent in a completely non-halogenated solvent system. PSCs with DPS additive showed excellent photovoltaic properties with excellent PCE (8.24%), comparable to devices fabricated using CB. This report marks the first of its kind to provide a detailed, structure-function analysis of the class of additives based on the DPX topology to polymer BHJ films and photovoltaic device performances. Furthermore, PSCs with DPS exhibited the best device performances (PCE over 9%), suggesting it can be useful to fabricate PSCs through environmental-friendly solution processes.

3.2 Experimental Details

General: PTB7-Th and PC$_{71}$BM were purchased from 1-Material and Organic Semiconductor Materials (OSM, Republic of Korea), respectively. Diphenyl ether and diphenyl sulfide were purchased from Sigma Aldrich and diphenyl selenide was purchased from Alfa Aesar. AFM height and phase images were obtained using a Veeco AFM microscope in tapping mode. Grazing incidence wide-angle X-ray scattering (GIWAXS) measurements were carried out at the PLS-II 9A U-SAXS beam line of Pohang Accelerator Laboratory, Republic of Korea.

Fabrication and characterization of PSCs: PSC devices were prepared with a conventional structure of glass/indium tin oxide (ITO)/poly(3,4-ethylenedioxythiophene):polystyrene sulfonate (PEDOT:PSS)/active layer/Al. Patterned ITO coated glass substrates were cleaned by ultra-sonication with deionized water, acetone and isopropyl alcohol. Then the substrates were dried in an oven at 100 °C overnight. PEDOT:PSS (Baytron, AI 4083) layers were spin coated on ITO substrates, and baked on a hot plate at 140 °C for 10 min in air. After baking, substrates were brought into a N$_2$ filled glove box. For PTB7-Th:PC$_{71}$BM (1:1.5, w/w) PSCs, blend solutions were prepared in chlorobenzene (CB) and 1,2,4-trimethylbenzene (TMB) with 3 vol% of diphenyl ether (DPE), diphenyl sulfide (DPS) and diphenyl selenide (DPSe) with total concentrations of 35 mg mL^{-1} and 30 mg mL^{-1}, respectively. The solutions were stirred at 60 °C overnight prior to spin casting. After coating active layers, substrates were brought into a high vacuum chamber (~10^{-6} Torr), and Al (100 nm) was deposited by thermal evaporation. Device areas were 13 mm^2. Measurements were conducted in a nitrogen filled glove box using a high quality optical fiber to lead the light from a Xenon arc lamp solar simulator. Intensity was calibrated at 100 mW/cm^2 with a standard silicon photodiode. Current density-voltage (*J-V*) characteristics were measured with a Keithley 2635A source measurement unit. Light intensity dependences of short-circuit current density (J_{SC}) and open-circuit voltage (V_{OC}) were measured with neutral density filters. External quantum efficiency (EQE) was measured in the air using an EQE system (Model QEX7) by PV measurements Inc. (Boulder, Colorado).

3.3 Results and Discussion

To analyze the effects of DPX solvent additives on photovoltaic characteristics, we fabricated PSCs with high-performance BHJ active layer: PTB7-Th:PC$_{71}$BM. PTB7-Th is known as a semi-crystalline conjugated polymer, and constitutes an appropriate candidate to check additive effects of DPX, since PTB7-Th has been reported as a widely studied reference material with well-known properties, and also its semi-crystalline characteristics is appropriate for use with DPE.[20, 32] Detailed molecular structures and calculated dihedral angles (by DFT simulation) for the DPX series are shown in **Figure 3.1a** and **Figure 3.1c**, respectively. As the size the heteroatoms ('X' in DPX) become larger, the dihedral angle increases from 34.2° to 37.2° to 47.5° for DPE, DPS and DPSe, respectively. Furthermore, as the 'X' atoms in DPX become heavier, the boiling point (at 760 mmHg pressure) of each solvent increases; 258 °C, 296 °C, and 335 °C for DPE, DPS, and DPSe, respectively. Interestingly, the melting point of DPS occurs at the sub-zero temperature of -40 °C, whereas DPE and DPSe have higher melting points of 26 °C and 3 °C, respectively. This stable liquid state of DPS facilitates device fabrication regardless of ambient temperatures in research laboratories or factories.
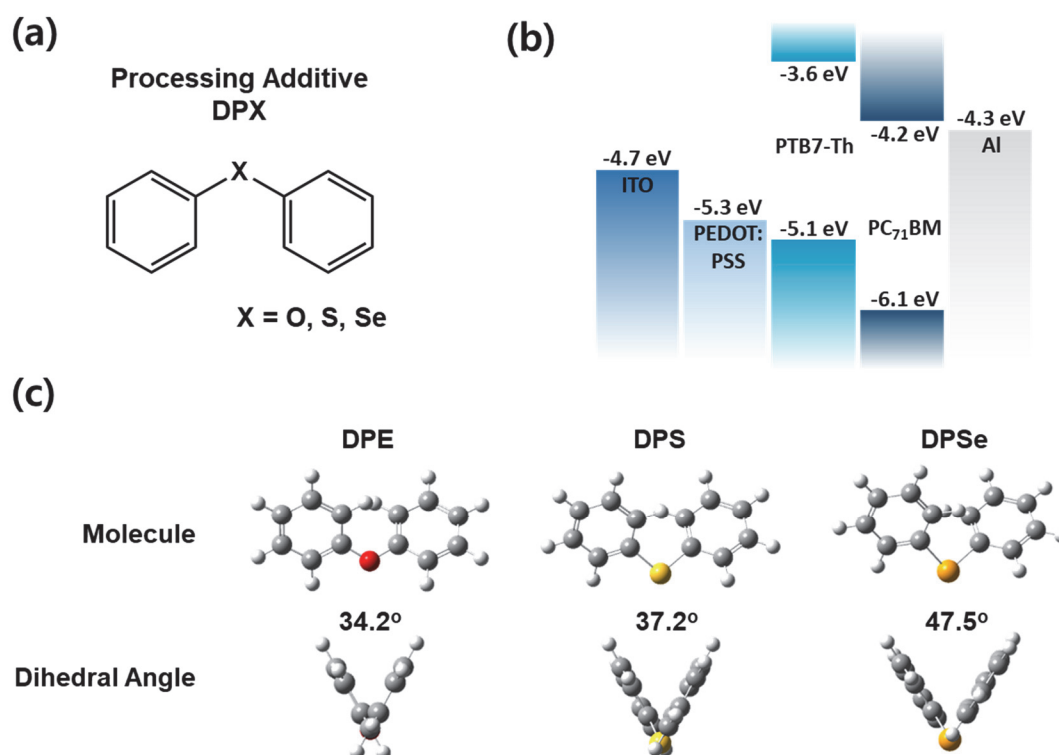
Figure 3. 1. (a) Molecular structure of DPX processing additives. (b) Energy band diagram of PTB7-Th:PC$_{71}$BM PSCs. (c) Detailed molecular structure and dihedral angles of DPX additives calculated by DFT.
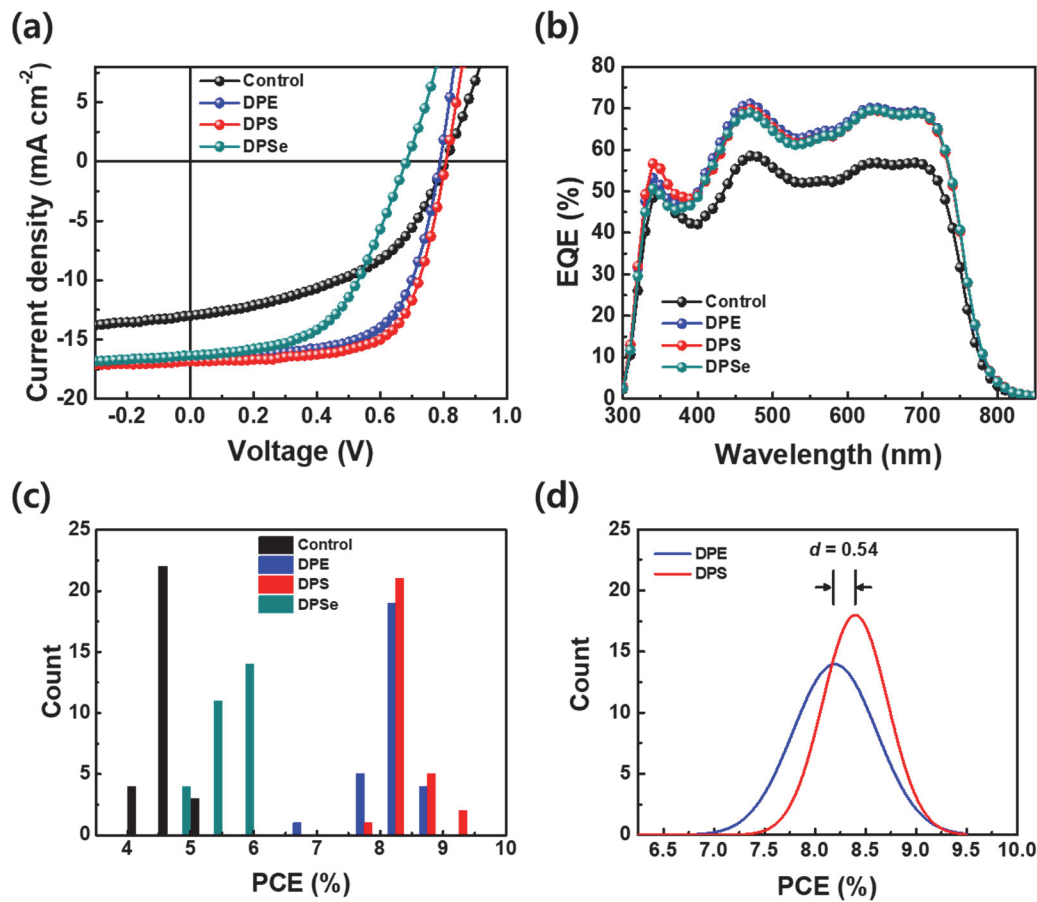
Figure 3. 2. (a) *J-V* characteristics, (b) EQE spectra and (c) statistical histogram of PTB7-Th:PC$_{71}$BM PSCs with different solvent additives. (d) Normal distribution curve for PCE values with comparison between DPE and DPS devices. (*d* is calculated as Cohen's *d* which is a statistical term.)

PSCs were fabricated in conventional structures with the architecture: indium tin oxide (ITO)/poly(3,4-ethylenedioxythiopene) polystyrene sulfonate (PEDOT:PSS)/PTB7-Th:PC$_{71}$BM/Al. A corresponding energy band diagram is shown in **Figure 3.1b**. For the active layer (PTB7-Th:PC$_{71}$BM), CB was used as the main solvent and 3 vol% of DPX processing additives were added. Detailed device fabrication procedures are described in the *Experimental Section*. Photovoltaic properties of the PSCs were investigated by comparison with control devices (only CB used) and CB + 3vol% DPX devices. Corresponding current density–voltage (*J-V*) curves and external quantum efficiency (EQE) spectra are shown in **Figure 3.2a** and **3.2b**, respectively. Detailed photovoltaic parameters are described in **Table 3.1**. Control devices with no additives showed low PCEs of 4.98% or less, whereas devices processed with DPX showed higher PCEs of 8.85%, 9.08% and 5.91% for DPE, DPS and DPSe, respectively. Except for DPSe devices, both DPE and DPS devices showed excellent performance. In particular, DPS devices exhibited the best photovoltaic device performance including a *J*$_{SC}$ of 16.8 mA cm^{-2}, *V*$_{OC}$ of

0.81 V and FF of 0.67, leading a PCE over 9%. Furthermore, as shown in statistical distribution of PCE as shown in **Figure 3.2c**, the average PCE (PCE_{avg}) of DPS devices is around 8.4% while PCE_{avg} of DPE devices was around 8.2%. We also calculate Cohen's d value which is defined as the difference two means divided by a standard deviation for the data, in statistic, providing a quantitative difference for specific phenomenon between two independent groups. Since the difference between PCE_{avg} of DPE and DPS devices is very small around 0.2%, it is better to describe this difference by calculating Cohen's d. If Cohen's d values are 0.2, 0.5 and 0.8, it indicates small, medium and large effect, respectively. As shown in **Figure 3.2d**, calculated Cohen's d is 0.54 which means the upper 50% in statistical distribution of PCE values in DPS devices exceeds upper 69.1% of PCE values in DPE devices. This small but statistically significant increase in PCE in DPS devices (compared to DPE devices) is related to reduced bimolecular recombination, which will be discussed subsequently. Compared to DPE and DPS devices, the J_{SC} of DPSe devices was a similar value of 16 mA cm^{-2} however, the V_{OC} and FF were significantly lower at 0.68 V and 0.53, respectively. The reason for low V_{OC} and FF in DPSe devices may originate from surface recombination or traps which render DPSe an ineffective processing additive, despite an improved J_{SC}.

Table 3. 1. Summary of photovoltaic parameters of PTB7-Th:PC$_{71}$BM PSCs processed with different solvent additives.

Solvent	Solvent additive (3 vol%)	J_{SC} [mA cm^{-2}]	V_{OC} [V]	FF	PCE [%]
CB[a]	Control	13.0 (12.4 ± 0.51)	0.80 (0.79 ± 0.02)	0.48 (0.48 ± 0.01)	4.98 (4.80 ± 0.24)
	DPE	16.5 (15.6 ± 0.61)	0.80 (0.80 ± 0.01)	0.67 (0.66 ± 0.02)	8.85 (8.20 ± 0.41)
	DPS	16.8 (15.7 ± 0.66)	0.81 (0.80 ± 0.01)	0.67 (0.67 ± 0.01)	9.08 (8.40 ± 0.32)
	DPSe	16.4 (14.8 ± 0.75)	0.68 (0.70 ± 0.03)	0.53 (0.53 ± 0.03)	5.91 (5.45 ± 0.34)
TMB[b]	Control	14.9 (14.0 ± 0.46)	0.76 (0.76 ± 0.01)	0.53 (0.53 ± 0.02)	6.06 (5.61 ± 0.32)
	DPE	16.5 (15.3 ± 0.65)	0.78 (0.78 ± 0.00)	0.62 (0.63 ± 0.01)	8.02 (7.50 ± 0.26)
	DPS	16.1 (15.2 ± 0.65)	0.79 (0.79 ± 0.00)	0.65 (0.65 ± 0.01)	8.24 (7.80 ± 0.31)
	DPSe	15.3 (14.9 ± 0.33)	0.72 (0.69 ± 0.02)	0.49 (0.49 ± 0.01)	5.43 (5.05 ± 0.22)

To investigate the influence of processing additives on film morphologies in detail, we first analyzed the molecular ordering and packing structures of PTB7-Th:PC$_{71}$BM blend films via grazing incidence wide-angle X-ray scattering (GIWAXS). As shown in **Figure 3.3**, all of the film processing conditions showed negligible differences in GIWAXS pattern images and line-cut profiles, except for a slight enhancement of the (100) peak intensity for DPX films along the q_z direction. This indicates that DPX does not strongly affect the molecular ordering of BHJ films, although (100) lamellar interactions in the q_z direction were slightly strengthened by DPX additives.
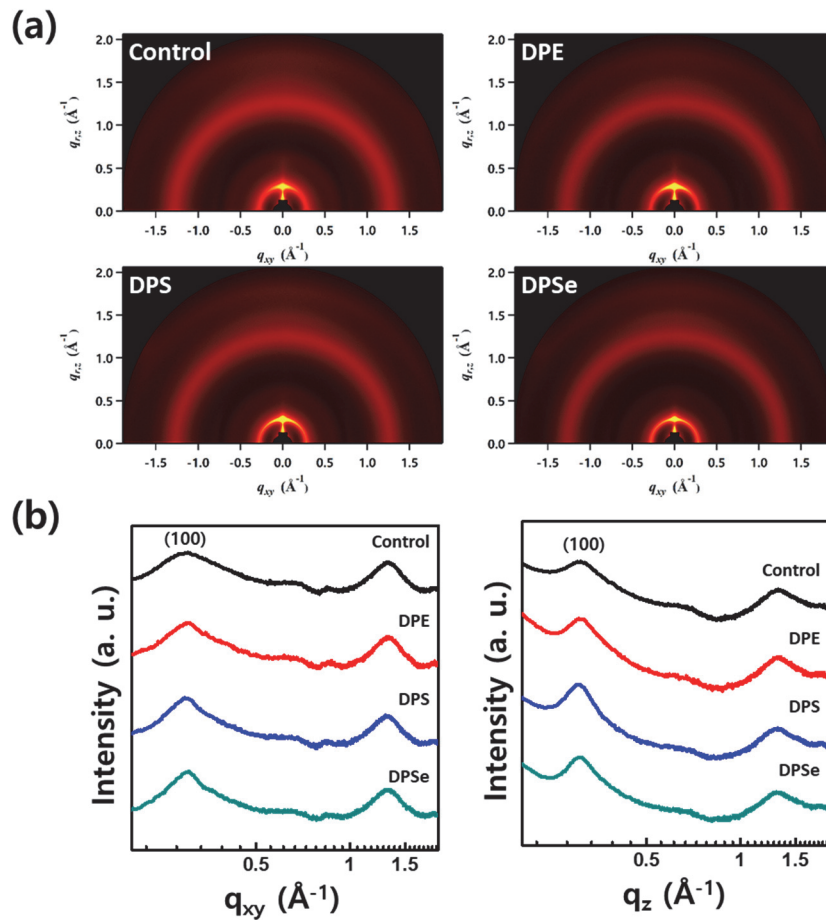
Figure 3. 3. (a) 2D GIWAXS images and (b) line-cut profiles for PTB7-Th:PC$_{71}$BM blend films processed with different solvent additives.

We also analyzed PTB7-Th:PC$_{71}$BM blend films via atomic force microscopy (AFM), in order to characterize the surface morphologies. As shown in **Figure 3.4**, a lot of aggregated features with large domain size (~100 nm) were observed for control films with no additives, and this large domains might be attributed to the fullerene-rich regions.[92] These control films exhibited an RMS roughness of 3.43 nm; the morphologies and roughness are consistent with previously reported results for PTB7-Th:PC$_{71}$BM BHJs.[92-93] However, upon using DPX additives, the aggregation was significantly reduced with decreased RMS roughness of 1.55 nm, 1.75 nm and 1.81 nm for DPE, DPS and DPSe, respectively. Furthermore, relatively small aggregated features are evenly distributed throughout the film compared to control films, which suggests that the surface area between donor and acceptor phases is larger for all films processed with DPX additives, which is consistent with the increase J_{SC}s from 13 mA cm^{-2} to more than 16 mA cm^{-2} upon processing with all three DPX additives. Therefore, DPX additives helps to form well phase-separated film morphologies without changing intermolecular ordering and packing properties, which is similar phenomenon with reported study.[20]
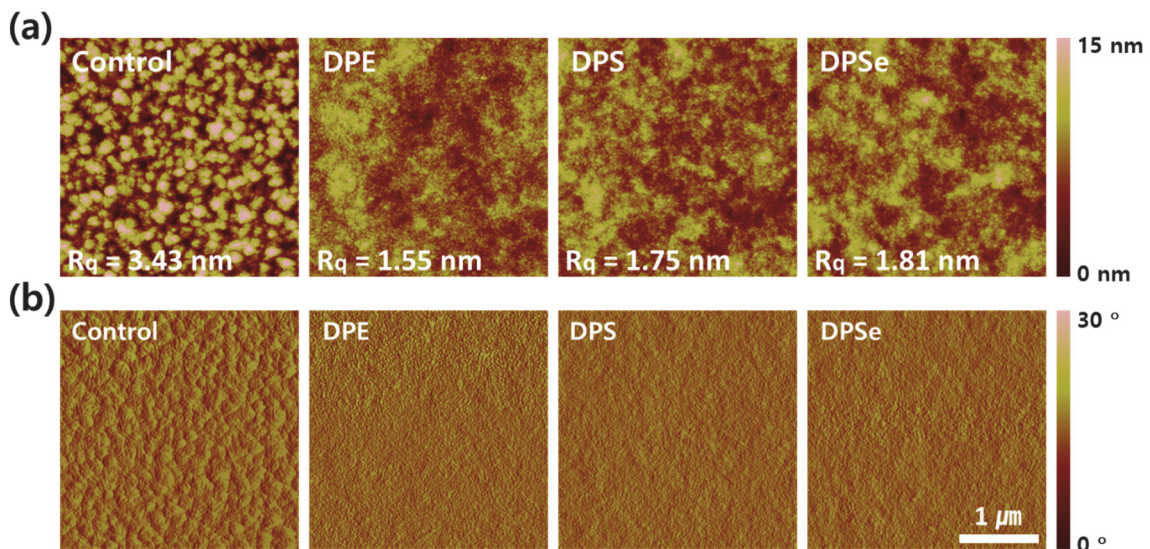
Figure 3. 4. AFM (a) topographical and (b) phase images for PTB7-Th:PC$_{71}$BM blend films processed with different solvent additives
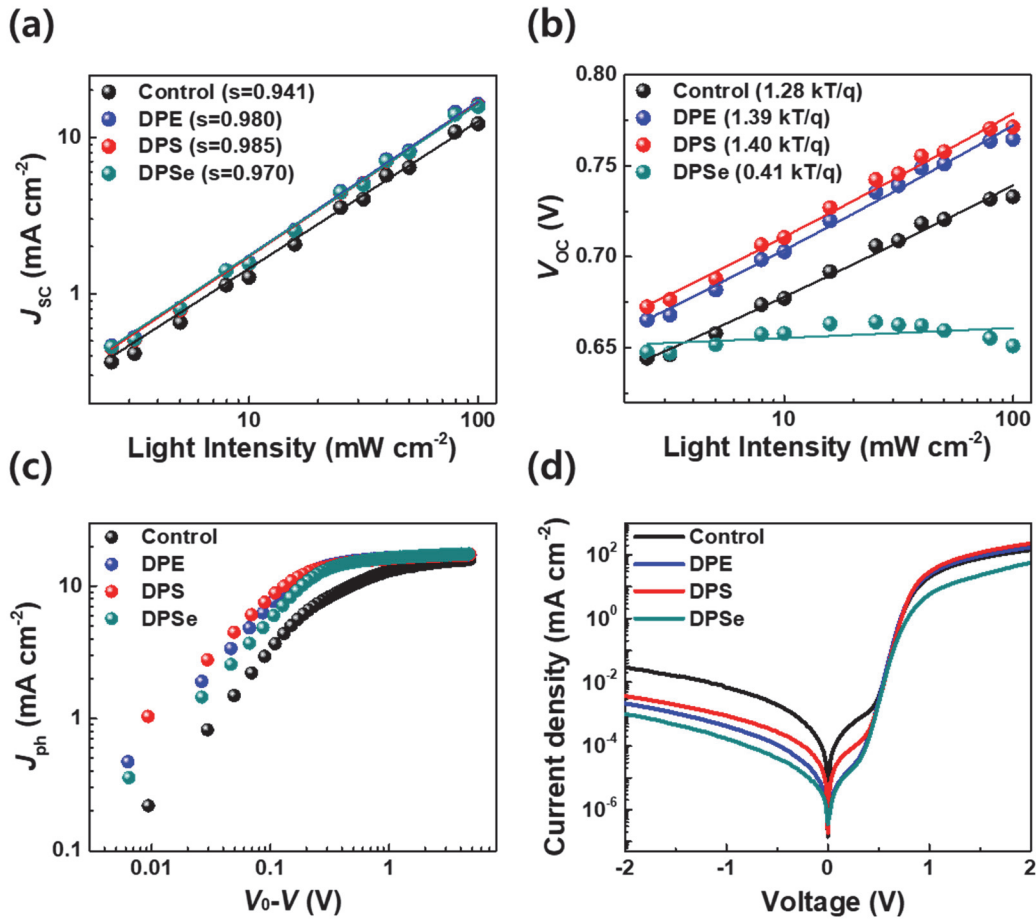
Figure 3. 5. Light intensity dependent (a) J_{SC} and (b) V_{OC} of PTB7-Th:PC$_{71}$BM PSCs. (c) Photocurrent density (J_{ph}) – effective voltage ($V_{eff} = V_0 - V$) and (d) dark current density (J_D) – voltage (V) characteristics for PTB7-Th:PC$_{71}$BM PSCs.

To elucidate the mechanisms of charge recombination in PSCs processed with and without DPX additives, light intensity (I_{light}) dependent J_{SC} and V_{OC} values were measured. In general, J_{SC} follows a power law of $J_{SC} \propto I_{light}^s$, where I_{light} is the incident light intensity and s is an exponent. As s approaches unity, this indicates that bimolecular recombination rates approach zero, whereas decreasing values of s indicate increasing rates of bimolecular recombination.[94] As shown in **Figure 3.5a**, the control device with no additive showed the lowest s value of 0.941, which is consistent with poor photovoltaic performance. For devices processed with DPX additives, DPS yielded the highest s value among the three additives of 0.985, indicating that it has the greatest ability to reduce bimolecular recombination, resulting in excellent PSC performance. DPE also showed a similar s value of 0.980. However, in DPSe devices, a significantly lower s value of 0.970 was obtained, indicating that the poor device performance relative to DPS and DPE originates, in part, from higher bimolecular recombination rates.

If bimolecular recombination is the only loss mechanism in a given BHJ system, the V_{OC} follows equation (3-1);

$$V_{OC} = \frac{E_{gap}}{q} - \frac{kT}{q} \ln \left[\frac{(1-P_D)\gamma N_C^2}{P_D G} \right] \qquad (3\text{-}1)$$

where E_{gap} is the energy difference between the $HOMO_{donor}$ and $LUMO_{acceptor}$, q is the elementary charge, k is the Boltzmann constant, T is temperature in Kelvin, P_D is the dissociation probability of the electron (e)-hole (h) pairs, γ is the Langevin recombination constant, N_C is the effective density of states, and G is the generation rate of bound e-h pairs. Since G is the only parameter directly proportional to I_{light}, we can obtain information about the existence of additional trap-assisted recombination from V_{OC} vs. $\ln(I_{light})$ plots.[94-95] As shown in **Figure 3.5b**, control devices showed a slope of 1.28 kT/q, while the slope values for DPE, DPS and DPSe devices were observed to be 1.39, 1.40 and 0.41 kT/q, respectively. Although the slope value of control devices was closest to kT/q (which indicates the lowest rate of trap-assisted recombination among all conditions), considering these results together with J_{SC} vs. I_{light}, indicates that the combination of relatively high rates of bimolecular recombination and low rates of trap-assisted recombination together resulted overall poor device performance. Similarly, although DPE and DPS devices showed slightly higher trap-assisted recombination compared to control devices, their negligible bimolecular recombination leads to superior device performance. In the case of DPSe devices, however, an unusual slope value lower than kT/q was observed which indicates a high rate of surface recombination, rather than trap-assisted recombination, leading to a limited V_{OC}.[96-98]
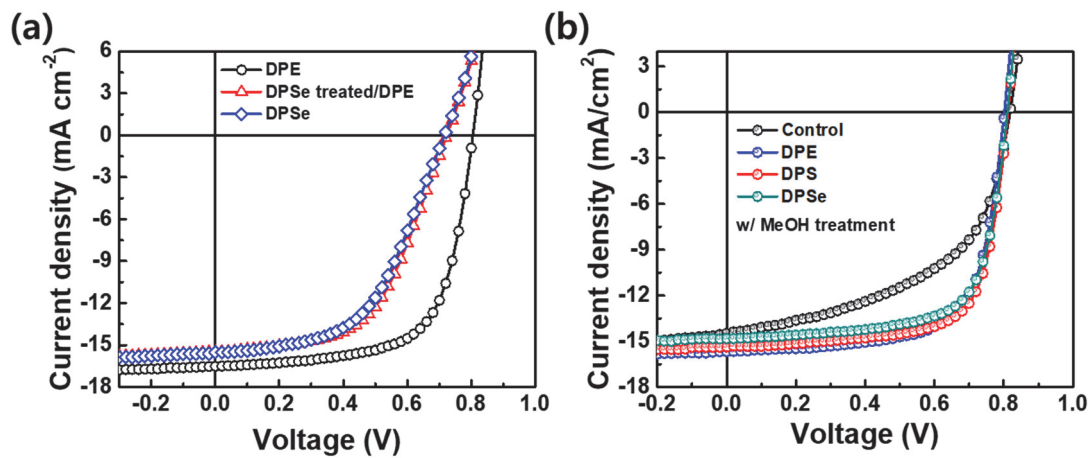
Figure 3. 6. *J-V* characteristics of PTB7-Th:PC$_{71}$BM PSCs processed (a) under various conditions and (b) with methanol treatment.

Table 3. 2. Summary of photovoltaic parameters for PTB7-Th:PC$_{71}$BM PSCs processed under various conditions.

Device Structure	J_{SC} [mA cm^{-2}]	V_{OC} [V]	FF	PCE [%]
PEDOT:PSS/Active Layer (3% DPE)	16.0	0.80	0.66	8.53
PEDOT:PSS/3% DPSe treated/Active Layer (3% DPE)	15.5	0.72	0.55	6.16
PEDOT:PSS/Active Layer (3% DPSe)	15.5	0.72	0.53	5.87

Table 3. 3. Summary of photovoltaic parameters for PTB7-Th:PC$_{71}$BM PSCs processed with methanol treatment.

Solvent additive (3 vol%)	J_{SC} [mA cm^{-2}]	V_{OC} [V]	FF	PCE [%]
Control	14.5	0.82	0.52	6.16
DPE	15.7	0.80	0.67	8.74
DPS	15.4	0.81	0.70	8.86
DPSe	14.8	0.81	0.70	8.39

To investigate the location of surface recombination in the devices, we fabricated a device with configuration of ITO/PEDOT:PSS/3% DPSe/Active Layer (3% DPE)/Al, where 3% DPSe indicates spin-coating of CB + 3 vol% DPSe solvents on the PEDOT:PSS layer. As shown in **Figure 3.6a** and **Table 3.2**, this device showed similar device characteristics to those processed with DPSe in the active layer; therefore we consider that the surface recombination in DPSe devices occurs at the boundary between PEDOT:PSS and the active layer. Furthermore, due to the high boiling point of DPSe, the residual solvent additives in BHJ films may lead to poor device performance. To confirm this, we fabricated PSCs with methanol (MeOH) treatment which can remove residual solvent additives with the following properties of MeOH; poor dissolubility of the active layer but good dissolubility of solvent additive.[99] As shown in **Figure 3.6b** and **Table 3.3**, after MeOH treatment, the *J-V* curve and efficiency were recovered showing comparable PCE of 8.39% with DPE and DPS devices. Therefore, residual DPSe in BHJ films affects not only surface recombination, but also disturbance charge transport.

Table 3. 4. Shunt and series resistances of PTB7-Th:PC$_{71}$BM PSCs calculated from dark J-V curve.

Solvent additive (3 vol%)	R_{sh} [MΩ cm^2]	R_s [Ω cm^2]
Control	0.54	7.25
DPE	10.7	5.92
DPS	2.87	4.27
DPSe	16.9	13.5

Photocurrent density–effective voltage (J_{ph}-V_{eff}) characteristics were collected to investigate charge generation and extraction properties, as shown in **Figure 3.5c**. In control devices, J_{ph} became saturated at high V_{eff} of over 1 V, indicating that a high electric-field was needed to completely separate bound e-h pairs and extract separated charge carriers. In contrast, DPS devices showed rapid J_{ph} saturation at a low V_{eff} of around 0.19 V, while J_{ph} saturation in DPE and DPSe devices at V_{eff} values of around 0.21 and 0.25 V, respectively. The fast and field-independent J_{ph} saturation in DPS devices suggests negligible recombination losses and efficient charge collection under operating conditions. Dark current density–voltage (J_D-V) characteristics were measured as shown in **Figure 3.5d**, and calculated shunt and series resistance (R_{sh} and R_s, respectively) values from J_D-V curve are summarized in **Table 3.4**. Control devices showed poor diode properties due to high leakage current and low shunt resistance. For DPX devices, leakage currents in the shunt regime is an order of magnitude lower than control devices, consistent with high J_{SC}s. However, DPSe showed the highest R_s of 13.5 Ω cm^2 among three DPX devices; this high R_s is related to excessive surface recombination, leading to poor photovoltaic device performance.[98]
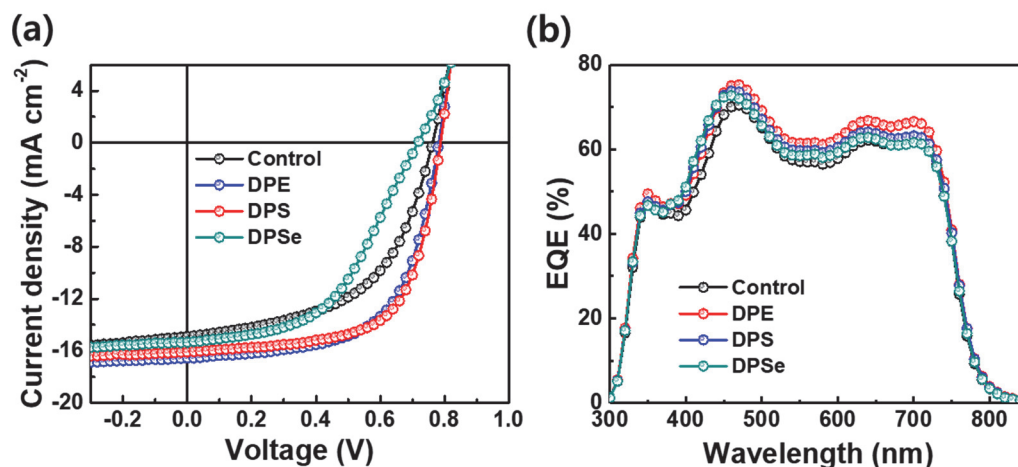
Figure 3. 7. (a) *J-V* characteristics and (b) EQE spectra for PTB7-Th:PC$_{71}$BM PSCs using 1,2,4-trimethylbenzene as a primary solvent.

To confirm that the three DPX solvent additives are effective in non-halogenated host solvents, as opposed to CB, we fabricated PSCs using fully-nonhalogenated solvent systems including 1,2,4-trimethylbenzene (TMB) as the primary solvent with three DPX compounds as solvent additives. Corresponding *J-V* curves and EQE spectra are shown in **Figure 3.7** and summary of photovoltaic parameters is described in **Table 3.1**. Among all conditions, DPS devices again yielded the highest PCEs of up to 8.24%, with corresponding J_{SC} of 16.1 mA cm^{-2}, V_{OC} of 0.79 V and FF of 0.65. DPE devices also showed high PCEs of up to 8.02%, whereas control devices and DPSe devices showed lower PCEs of 6.06% and 5.08%, respectively. The consistently outstanding device performance observed in DPS devices fabricated with both CB and TMB as primary solvents suggests the great potential of DPS for PSC fabrication in research laboratories and in industry.

3.4 Conclusion

In conclusion, we have investigated the photovoltaic characteristics, film morphologies and device properties of PTB7-Th:PC$_{71}$BM PSCs using DPE, DPS and DPSe solvent additives. Compared to control devices without additives, all three solvent additives provided increased J_{SC}s of over 16 mA cm^{-2}. This enhancement is attributed to well-phase-separated film morphologies with low RMS roughness (~1.5 nm). PSCs with DPS consistently yielded the best performance among three additives, with PCEs of great than 9%, a small but significant improvement compared to DPE devices, which also showed high PCEs of up to 8.85%. In contrast, DPSe devices showed relatively low PCEs of 5.91% or less, largely due to a low V_{OC}, which originated from significant surface recombination and high series resistance. For DPS devices, quick and field-independent J_{ph} saturation with negligible bimolecular recombination occurred, leading to efficient charge separation and collection and excellent device performance. Finally, we successfully demonstrated the fabrication of PSCs using fully non-halogenated solvent:additive systems incorporating TMB as a primary solvent and DPX materials as solvent additives. Using TMB as the main solvent, DPS devices showed excellent PCEs of up to 8.24%, while DPE devices also showed high PCEs of up to 8.02%, while DPSe devices showed low PCEs of ~ 5%. We confirmed that DPS is the most effective solvent additive for use in PSCs by comparison of the three diphenyl chalcogenide additives. This work demonstrates the suitability of DPS as an effective non-halogenated solvent additive for PSC fabrication, offering the possibility of safe and stable solution-processing using non-halogenated solvents in ambient conditions considerations which are greatly needed for the industrial development and commercialization of PSCs.

Chapter 4. Alkoxybenzothiadiazole-Based Fullerene and Nonfullerene Polymer Solar Cells with High Shunt Resistance for Indoor Photovoltaic Applications

4.1 Research Backgrounds

Polymer solar cells (PSCs) have attracted growing attention over the past decades due to their facile fabrication (via solution process), cost effectiveness, light weight and great potential for flexible and large-area electronic devices.[10, 100-101] Recently, power conversion efficiencies (PCEs) up to 12~13% have been reported in PSCs, surpassing the PCE of amorphous silicon-based solar cells.[33, 102-103] One very attractive property of PSCs is that under dim light, the devices show better photovoltaic performance than their inorganic counterparts. In the case of commercialized crystalline silicon (c-Si) solar cells, it is well known that PCE increases as increasing light intensity until series resistance (R_s) influences device performance.[104] When the light intensity decreases, however, the PCE decreases; the relatively low shunt resistance (R_{sh}) limits device performance when the photo-generation rate of charge carriers decreases under dim light.[105] In real applications, the sun light intensity changes over time, location, weather or surrounding environment. For example, on a cloudy day, the light intensity may decrease to as low as 1/50 the intensity of a typical sunny day. Additionally, incident angle of light may vary the intensity of sunlight from 104 mW cm^{-2} (AM1, at zenith angle 0°) to 2 mW cm^{-2} (AM38, at zenith angle 90°) depending on the location in the earth. Therefore, for practical applications of PSCs, both standard (100 mW cm^{-2}) and dim lighting conditions should be considered together. By extension, the investigation of photovoltaic behavior under dim light is also necessary for indoor photovoltaic power-supply systems i.e., low-power consumed electronic devices, Internet of Things (IoT) sensors, actuators, etc.[106-107] N. H. Reich *et al.* reported that the PCE of c-Si solar cells drastically decreased from 20% to ~13% when the incident light intensity decreased from 100 mW cm^{-2} to 0.3 mW cm^{-2}; this significantly hinders the indoor application of silicon solar cells.[105] In contrast to inorganic solar cells, slightly increased PCEs are often observed in PSCs as the incident light intensity decreases. Recently, interesting papers on indoor applications of PSCs have been reported, for instance, R. Steim *et al.* reported that the photovoltaic properties of PSCs under different illumination intensities are closely related to their series and shunt resistances.[108] H. K. H. Lee *et al.* recently reported a comparison of photovoltaic performance of PSCs under AM 1.5G illumination (100 mW cm^{-2}, 1 sun) and fluorescent

lamp illumination (300 lx). In this report, poly[N-9′-heptadecanyl-2,7-carbazole-alt-5,5-(4′,7′-di-2-thienyl-2′,1′,3′-benzothiadiazole)] (PCDTBT):[6,6]-phenyl C_{71} butyric acid methyl ester ($PC_{71}BM$) bulk-heterojunction (BHJ) PSCs showed 16.6% PCE under fluorescent lamp illumination, which is much higher compared to AM 1.5G illumination (PCE = 6.0%), demonstrating the great potential of PSCs for indoor applications.[109] Despite interesting reports on the properties of PSCs under different light intensities, detailed investigations on the underlying mechanisms and photovoltaic behaviors under dim lighting conditions are still lacking. Currently, there is little understanding on how to design molecules to increase R_{sh} and morphology−R_{sh} relationship, etc., which will be the critical issues for further optimization of indoor PSCs.

Herein, we have synthesized three semi-crystalline photovoltaic polymers based on the dialkyloxy substituted benzothiadiazole (BT), poly(5,6-bis(butyloctyloxy)-4-(thieno[3,2-b]thiophene-2-yl)-benzo[c][1,2,5]thiadiazole) ($PTTBT_{BO}$), poly(5,6-bis(butyloctyloxy)-4-(2,2′-bithiophene-5-yl)-benzo[c][1,2,5]thiadiazole) ($PDTBT_{BO}$) and poly(5,6-bis(butyloctyloxy)-4-(3,3′-difluoro-2,2′-bithiophene-5-yl)-benzo[c][1,2,5]thiadiazole) ($P2FDTBT_{BO}$) as donor materials and studied their photovoltaic behaviors upon blending with the acceptors $PC_{71}BM$ or 3,9-bis(2-methylene-(3-(1,1-dicyanomethylene)-indanone))-5,5,11,11-tetrakis(4-hexylphenyl)-dithieno[2,3-d:2′,3′-d′]-s-indaceno[1,2-b:5,6-b′]dithiophene (ITIC) under different illumination intensities. The best photovoltaic performance was measured for $PDTBT_{BO}$:$PC_{71}BM$, showing a PCE of 7.52% under standard (100 mW cm^{-2}) light which increased by 28% (PCE: 9.60%) under dim light (2.50 mW cm^{-2}). Very interestingly, the PCE was dramatically increased by 2.3 times (3.69% to 8.33%) for $P2FDTBT_{BO}$:$PC_{71}BM$ PSCs under dim light. Due to the large R_s (9.42 Ω cm^2) of $P2FDTBT_{BO}$ device (see 5.26 Ω cm^2 for $PDTBT_{BO}$:$PC_{71}BM$), significant bimolecular and surface charge recombinations were measured, showing poor PCE under standard light. The improved PCE in $P2FDTBT_{BO}$ PSCs under weak light intensity mainly originates from the sustained open-circuit voltage (V_{OC}) and enhanced fill factor (FF) values. The steady V_{OC} can be understood in terms of the small R_s-induced voltage drop due to the small photocurrent under dim light. The remarkable enhancement of PCE in the $P2FDTBT_{BO}$ device was analyzed to be related to exceptionally high R_{sh} (1326 kΩ cm^2), which is an essential parameter to avoid leakage current under dim light (see 581 kΩ cm^2 for $PDTBT_{BO}$:$PC_{71}BM$). $P2FDTBT_{BO}$ showed compact crystalline packing (d-spacing of ~3.8 Å), which may be related to its high R_{sh}. Consequently, field-independent saturation of photocurrent was observed as the light intensity decreased, which suggests efficient charge transport and extraction with negligible charge recombination under dim light. Similar data were also measured for polymer:ITIC nonfullerene PSCs. The $PTTBT_{BO}$ devices with a large R_s and small R_{sh} showed poor photovoltaic properties under both standard and dim light illumination. At a present stage, we do not understand clearly how to design ideal indoor photovoltaic molecules to increase R_{sh}. The crystalline morphology must be one main parameter to be considered. We believe that

our current study may provide valuable information to understand the origin of high shunt resistance in terms of molecular design and morphology for indoor PSCs development. In addition, high R_{sh} is essential whereas R_s is less critical under dim light, which may allow a greater room for designing indoor photovolatic materials.

4.2 Experimental Details

General: ^{1}H and ^{13}C NMR spectra were recorded on a Bruker Advance III HD system operating at 500 MHz and 125 MHz, respectively. UV-vis spectra were obtained with a Jasco V-630 spectrophotometer. Cyclic voltammetry data were measured on a Versa STAT3 (Princeton Applied Research) with a three-electrode cell employing a platinum wire as the counter electrode, a platinum electrode coated with a thin polymer film was used as the working electrode, with Ag/Ag$^+$ as the reference electrode in 0.1 M tetrabutylammonium tetrafluoroborate (Bu$_4$NBF$_4$) in CH$_3$CN at a scan rate of 50 mV/s. Thermogravimetric analysis (2050 TGA V5.4A) and differential scanning calorimetry (DSC Q200 V24.4) measurements were performed at a heating and cooling rate of 10 °C/min under nitrogen (purity, 99.999%). Grazing incidence wide-angle X-ray scattering (GI-WAXS) measurements were carried out at the PLS-II 9A U-SAXS beam line of Pohang Accelerator Laboratory, Republic of Korea.

Synthesis: All reagents were purchased from Aldrich, Tokyo Chemical Industry, Junsei Chemical and used without further purification. 4,7-Dibromo-5,6-bis[(2-butyloctyl)oxy]-2,1,3-benzothiadiazole (**1**) and 2,5-bis(trimethylstannyl)thieno[3,2-b]thiophene (**2**), 5,5′-bis(trimethylstannyl)-2,2′-bithiophene (**3**) and 5,5′-bis(trimethylstannyl)-3,3′-difluoro-2,2′-bithiophene (**4**) were prepared according to the previously reported literature procedures.[39, 110]

Poly(5,6-bis(butyloctyloxy)-4-(thieno[3,2-b]thiophene-2-yl)-benzo[c][1,2,5]thiadiazole) *(PTTBT$_{BO}$).* In a N$_2$ filled glove box, monomer (**1**) (200 mg, 0.302 mmol), monomer (**2**) (140.6 mg, 1 equiv.), tris(dibenzylideneacetone)dipalladium(0) (2 mol%), tri(o-tolyl)phosphine (8 mol%) and toluene (1.5 mL) were added in a 5 mL microwave vial. The reaction mixture was heated at 80 °C for 3 min, at 100 °C for 5 min, at 125 °C for 45 min and at 150 °C for 55 min in a microwave reactor. After cooling the reaction solution, the polymer was end-capped by addition of 2-tributylstannylthiophene (0.1 equiv.) and the mixture was further reacted at 145 °C for 20 min. After cooling the solution, 2-bromothiophene (0.2 equiv.) was added by a syringe and the reaction solution was heated at 145 °C for another 20 min. After the reaction was finished, the crude PTTBT$_{BO}$ polymer was precipitated into 300 mL methanol, filtered and further purified by Soxhlet extraction with acetone, hexane and chloroform. The extracted polymer in chloroform was precipitated into MeOH, filtered and dried under vacuum (Yield: 68.3%). Number average molecular weight (M_n) = 44 kDa, polydispersity index (PDI) = 2.8. ^{1}H

NMR (500 MHz, CDCl$_3$): δ (ppm) 8.67 (s, 2H), 4.07 (br, 4H), 2.10 (br, 2H), 1.38-1.00 (br, 32H), 0.83 (br, 12H).

Poly(5,6-bis(butyloctyloxy)-4-(2,2'-bithiophene-5-yl)-benzo[c][1,2,5]thiadiazole) *(PDTBT$_{BO}$)*. PDTBT$_{BO}$ was synthesized similarly as PTTBT$_{BO}$. Yield: 71.5%. M_n = 35 kDa, PDI = 2.2. ^{1}H NMR (500 MHz, CDCl$_3$): δ (ppm) 8.32 (d, *J*= 5 Hz, 2H), 7.41 (d, *J*= 5 Hz, 2H), 4.25- 3.60 (d, *J*= 5 Hz, 4H), 2.11-2.04 (m, 2H), 1.60-1.20 (m, 32H), 0.93-0.83 (m, 12H).

Poly(5,6-bis(butyloctyloxy)-4-(3,3'-difluoro-2,2'-bithiophene-5-yl)-benzo[c][1,2,5]thiadiazole) *(P2FDTBT$_{BO}$)*. P2FDTBT$_{BO}$ was synthesized similarly as PTTBT$_{BO}$. Yield: 64.5%. M_n = 36 kDa, PDI =3.0. ^{1}H NMR (500 MHz, CDCl$_3$): δ (ppm) 8.64-8.36 (br, 2H), 4.30- 3.90 (br, 4H), 2.25-2.45 (br, 2H), 2.10-1.05 (br, 32H), 1.05-0.70 (br, 12H).

Fabrication and characterization of PSCs: The PSC devices were prepared with a conventional structure of glass/indium tin oxide (ITO)/poly(3,4-ethylenedioxythiophene):polystyrene sulfonate (PEDOT:PSS)/active layer/Al. Patterned ITO coated glass substrates were cleaned by ultra-sonication with deionized water, acetone and isopropyl alcohol. Then the substrates were dried in an oven at 100 °C overnight. The PEDOT:PSS (Baytron, AI 4083) layer was spin coated on the ITO substrate, and baked on a hot plate at 140 °C for 10 min in the air. After baking, the substrates were brought into a N$_2$ filled glove box. For polymer:PC$_{71}$BM (1:2, w/w) PSCs, the blend solutions were prepared in chlorobenzene (CB) with 2 vol% of 1,8-octanedithiol (ODT) with polymer concentrations of 13, 14, and 10 mg/mL for PTTBT$_{BO}$, PDTBT$_{BO}$, and P2FDTBT$_{BO}$, respectively. For polymer:ITIC (1:1, w/w) PSCs, the blend solutions were prepared in CB with 0.5 vol% of ODT using polymer concentrations of 12, 13, and 9 mg/mL for PTTBT$_{BO}$, PDTBT$_{BO}$, and P2FDTBT$_{BO}$, respectively. Except for PTTBT$_{BO}$ solutions (60 °C), all solutions were stirred at 110 °C overnight before spin casting. After coating active layers, the substrates were brought into a high vacuum chamber (~10^{-6} Torr), and Al (100 nm) was deposited by thermal evaporation. The device area was 13 mm^2. Measurements were conducted in the glove box using a high quality optical fiber to lead the light from a Xenon arc lamp solar simulator (AM 1.5G illumination, 100 mW cm^{-2}). Light intensities were modulated with neutral density filters to measure the light intensity dependent photovoltaic parameters. Current density-voltage (*J-V*) characteristics were measured with a Keithley 2635A source measurement unit, and external quantum efficiency (EQE) was measured in the air using an EQE system (Model QEX7) by PV measurements Inc. (Boulder, Colorado).

4.3 Results and Discussion

Three donor (D)-acceptor (A) type conjugated polymers based on dialkoxybenzothiadiazole were designed by considering intra- and intermolecular noncovalent coulombic interactions (via $S^{\delta+}\cdots O^{\delta-}$, $S^{\delta+}\cdots F^{\delta-}$, etc.), allowing polymers to have a planar backbone and crystalline intermolecular organization.[111-112] The chemical structures of PTTBT$_{BO}$, PDTBT$_{BO}$ and P2FDTBT$_{BO}$ are shown in **Figure 4.1**. The Stille coupling of equimolar quantities of 4,7-dibromo-5,6-bis(2-butyloctyloxy)-2,1,3-benzothiadiazole (1) and 2,5-bis(trimethylstannyl)thieno[3,2-b]thiophene (2) for PTTBT$_{BO}$ or 5,5′-bis(trimethylstannyl)-2,2′-bithiophene (3) for PDTBT$_{BO}$ or 5,5′-bis(trimethylstannyl)-3,3′-difluoro-2,2′-bithiophene (4) for P2FDTBT$_{BO}$ was performed by microwave assisted polymerization with a catalyst of tris(dibenzylideneacetone)dipalladium(0) and tri(*o*-tolyl)phosphine in toluene to afford the resulting three polymers (64%-72% yield). The detailed synthetic procedures for the polymers can be found in the *Experimental Section*. All three polymers were readily soluble in common organic solvents such as chloroform, chlorobenzene and *o*-dicholorobenzene, etc. The number average molecular weights were measured to be 44 kDa (polydispersity index (PDI) = 2.8), 35 kDa (2.2) and 36 kDa (3.0) for PTTBT$_{BO}$, PDTBT$_{BO}$ and P2FDTBT$_{BO}$, respectively, by gel permeation chromatography (GPC) at 80 °C using *o*-dichlorobenzene as the eluent.
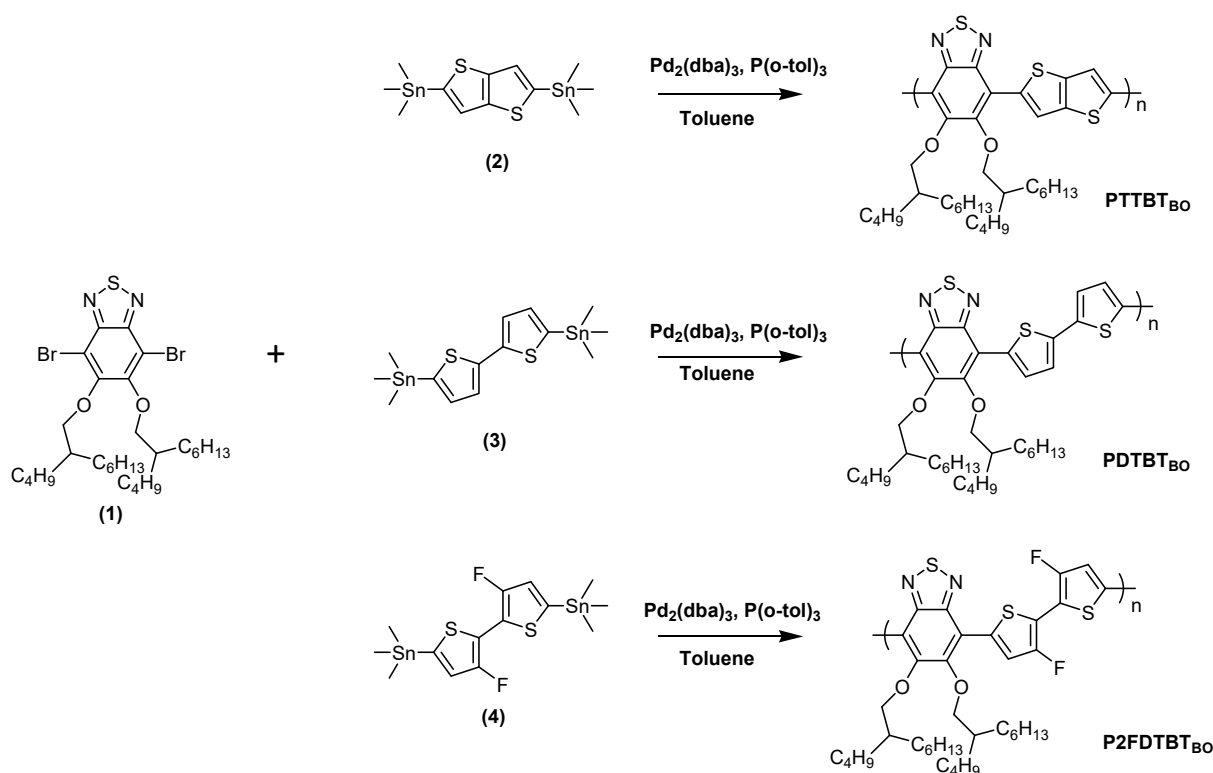
Figure 4. 1. Synthetic route to three polymers.

Table 4. 1. Summary of optical, electrochemical and thermal properties

Materials	M_n(kDa)	PDI	λ_{max} (sol.) [nm]	λ_{max} (film) [nm]	λ_{onset} (film) [nm]	E_g^{opt} (eV)[a]	HOMO (eV)[b]	LUMO (eV)[c]	T_d (°C)[d]
PTTBT$_{BO}$	44	2.8	647	654	736	1.69	-5.51	-3.82	324
PDTBT$_{BO}$	35	2.2	559	626	704	1.76	-5.49	-3.73	308
P2FDTBT$_{BO}$	36	3.0	662	664	761	1.63	-5.57	-3.94	296

[a]Optical band gaps were estimated from the absorption onset of polymer films. [b]HOMO levels were estimated from the tangential onset of oxidation (E_{ox}^{onset}) by CV using the equation: HOMO (eV) $= -(E_{ox}^{onset} - E_{1/2}^{ferrocene} + 4.8)$. [c]LUMO levels were estimated from the HOMO values and optical band gaps. [d]Decomposition temperature (T_d) (with 5% weight-loss) was determined by TGA under nitrogen.

Thermal properties were characterized by thermogravimetric analysis (TGA) and differential scanning calorimetry (DSC) as shown in **Figure 4.2a** and **4.2b**. The onset decomposition temperatures (T_d, 5% weight loss) of PTTBT$_{BO}$, PDTBT$_{BO}$ and P2FDTBT$_{BO}$ were determined to be 324, 308 and 296 °C, respectively (**Table 4.1**). The thermal transitions were analyzed by DSC measurements in a temperature range of 25-275 °C. Among the three polymers, PDTBT$_{BO}$ showed clear phase transitions at 249 °C for melting and at 210 °C for crystallization. Based on the molecular structures, PTTBT$_{BO}$ and P2FDTBT$_{BO}$ might be more crystalline than PDTBT$_{BO}$ due to the chain linearity and the strong $S^{\delta+}\cdots F^{\delta-}$ interchain interactions, etc. These polymers did not exhibit phase transitions within the scan range. Melting and crystallization temperatures may not be detected due to low decomposition temperature of around ~300 °C.
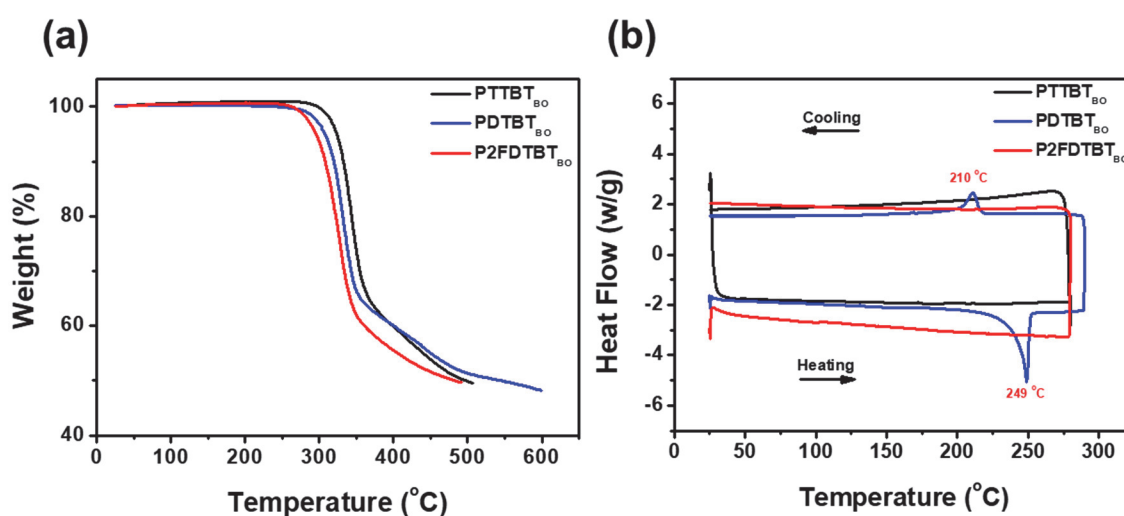
Figure 4. 2. (a) TGA thermograms of PTTBT$_{BO}$, PDTBT$_{BO}$ and P2FDTBT$_{BO}$. (b) DSC thermograms of PTTBT$_{BO}$, PDTBT$_{BO}$ and P2FDTBT$_{BO}$.

UV-Vis absorption spectra of three polymers were recorded in chloroform and as thin films (**Figure 4.5b**). The corresponding parameters are summarized in **Table 4.1**. $PTTBT_{BO}$ and $P2FDTBT_{BO}$ present similar spectra in solution and in film with a clear shoulder peak, indicating a strong interchain organization or pre-aggregation even in dilute solution.[60] The temperature-dependent UV-vis spectra also show a similar trend (**Figure 4.3**). The absorption bands of $PTTBT_{BO}$ and $P2FDTBT_{BO}$ films become broadened with negligible change in absorption maxima (654 nm for $PTTBT_{BO}$ and at 664 nm for $P2FDTBT_{BO}$) relative to those in solution. Significantly different aggregation behavior was observed for $PDTBT_{BO}$ in dilute chloroform solution, showing a clearly blue-shifted and featureless spectrum compared to those of $PTTBT_{BO}$ and $P2FDTBT_{BO}$ in solution. In films, the maximum absorption of $PDTBT_{BO}$ was bathochromically shifted to 626 nm (by 67 nm), which suggests strong interchain packing interactions in film. The optical band gaps of $PTTBT_{BO}$, $PDTBT_{BO}$ and $P2FDTBT_{BO}$ were calculated to be 1.69, 1.76 and 1.63 eV, respectively, from the film absorption edge (**Table 4.1**). Molar absorption coefficients were measured at each maximum absorption wavelength in chloroform ($< 10^{-5}$ mol/L), showing similar molar absorption coefficients of $\varepsilon_{max} = 3.06 \times 10^4$, 2.55×10^4 and 3.04×10^4 $M^{-1} cm^{-1}$ for $PTTBT_{BO}$, $PDTBT_{BO}$ and $P2FDTBT_{BO}$, respectively (**Figure 4.4a**).

Cyclic voltammetry (CV) was employed to investigate the electrochemical properties of $PTTBT_{BO}$, $PDTBT_{BO}$ and $P2FDTBT_{BO}$ (**Figure 4.4b**). The highest occupied molecular orbital (HOMO) levels were calculated from the onset oxidation potentials, assuming the absolute energy level of standard ferrocene and ferrocenium redox couples (Fc/Fc^+) to be 4.8 eV below vacuum. The HOMO levels of $PTTBT_{BO}$, $PDTBT_{BO}$ and $P2FDTBT_{BO}$ were estimated to be -5.51, -5.49 and -5.57 eV, respectively (**Figure 4.5a** and **Table 4.1**) and the LUMO levels were calculated to be -3.82, -3.73 and -3.94 eV for $PTTBT_{BO}$, $PDTBT_{BO}$ and $P2FDTBT_{BO}$, respectively, based on the HOMO values and the corresponding optical band gaps in film.
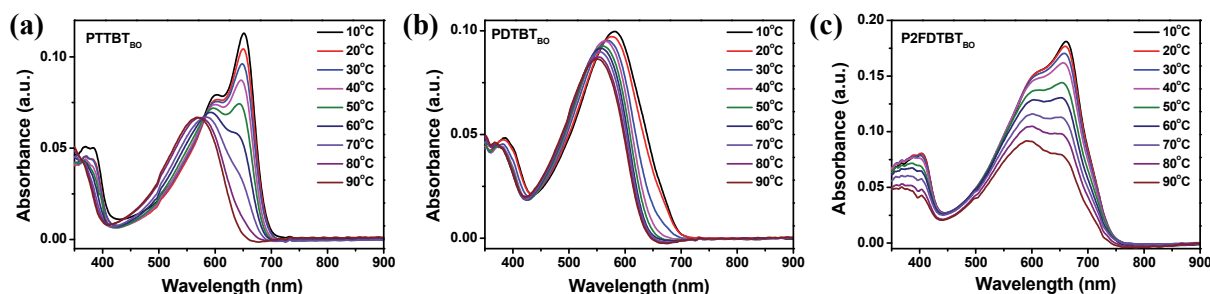
Figure 4. 3. Temperature-dependent absorption spectra of (a) $PTTBT_{BO}$, (b) $PDTBT_{BO}$ and (c) $P2FDTBT_{BO}$ in chlorobenzene at a concentration of 0.02 mg mL^{-1}
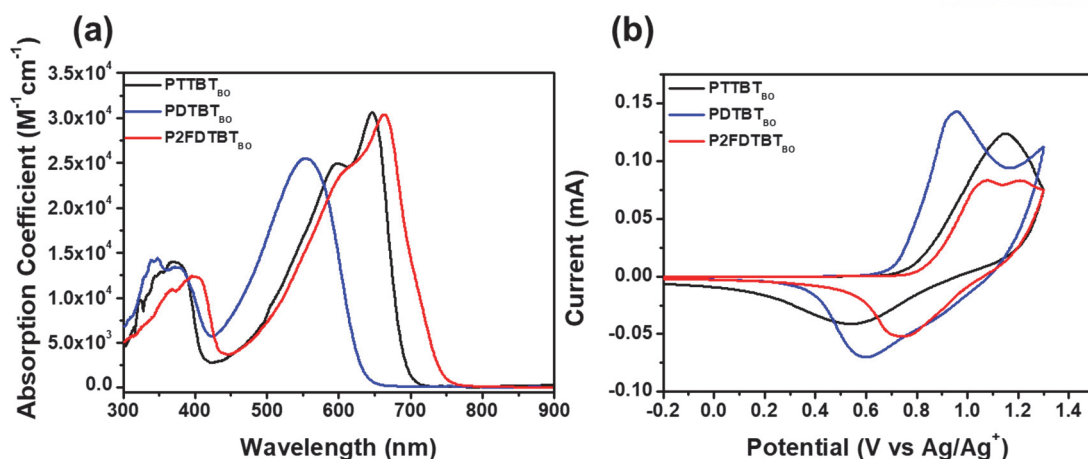
Figure 4. 4. (a) Molar absorption coefficients of three polymers in chloroform. (b) Cyclic votammograms of PTTBT$_{BO}$, PDTBT$_{BO}$ and P2FDTBT$_{BO}$.

To characterize the photovoltaic properties of the three polymers, we utilized two types of acceptors, PC$_{71}$BM and ITIC, which are representative n-type acceptors for fullerene-based and nonfullerene PSCs.[113-115] Devices were fabricated in a conventional architecture of ITO/PEDOT:PSS/active layer/Al. The corresponding energy band diagrams are shown in **Figure 4.5a**. The optimum donor:acceptor ratios were 1:2 and 1:1 (by weight) for polymer:PC$_{71}$BM and polymer:ITIC BHJ devices, respectively. In addition, chlorobenzene was used as a solvent and ODT was used as a processing additive to modulate film morphologies. Detailed device fabrication procedures are described in the *Experimental Section*. The corresponding *J-V* characteristics (under AM 1.5G irradiation) and EQE spectra of polymer:PC$_{71}$BM devices are shown in **Figure 4.5c** and **4.5d**, respectively. The highest photovoltaic performance was measured for PDTBT$_{BO}$ PSCs, showing a peak PCE of 7.52% with a J_{SC} of 13.6 mA cm^{-2}, V_{OC} of 0.86 V and FF of 0.64, respectively. P2FDTBT$_{BO}$ and PTTBT$_{BO}$ PSCs showed 3.69% and 1.50% PCEs, respectively. In the case of nonfullerene PSCs with ITIC as an acceptor, PCEs of 5.41, 2.46 and 1.57% were measured for PDTBT$_{BO}$, P2FDTBT$_{BO}$ and PTTBT$_{BO}$, respectively. Detailed photovoltaic parameters are summarized in **Table 4.2** and **Table 4.3**. To check the data accuracy, we also checked the EQE and calculated (calc.) J_{SC} values by integrating the EQE spectra. The calc. J_{SC} values were found to be 13.8, 15.1 and 8.58 mA cm^{-2} for PDTBT$_{BO}$, P2FDTBT$_{BO}$ and PTTBT$_{BO}$ PSCs with PC$_{71}$BM, respectively. PDTBT$_{BO}$ PSCs showed similar measured and calc. J_{SC} values (13.6 vs. 13.8 mA cm^{-2}). Interestingly, a large discrepancy in the measured and calc. J_{SC} values was observed for PTTBT$_{BO}$ (J_{SC}=6.06 mA cm^{-2}, calc. J_{SC}=8.58 mA cm^{-2}) and P2FDTBT$_{BO}$ (J_{SC}=9.91 mA cm^{-2}, calc. J_{SC}=15.1 mA cm^{-2}) PSCs. The spectral shape of the EQE data is similar to UV-Vis absorption spectra, where P2FDTBT$_{BO}$ PSCs show the broadest spectrum up to ~760 nm (**Figure 4.5b**). Similar phenomena were also observed in polymer:ITIC PSCs (**Figure 4.6**). In the case of PDTBT$_{BO}$:ITIC PSCs, there was

negligible discrepancy in the measured and calc. J_{SC} values (10.4 vs. 10.4 mA cm^{-2}). However, mis-matched J_{SC} values were observed in PTTBT$_{BO}$:ITIC (J_{SC}=3.94 mA cm^{-2}, calc. J_{SC}=4.25 mA cm^{-2}) and P2FDTBT$_{BO}$:ITIC PSCs (J_{SC}=7.04 mA cm^{-2}, calc. J_{SC}=10.7 mA cm^{-2}). This unusual phenomenon motivated us to investigate the origins of the discrepancy. We suspected the higher calc. J_{SC} might be related to the low light intensity used for EQE measurement. In this case, PTTBT$_{BO}$ and P2FDTBT$_{BO}$ may show very different photovoltaic characteristics depending on the illuminated light intensity.
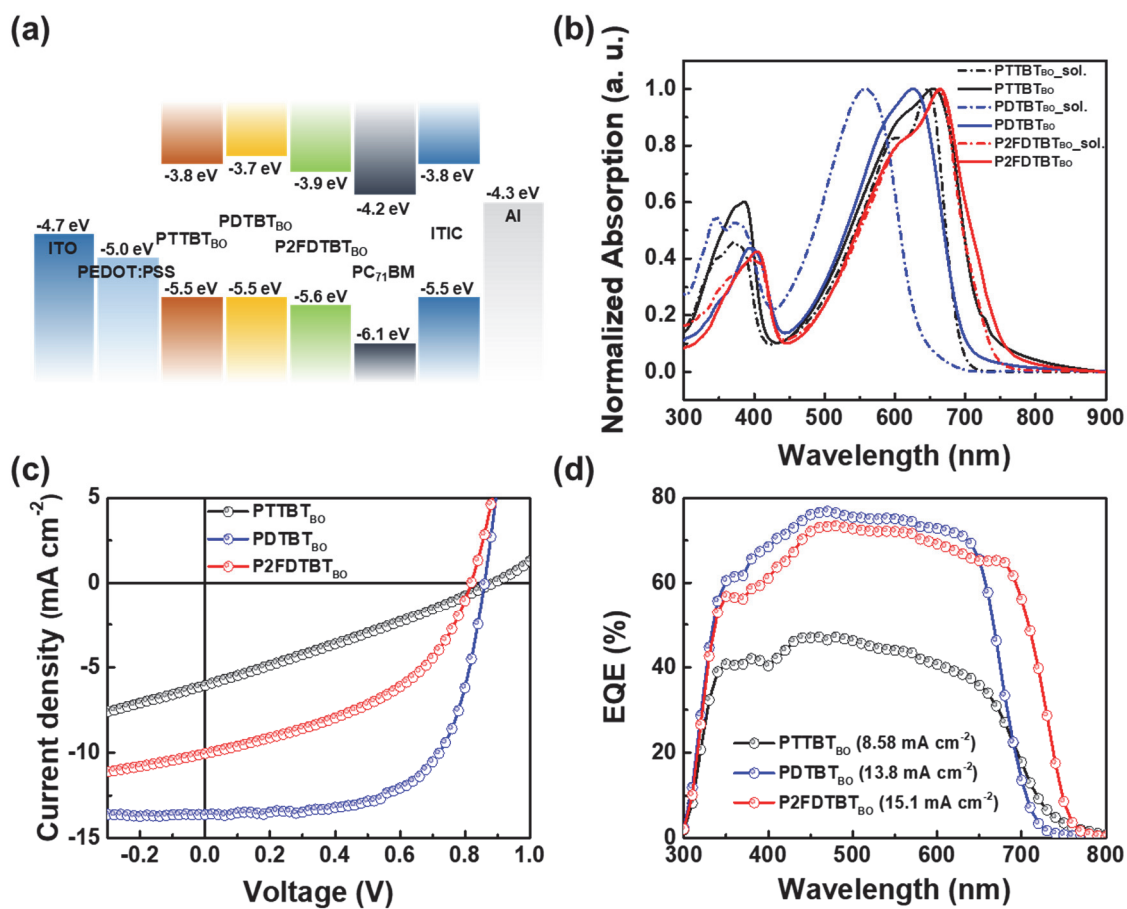
Figure 4. 5. (a) Energy band diagram. (b) Normalized UV-vis absorption spectra of three polymers in chloroform (dash-dotted) and in thin film (solid) (c) *J-V* characteristics and (d) EQE spectra of polymer:PC$_{71}$BM devices measured under AM 1.5G condition (Calculated J_{SC} values are included in parenthesis in the legend).

Table 4. 2. Photovoltaic parameters of polymer:$PC_{71}BM$ PSCs under various light intensities.

Polymer	Solvent additive (2 vol%)	I_{light} [mW cm^{-2}]	J_{SC}[a] [mA cm^{-2}]	V_{OC}[a] [V]	FF[a]	PCE[a] [%]
PTTBT$_{BO}$	None	100	4.40 (4.12±0.19)	0.88 (0.87±0.01)	0.26 (0.26±0.00)	0.99 (0.92±0.05)
	ODT	100	6.06 (5.77±0.21)	0.89 (0.87±0.01)	0.28 (0.28±0.00)	1.50 (1.42±0.04)
		50	3.68 (3.54±0.13)	0.85 (0.86±0.01)	0.29 (0.29±0.00)	1.83 (1.77±0.05)
		25	2.22 (2.11±0.09)	0.85 (0.85±0.01)	0.30 (0.31±0.00)	2.29 (2.19±0.07)
		10	0.88 (0.84±0.04)	0.84 (0.83±0.01)	0.35 (0.35±0.00)	2.56 (2.44±0.10)
		2.5	0.28 (0.27±0.01)	0.82 (0.81±0.01)	0.40 (0.40±0.00)	3.57 (3.39±0.14)
PDTBT$_{BO}$	None	100	5.54 (5.00±0.44)	0.95 (0.94±0.01)	0.34 (0.33±0.01)	1.80 (1.54±0.20)
	ODT	100	13.6 (12.7±0.57)	0.86 (0.85±0.01)	0.64 (0.66±0.01)	7.52 (7.12±0.24)
		50	7.15 (6.56±0.35)	0.83 (0.82±0.00)	0.68 (0.71±0.02)	8.02 (7.62±0.24)
		25	3.55 (3.49±0.06)	0.81 (0.81±0.00)	0.74 (0.74±0.00)	8.44 (8.28±0.15)
		10	1.39 (1.33±0.06)	0.79 (0.79±0.00)	0.76 (0.76±0.00)	8.33 (7.93±0.40)
		2.5	0.36 (0.37±0.01)	0.75 (0.74±0.01)	0.77 (0.76±0.00)	9.60 (8.72±0.54)
P2FDTBT$_{BO}$	None	100	7.88 (7.26±0.38)	0.82 (0.82±0.01)	0.46 (0.43±0.02)	2.97 (2.57±0.19)
	ODT	100	9.91 (9.43±0.37)	0.86 (0.84±0.01)	0.44 (0.43±0.01)	3.69 (3.42±0.20)
		50	6.10 (5.79±0.25)	0.83 (0.83±0.00)	0.43 (0.43±0.01)	4.40 (4.15±0.21)
		25	3.79 (3.57±0.18)	0.82 (0.82±0.00)	0.44 (0.44±0.00)	5.47 (5.18±0.25)
		10	1.43 (1.35±0.06)	0.81 (0.81±0.00)	0.52 (0.53±0.01)	5.98 (5.70±0.23)
		2.5	0.43 (0.41±0.02)	0.79 (0.78±0.01)	0.62 (0.62±0.01)	8.33 (7.88±0.40)

[a]Average values obtained from 15 devices are stated in parenthesis.
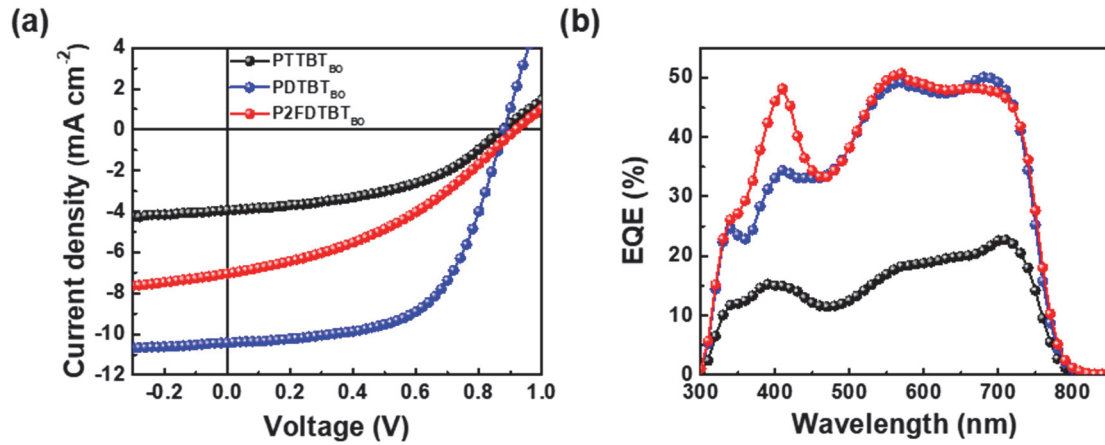
Figure 4. 6. (a) *J-V* characteristics and (b) EQE spectra for polymer:ITIC PSCs.

Table 4. 3. Photovoltaic parameters of polymer:ITIC BHJ PSCs under various light intensities

BHJ	Light intensity [mW cm^{-2}]	J_{SC} [mA cm^{-2}]	V_{OC} [V]	FF	PCE [%]
	100	3.94 (4.25)[a]	0.87	0.46	1.57
	50	2.10	0.88	0.50	1.82
PTTBT$_{BO}$: ITIC	25	1.22	0.88	0.53	2.24
	10	0.43	0.86	0.57	2.13
	2.5	0.13	0.84	0.60	2.67
	100	10.42 (10.4)[a]	0.88	0.59	5.41
	50	5.27	0.88	0.63	5.79
PDTBT$_{BO}$: ITIC	25	2.86	0.87	0.65	6.48
	10	1.02	0.85	0.68	5.84
	2.5	0.30	0.82	0.67	6.48
	100	7.04 (10.7)[a]	0.92	0.38	2.46
	50	3.98	0.92	0.42	3.08
P2FDTBT$_{BO}$: ITIC	25	2.39	0.92	0.46	4.01
	10	0.93	0.91	0.51	4.34
	2.5	0.30	0.89	0.56	5.85

[a]Calculated J_{SC} from EQE spectra.

To systematically analyze the unusual behavior of $PTTBT_{BO}$ and $P2FDTBT_{BO}$ polymers, photovoltaic characteristics of BHJ devices (with $PC_{71}BM$ and ITIC) were investigated in detail under various light intensity (I_{light}) as shown in **Figure 4.7** and **4.8**, respectively. When the I_{light} decreased from 100 to 2.5 mW cm^{-2}, a small improvement of PCE (by 28%) was observed in $PDTBT_{BO}$:$PC_{71}BM$ PSCs (7.52% to 9.60%). The weak light intensity dependence for $PDTBT_{BO}$:$PC_{71}BM$ must be related to little electron-hole recombination even under 1 sun illumination during charge extraction, due to small R_s and high R_{sh}. However, a dramatic increase in device performance was observed by 2.4 times (PCE: 1.50% to 3.57%) and by 2.3 times (PCE: 3.69% to 8.33%) for $PTTBT_{BO}$ and $P2FDTBT_{BO}$ PSCs, respectively, as I_{light} decreased from 100 to 2.5 mW cm^{-2}. One noticeable thing is that the J_{SC} for $P2FDTBT_{BO}$ PSC becomes higher than that of $PDTBT_{BO}$ PSCs below $I_{light} = \sim25$ mW cm^{-2} (**Figure 4.7a**), which is well-matched with EQE results in **Figure 4.5d**. Similar phenomena were also observed in polymer:ITIC PSCs, showing significantly improved photovoltaic performance for $PTTBT_{BO}$:ITIC and $P2FDTBT_{BO}$: ITIC under weak light illumination, as summarized in **Table 4.3**. We also compared photovoltaic properties vs. I_{light} using other reference photovoltaic polymers, including poly[N-9′-heptadecanyl-2,7-carbazole-alt-5,5-(4′,7′-di-2-thienyl-2′,1′,3′-benzothiadiazole)] (PCDTBT), poly(3-hexylthiophene) (P3HT) and poly[4,8-bis(5-(2-ethylhexyl)thiophen-2-yl)benzo[1,2-b:4,5-b′]dithiophene-co-3-flurothieno[3,4-b]thiophene-2-carboxylate] (PTB7-Th) as shown in **Figure 4.9**. PCDTBT, P3HT and PTB7-Th PSCs showed similar tendencies with $PDTBT_{BO}$ PSCs including minor improvements in PCE under dim light illumination. To our knowledge, the dramatic improvement of PCEs in $PTTBT_{BO}$ and $P2FDTBT_{BO}$ PSCs is unusual and merits a more detailed investigation.
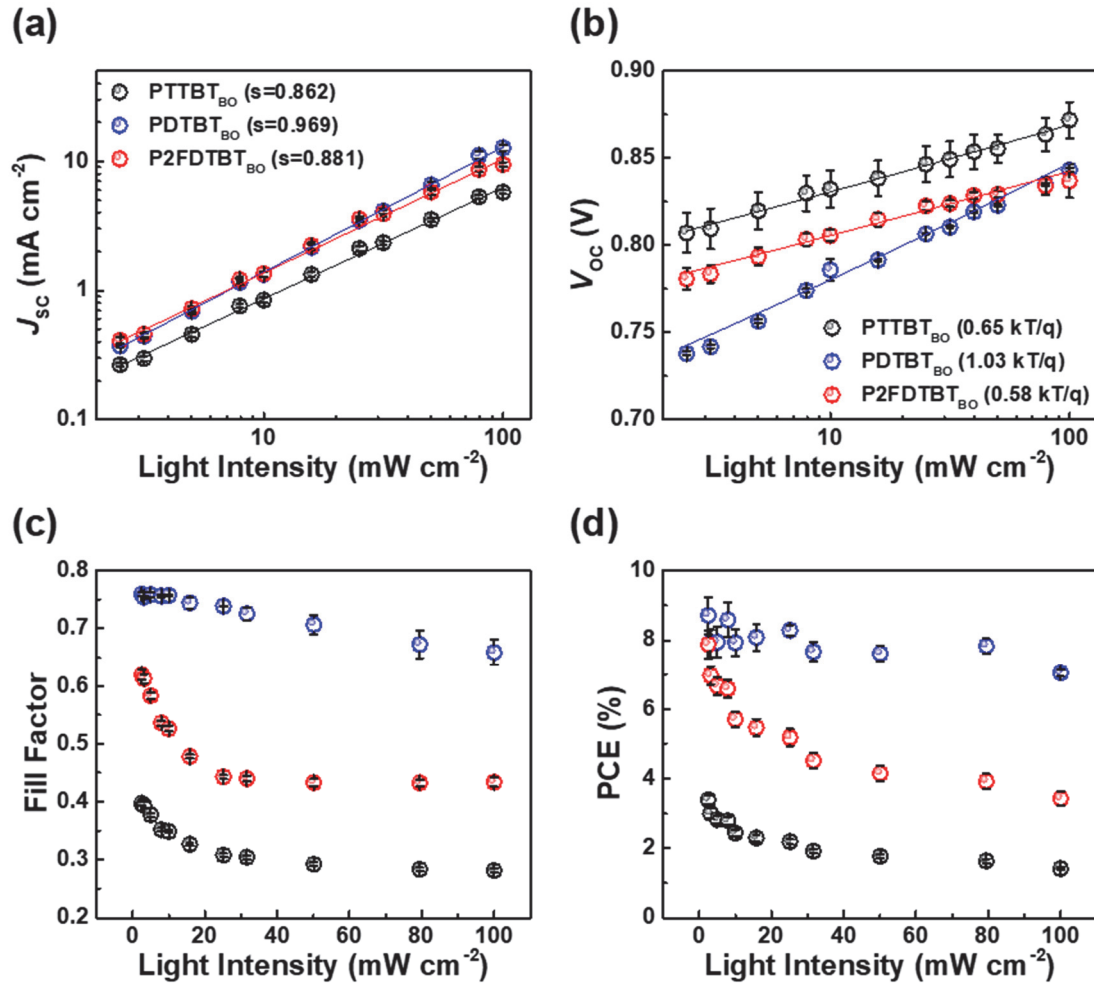
Figure 4. 7. Light intensity dependent photovoltaic parameters: (a) J_{SC}, (b) V_{OC}, (c) FF and (d) PCE for polymer:$PC_{71}BM$ devices.
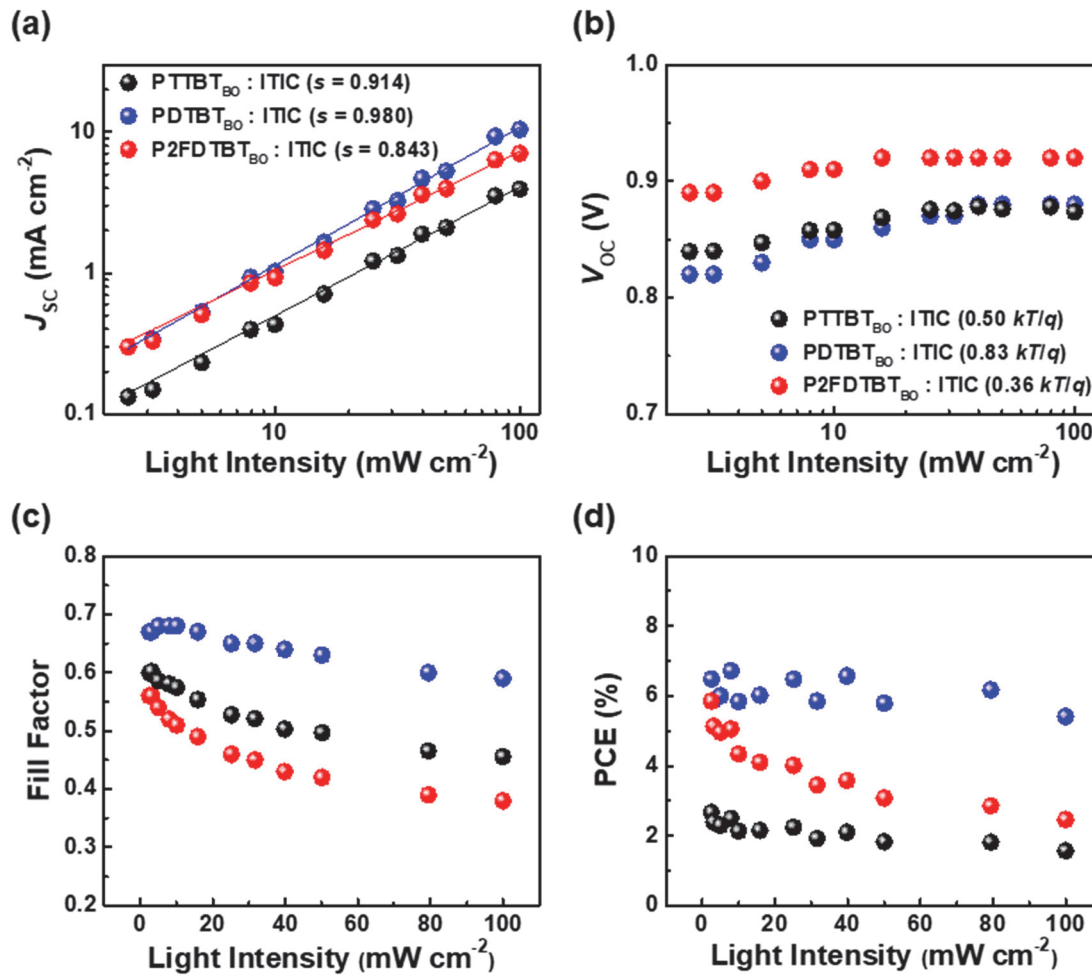
Figure 4. 8. Light intensity dependent photovoltaic parameters; (a) J_{SC}, (b) V_{OC}, (c) *FF* and (d) PCE for polymer:ITIC PSCs.
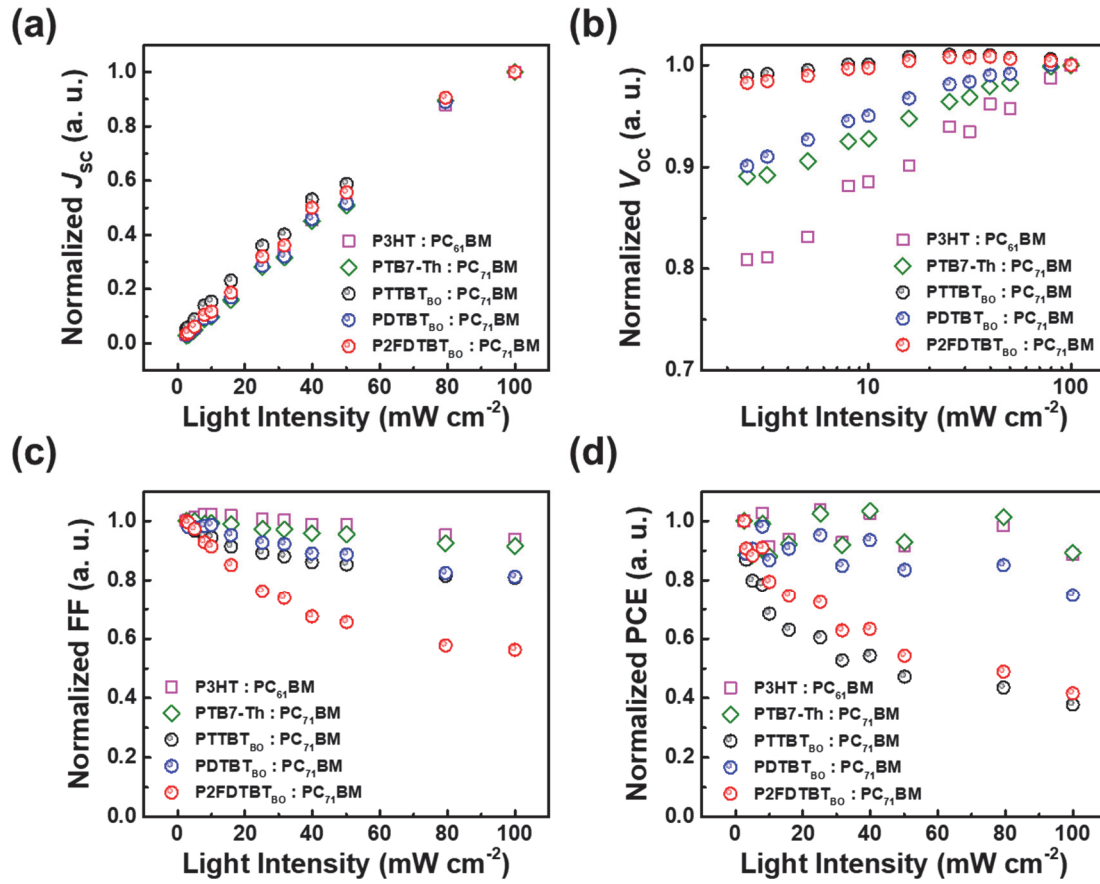
Figure 4. 9. Light intensity dependence of normalized photovoltaic parameters (a) J_{SC}, (b) V_{OC}, (c) FF and (d) PCE for various polymer:PC$_{71}$BM PSCs.

In the case of polymer:PC$_{71}$BM PSCs, the V_{OC} decreases from 0.86 to 0.75 V for PDTBT$_{BO}$, however the V_{OC} decrements for PTTBT$_{BO}$ (0.89 to 0.82 V) and P2FDTBT$_{BO}$ (0.86 to 0.79 V) were relatively small with decreasing the light intensity. This can be understood in terms of large R_s in PTTBT$_{BO}$ and P2FDTBT$_{BO}$ devices and the different R_s–induced voltage drop under 1 sun and dim light illumination, which will be discussed in the following section. The FF values increase substantially for all PSCs, probably due to decreased charge recombination under weak I_{light}. From the light intensity dependent J_{SC} and V_{OC} (J_{SC} vs. I_{light} and V_{OC} vs. I_{light}) measurements, we can obtain information of charge recombination processes in the devices. Generally J_{SC} shows a power law dependence on I_{light}, following the relationship of $J_{SC} \propto I_{light}{}^s$ (where s is an exponential constant). When s is close to unity, the BHJ system has weak bimolecular recombination.[94, 116] As shown in **Figure 4.7a** and **4.8a**, s values were measured to be 0.969 and 0.980 for PDTBT$_{BO}$:PC$_{71}$BM and PDTBT$_{BO}$:ITIC PSCs, respectively. However, PTTBT$_{BO}$ BHJ systems show s values of 0.862 and 0.914 for PTTBT$_{BO}$:PC$_{71}$BM and PTTBT$_{BO}$:ITIC PSCs, respectively. With regard to the P2FDTBT$_{BO}$ BHJ systems, s values were

measured to be 0.881 and 0.843 for P2FDTBT$_{BO}$:PC$_{71}$BM and P2FDTBT$_{BO}$:ITIC PSCs, respectively. Since PTTBT$_{BO}$ and P2FDTBT$_{BO}$ BHJ systems exhibited much smaller s values compared to those of PDTBT$_{BO}$ PSCs, these systems are interpreted to suffer from significant bimolecular recombination losses, leading to worse device performance.

If a given BHJ system has only bimolecular recombination losses without any trap-assisted or surface recombination, the V_{OC} follows the equation (4-1),

$$V_{OC} = \frac{E_{gap}}{q} - \frac{kT}{q}\ln\left[\frac{(1-P_D)\gamma N_C^2}{P_D G}\right] \qquad (4\text{-}1)$$

where E_{gap} is the energy difference between the HOMO$_{donor}$ and LUMO$_{acceptor}$, q is the elementary charge, k is the Boltzmann constant, T is temperature in Kelvin, P_D is the dissociation probability of the electron (e)-hole (h) pairs, γ is the Langevin recombination constant, N_C is the effective density of states, and G is the generation rate of bound e-h pairs. From equation (1), since G is the only parameter directly proportional to I_{light}, a slope of V_{OC} vs. $\ln(I_{light})$ gives information about whether additional Shockley-Read-Hall (SRH or trap-assisted) recombination is involved (slope $> kT/q$) or not.[94] As shown in **Figure 4.7b**, the slope of PDTBT$_{BO}$:PC$_{71}$BM is 1.03 kT/q, suggesting negligible involvement of trap-assisted recombination. The other BHJ systems, however, have slope values less than kT/q, which may be mainly attributed to surface recombination.[97] The slope for PTTBT$_{BO}$ and P2FDTBT$_{BO}$:PC$_{71}$BM PSCs was measured to be 0.65 kT/q and 0.58 kT/q, respectively, indicating these BHJs have higher surface recombination rates than drift of charge carriers.[96] Both PTTBT$_{BO}$ and P2FDTBT$_{BO}$ BHJs are interpreted to have higher surface charge recombination due to large R_s, showing significant R_s-induced voltage drop under 1 sun illumination. Under dim light, the photo-generated current becomes small and the R_s-induced voltage drop is also decreased, leading to small decrement of V_{OC} for PTTBT$_{BO}$ and P2FDTBT$_{BO}$ as decreasing I_{light}, inducing a smaller slope in the V_{OC} vs. I_{light} plot. Similarly, PTTBT$_{BO}$:ITIC and P2FDTBT$_{BO}$:ITIC PSCs also showed slopes smaller than 1. These were found to be 0.50 kT/q and 0.36 kT/q, respectively.

To investigate the role of R_{sh} and R_s in determining photovoltaic characteristics under different light intensity, we measured J-V characteristics in the dark as shown in **Figure 4.10a**. Detailed electrical parameters are summarized in **Table 4.4**. Generally, high R_{sh} and low R_s are essential factors to achieve high-performance PSCs under 1 sun condition, because both resistances are closely related to J_{SC} and FF. In contrast, under low I_{light} conditions, R_s is less significant, because the generated current is too small to cause noticeable R_s losses.[105] Instead, high R_{sh} becomes more important to avoid leakage currents, since low photo-generated current is sharply influenced by R_{sh}.[108] PDTBT$_{BO}$:PC$_{71}$BM PSCs

showed the lowest R_s of 5.26 Ω cm^2 and moderate R_{sh} of 581.4 kΩ cm^2, which leads to good device performance without significant charge recombination under both 1 sun and weak I_{light} irradiations. Interestingly, P2FDTBT$_{BO}$ PSCs showed poor device performance (3.46% PCE with large R_s of 9.42 Ω cm^2) under 1 sun illumination, but showed a remarkable enhancement of PCE over 8% under weak I_{light} irradiation (with the highest R_{sh} of 1326 kΩ cm^2). In the case of PTTBT$_{BO}$:PC$_{71}$BM, high R_s (50.9 Ω cm^2) and low R_{sh} (19.17 kΩ cm^2) were observed, which led to poor device performance under both 1 sun and weak I_{light} irradiation. For both PTTBT$_{BO}$:PC$_{71}$BM and P2FDTBT$_{BO}$:PC$_{71}$BM, the high R_s led to significant charge recombination under 1 sun, but the R_s-induced voltage drop was not serious under dim light due to the small photocurrent, resulting in little decrease in V_{OC} with decreasing the illumination I_{light}. Similar tendencies were observed in polymer:ITIC PSCs as shown in **Figure 4.10b** and **Table 4.4**. The high R_s values in PTTBT$_{BO}$ and P2FDTBT$_{BO}$ PSCs may account for large surface recombination as previously discussed.
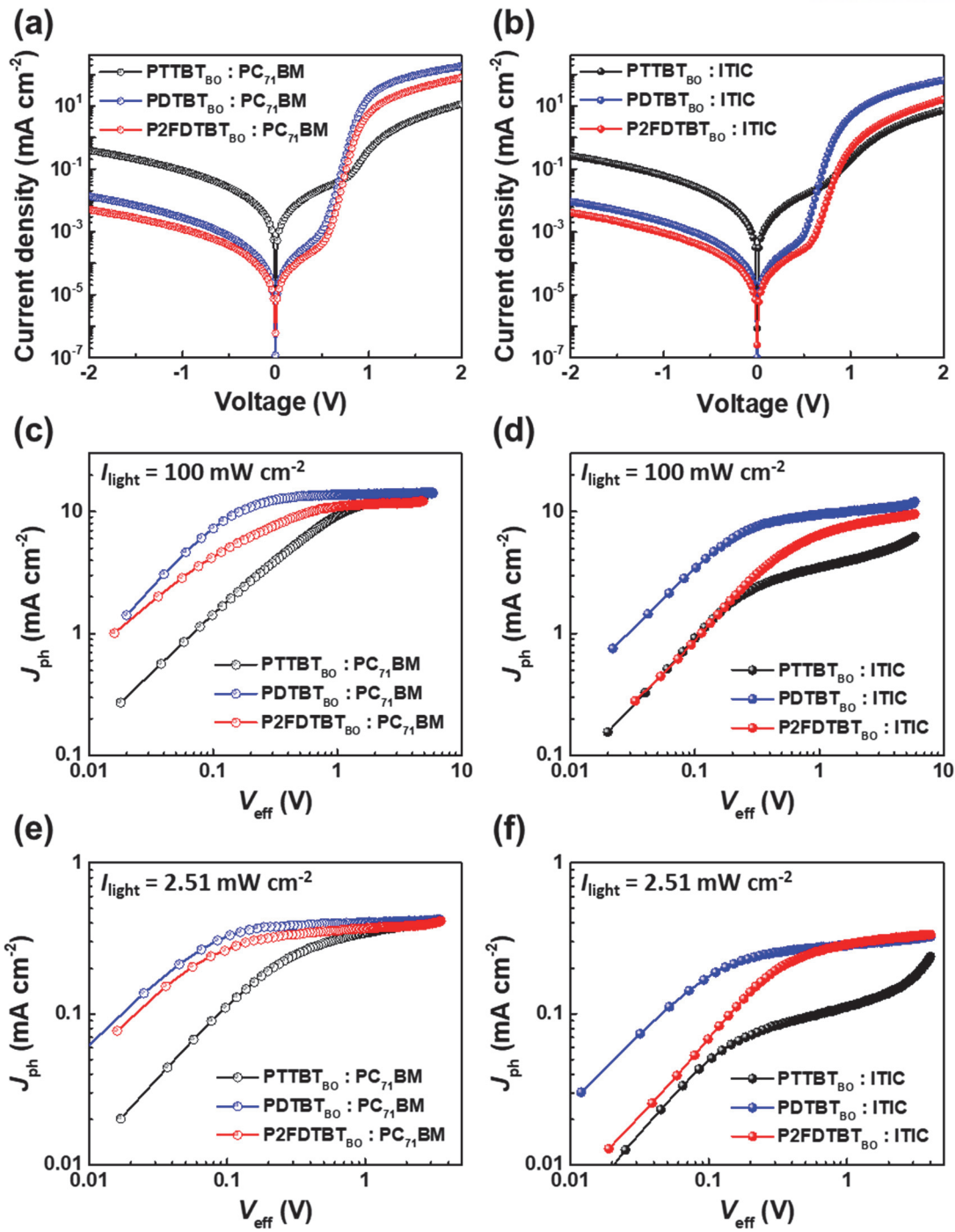
Figure 4. 10. J-V characteristics in the dark for (a) polymer:$PC_{71}BM$ and (b) polymer:ITIC PSCs. Photocurrent density (J_{ph}) – effective voltage ($V_{eff} = V_0 - V$) characteristics measured under (c, d) 100 mW cm^{-2} and (e, f) 2.51 mW cm^{-2} light intensity illumination for polymer:$PC_{71}BM$ and polymer:ITIC PSCs, respectively.

To investigate charge generation and extraction characteristics, further analysis was carried out by measuring the photocurrent density (J_{ph}) as a function of effective voltage (V_{eff}) where $J_{ph} = J_L - J_D$ (J_L and J_D is current densities under illumination and in the dark, respectively) and $V_{eff} = V_0 - V$ (V_0 is the voltage at $J_{ph} = 0$ and V is applied voltage). J_{ph}-V_{eff} characteristics measured under AM 1.5G irradiation (100 mW cm^{-2}) are plotted in **Figure 4.10c**. The highest J_{ph} with quick saturation at $V_{eff} = \sim 0.45$ V was observed in both PDTBT$_{BO}$:PC$_{71}$BM and PDTBT$_{BO}$:ITIC PSCs (**Figure 4.10d**), while PTTBT$_{BO}$ PSCs showed unclear J_{ph} saturation and P2FDTBT$_{BO}$ PSCs exhibited J_{ph} saturation under high V_{eff}. The field-independent saturation of J_{ph} in PDTBT$_{BO}$ BHJs suggests negligible trapped charges and efficient charge collection. We also measured J_{ph}-V_{eff} characteristics under low I_{light} (2.51 mW cm^{-2}), and the results are shown in **Figure 4.10e** and **4.10f**. PDTBT$_{BO}$ and P2FDTBT$_{BO}$ PSCs showed clear saturation of J_{ph} at low V_{eff} of ~ 0.25 V and ~ 0.3 V, respectively. J_{ph} saturation was not clear for PTTBT$_{BO}$:PC$_{71}$BM, due to high R_s and low R_{sh}. Under low I_{light}, it appears that better charge transport and extraction with less trapping occurs compared to under 1 sun illumination, which is consistent with the observed device performance.
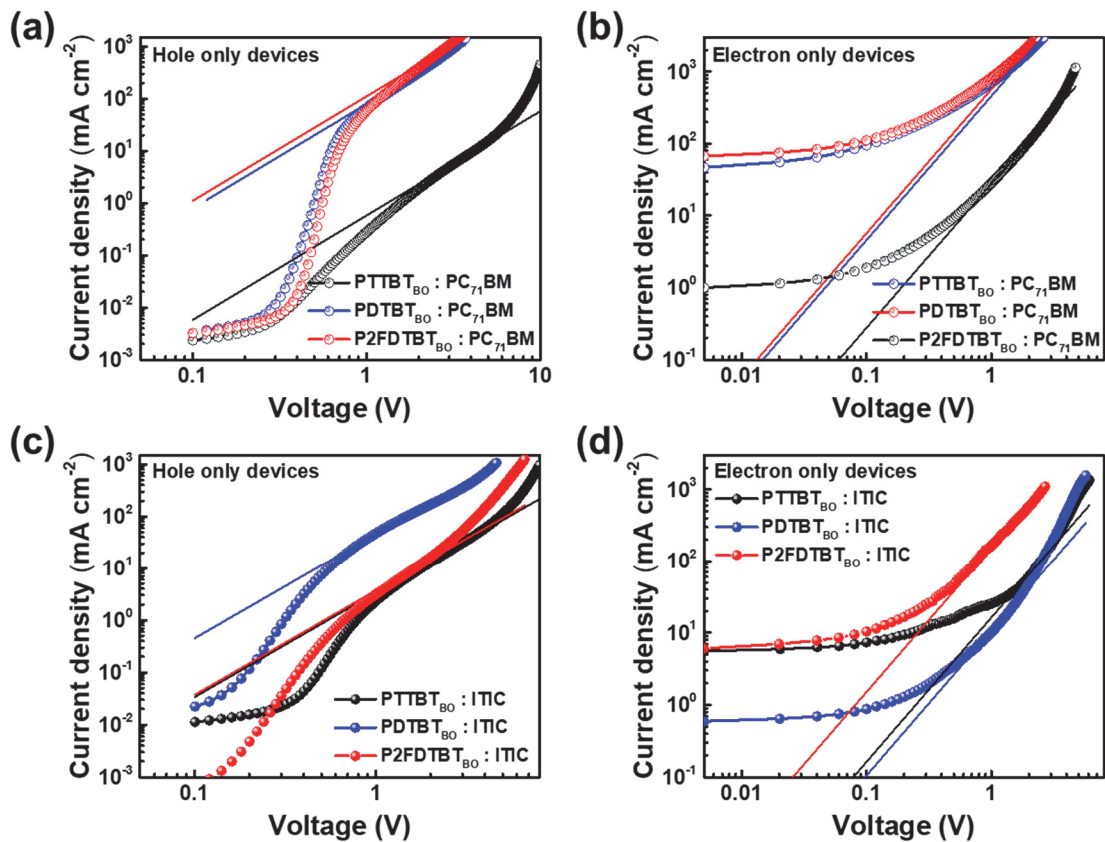
Figure 4. 11. *J-V* characteristics of (a, c) hole-only and (b, d) electron-only devices.

Single carrier diodes were prepared in order to measure the hole and electron mobilities for carrier transport in the vertical direction by the space-charge-limited currents (SCLC) method. Furthermore, trap densities (n_t) were obtained by fitting trap-filling limit (TFL) regime.[117-118] Detailed parameters are summarized in **Table 4.4** and **Figure 4.11**. For PDTBT$_{BO}$:PC$_{71}$BM BHJs, the highest hole mobilities (μ_h, 7.27×10^{-4} cm^2 V^{-1} s^{-1}) were observed. Balanced hole and electron (μ_e, 5.25×10^{-4} cm^2 V^{-1} s^{-1}) mobilities led to efficient charge transport and extraction. The lowest μ_h (6.52×10^{-6} cm^2 V^{-1} s^{-1}) and μ_e (1.23×10^{-4} cm^2 V^{-1} s^{-1}) values were observed for PTTBT$_{BO}$:PC$_{71}$BM BHJs, indicating poor charge transport properties. Although P2FDTBT$_{BO}$:PC$_{71}$BM BHJs showed similar mobilities in the range of $\sim10^{-4}$ cm^2 V^{-1} s^{-1}, an order of higher n_t of $\sim10^{16}$ cm^{-3} was observed, compared to PDTBT$_{BO}$ BHJs ($\sim10^{15}$ cm^{-3}). This higher n_t must be related to high R_s and charge recombination, leading to an efficiency drop under 1 sun irradiation. Furthermore, the high n_t is related to density of defects in the active layer, especially in donor phase. In P2FDTBT$_{BO}$ PSCs, interestingly V_{OC} was lower (0.86 V) than the other polymers, despite the lowest HOMO level (-5.57 eV) of P2FDTBT$_{BO}$. We attribute this lower V_{OC} to the high density of defects which can increase hole Fermi level from HOMO level of donor.[22, 119]

Table 4. 4. Summary of charge carrier mobilities and trap densities derived from single carrier devices of polymer:ITIC blend films.

Polymer	μ_h [cm^2 V^{-1} s^{-1}]	μ_e [cm^2 V^{-1} s^{-1}]	μ_h/μ_e	n_t [cm^{-3}]	R_{sh} [kΩ cm^2]	R_s [Ω cm^2]
PTTBT$_{BO}$	5.82×10^{-6}	6.81×10^{-6}	0.85	2.03×10^{16}	30.41	80.69
PDTBT$_{BO}$	1.38×10^{-5}	1.51×10^{-6}	9.14	3.08×10^{16}	819.7	11.97
P2FDTBT$_{BO}$	7.98×10^{-7}	4.04×10^{-6}	0.20	3.17×10^{16}	1660	34.54
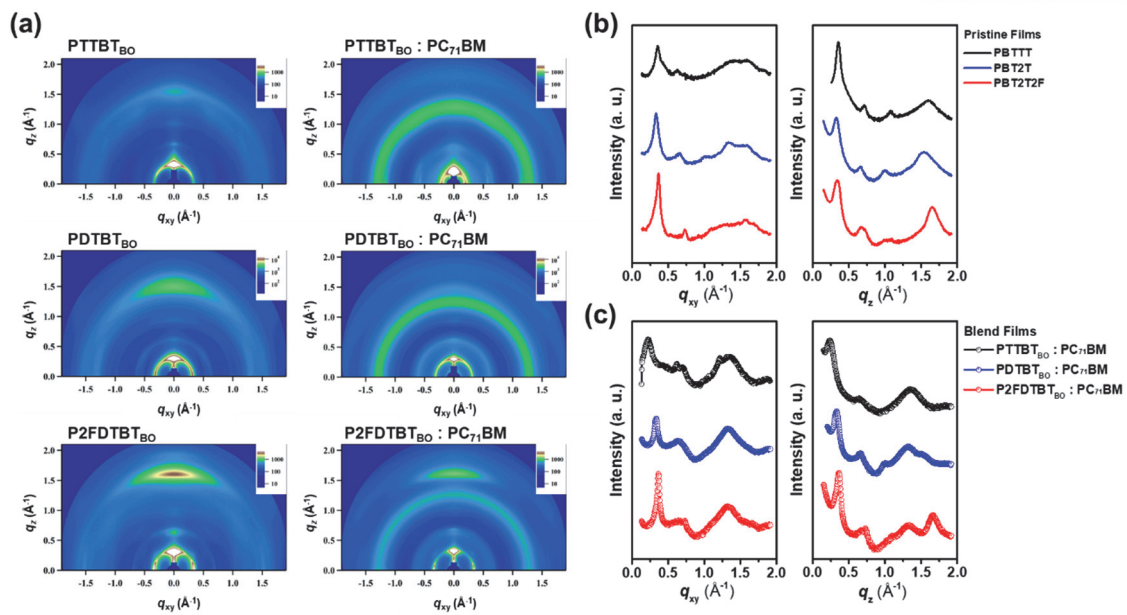
Figure 4. 12. (a) 2D GIWAXS images for pristine polymers and polymer:PC$_{71}$BM blend films. Line-cut profiles for (b) pristine polymers and (c) polymer:PC$_{71}$BM blend films. Blend films were prepared with ODT as solvent additive.
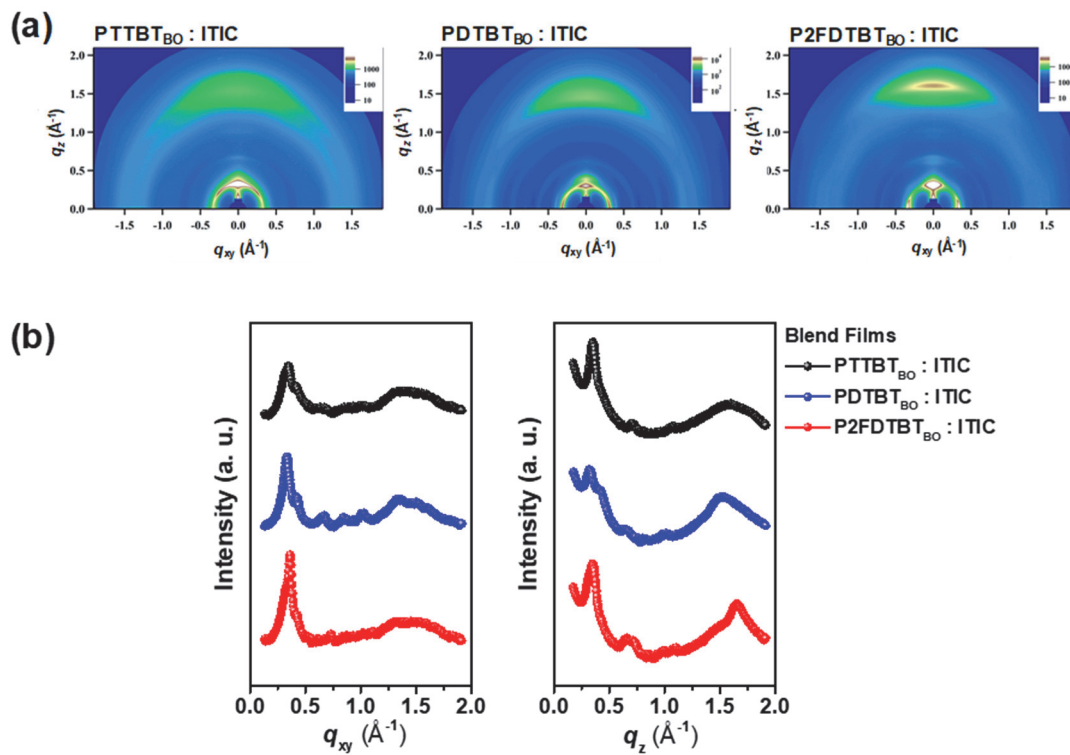
Figure 4. 13. (a) 2D GI-WAXS images and (b) line-cut profiles for polymer:ITIC blend films.

Table 4. 5. Packing parameters of pristine and blend BHJ films.

Thin film	Material	GI-WAXS parameters							
		Lamella spacing (q_{xy} direction)		π-π stacing (q_{xy} direction)		Lamella spacing (q_z direction)		π-π stacing (q_z direction)	
		q (Å^{-1})	d (Å)	q (Å^{-1})	d (Å)	q (Å^{-1})	d (Å)	q (Å^{-1})	d (Å)
Pristine	PTTBT$_{BO}$	0.3567	17.6148	-	-	0.3541	17.7440	1.5962	3.9363
	PDTBT$_{BO}$	0.3310	18.9824	-	-	0.3265	19.2441	1.5384	4.0842
	P2FDTBT$_{BO}$	0.3666	17.1390	-	-	0.3364	18.6777	1.6569	3.7921
Blend (w/ PC$_{71}$BM)	PTTBT$_{BO}$	0.2205	28.4952	-	-	0.2276	27.6063	-	-
	PDTBT$_{BO}$	0.3310	18.9824	-	-	0.3265	19.2441	-	-
	P2FDTBT$_{BO}$	0.3647	17.2284	-	-	0.3620	17.3569	1.6517	3.8041
Blend (w/ ITIC)	PTTBT$_{BO}$	0.3448	18.2227	-	-	0.3541	17.7440	-	-
	PDTBT$_{BO}$	0.3350	18.7558	-	-	0.3206	19.5982	1.5119	4.1558
	P2FDTBT$_{BO}$	0.3626	17.3281	-	-	0.3502	17.9417	1.6552	3.7960

Detailed molecular ordering and packing structures were investigated by two-dimensional GIWAXS using pristine and blend films. GIWAXS images and line-cut profiles are shown in **Figure 4.12**. All three polymers showed dominant face-on π-π stacking structures in pristine films, however, the (010) π-π stacking peak in the z direction almost disappeared in the blend film for PTTBT$_{BO}$:PC$_{71}$BM, which may be one reason for inefficient charge transport and poor device performance of PTTBT$_{BO}$:PC$_{71}$BM. P2FDTBT$_{BO}$ showed the tightest face-on π-π stacking (d-spacing of ~3.8 Å) in both pristine and blend films with PC$_{71}$BM. Similar tendencies were also observed in the polymer:ITIC blend films (**Figure 4.13**). Strong intra- and intermolecular noncovalent coulombic interactions in P2FDTBT$_{BO}$ (via $S^{\delta+}\cdots O^{\delta-}$ or $S^{\delta+}\cdots F^{\delta-}$) may direct the compact face-on π-π stacking, which increases R_{sh} compared to the other two polymers (PTTBT$_{BO}$ and PDTBT$_{BO}$), resulting in negligible leakage current (see the smallest dark current under reverse bias for P2FDTBT$_{BO}$ due to R_{sh} in **Figure 4.10a** and **4.10b**) and significant enhancement of PCE under dim light.[120-121] We also measured atomic force microscopy (AFM) topographical images for polymer:PC$_{71}$BM blend films (**Figure 4.14**). PTTBT$_{BO}$:PC$_{71}$BM film shows clearly larger domains in the surface with fibrillar structures which may disturb charge transport in the grain boundaries. This supports the poor photovoltaic performance of PTTBT$_{BO}$:PC$_{71}$BM under 1 sun and dim light illuminations. For PDTBT$_{BO}$ and P2FDTBT$_{BO}$ blend films, similar film morphologies and surface roughness (RMS roughness of ~ 1.36 nm) were observed.
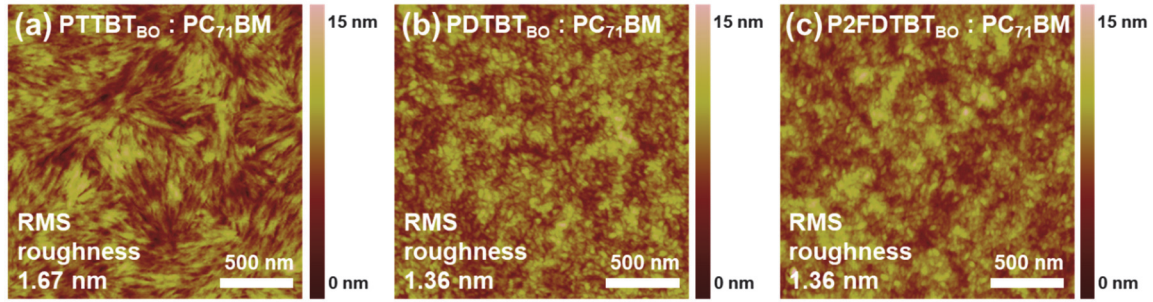
Figure 4. 14. AFM topographical images for (a) PTTBT$_{BO}$:PC$_{71}$BM, (b) PDTBT$_{BO}$:PC$_{71}$BM and (c) P2FDTBT$_{BO}$:PC$_{71}$BM blend films prepared with ODT.
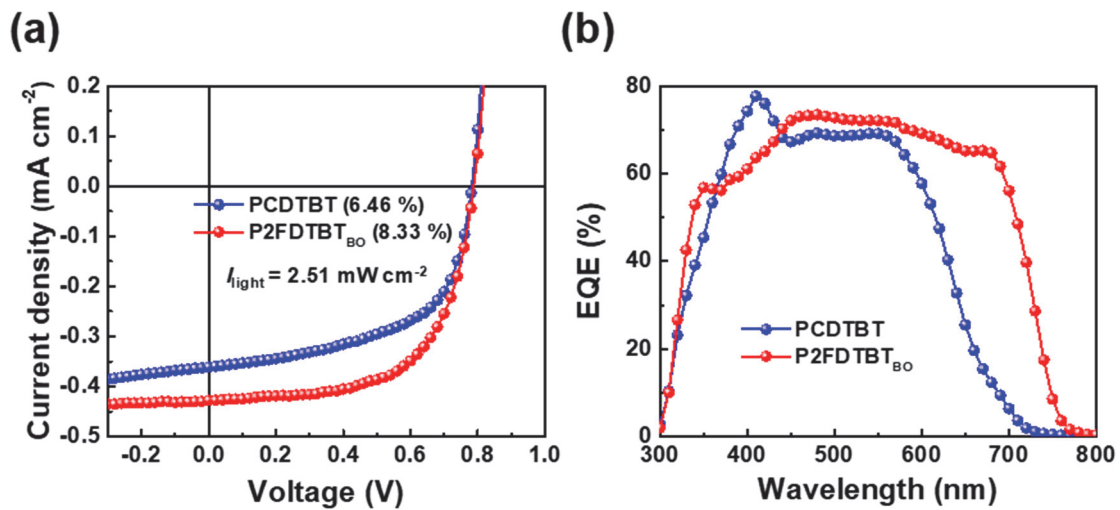
Figure 4. 15. (a) *J-V* characteristics measured under I_{light} = 2.51 mW cm^{-2} and (b) EQE spectra for PCDTBT:PC$_{71}$BM and P2FDTBT$_{BO}$:PC$_{71}$BM PSCs.

In addition, we compared the photovoltaic properties of PCDTBT:PC$_{71}$BM and P2FDTBT$_{BO}$:PC$_{71}$BM PSCs under I_{light} = 2.51 mW cm^{-2} (**Figure 4.15**). Contrary to the reported nice photovoltaic properties under a fluorescent lamp,[12] PCDTBT PSCs showed a similar PCE with that (6%) under 1 sun illumination. As shown in **Figure 4.15a**, PCDTBT shows the poorer performance (PCE = 6.46%) than P2FDTBT$_{BO}$ (PCE = 8.33%). The PCDTBT BHJ film was reported to form amorphous morphology and P2FDTBT$_{BO}$ blend shows semi-crystalline morphology with compact face-on

interchain stacking. The different film morphology of both blends is expected to influence the R_{sh} significantly. Compared to reported PCDTBT PSCs in the same device structures, P2FDTBT$_{BO}$ PSCs showed much lower leakage current (~10^{-2} order of magnitude) in the R_{sh} region, suggesting the much higher R_{sh} of P2FDTBT$_{BO}$ PSCs.[122] At a present stage, although we do not understand clearly how to design ideal indoor photovoltaic molecules to increase R_{sh}, the crystalline morphology must be one main parameter to be considered.

4.4 Conclusion

We designed three semi-crystalline polymers (PTTBT$_{BO}$, PDTBT$_{BO}$, and P2FDTBT$_{BO}$) containing dialkoxybenzothiadiazole, and investigated their photovoltaic characteristics under various illumination I_{light}. PTTBT$_{BO}$ and P2FDTBT$_{BO}$ PSCs showed interesting behavior with a significant discrepancy between measured J_{SC} and calc. J_{SC}, and the discrepancy originates from the low light intensity used for EQE measurements. As incident light intensity decreased to 1/40 of standard illumination intensity, the PCEs significantly increased by 2.4 times (PCE: 1.50% to 3.75%) and 2.3 times (PCE: 3.69% to 8.33%) in PTTBT$_{BO}$ and P2FDTBT$_{BO}$:PC$_{71}$BM PSCs, respectively, while a 28% (PCE: 7.52% to 9.60%) increase was observed in PDTBT$_{BO}$:PC$_{71}$BM PSCs. In the case of PDTBT$_{BO}$ devices, the lowest R_s (5.26 Ω cm^2) and moderate R_{sh} (581.4 kΩ cm^2) led to the best photovoltaic performance among the three polymers under both standard and dim light. On the other hand, both PTTBT$_{BO}$ and P2FDTBT$_{BO}$ PSCs suffered from high R_s (50.9 and 9.42 Ω cm^2, respectively) and e-h charge recombination, resulting poor device performance under standard illumination. The high R_s and low R_{sh} (19 kΩ cm^2) of PTTBT$_{BO}$ PSCs led to poor device performance even under dim light. With P2FDTBT$_{BO}$ PSCs, the highest R_{sh} of over 1000 kΩ cm^2 was measured due to tight face-on intermolecular packing, leading to remarkable enhancement of PCE under dim light with minimal leakage current through a high R_{sh}. Contrary to PDTBT$_{BO}$:PC$_{71}$BM, the smaller decrements of V_{OC} were observed for PTTBT$_{BO}$ (from 0.89 to 0.82 V) and P2FDTBT$_{BO}$ (from 0.86 to 0.79 V) devices with decreasing light intensity. These small decrements of V_{OC} originates from lowering the R_s–induced voltage drop due to small photo-generated current under dim light, emphasizing that high R_{sh} is essential (whereas R_s is less critical) for indoor applications. This work reveals that although the photovoltaic devices may show modest device performance (with high R_s) under 1 sun illumination, they can nonetheless be useful for indoor and weak light applications if R_{sh} is high enough. This may allow a greater room for designing indoor photovolatic materials. This study may provide useful tips to further optimize organic photovoltaic materials and devices for indoor applications.

Chapter 5. High Efficiency Bilayer Organic Photovoltaic Cells Enabled by Large Extinction Coefficients, High Exciton Diffusion Lengths, and Interlayer Energy Transfer

5.1 Research Backgrounds

Organic photovoltaics (OPVs) hold great promise due to their tunability, flexibility, and potential for ultracheap production. In π-conjugated organic semiconductors - the key component of OPVs - light absorption and emission are governed by excitons.[123-124] Excitons can rarely travel beyond 5–10 nm in these materials – a constraint that has defined the field of OPVs for decades.[123-126] The bulk heterojunction design for the charge generation active layer arose to reconcile the mismatched length-scales of exciton diffusion (requiring charge-separating junctions distributed on a 5–10 nm scale), and light absorption (requiring >100 nm film thicknesses).[127]

From a materials and device design perspective, the bulk heterojunction (BHJ) has severe drawbacks, namely: i) reduced power conversion efficiency (PCE) from charge trapping and field-dependent separation and recombination at buried interfaces;[128] and ii) disproportionate research emphasis on the semi-empirical art of controlling non-equilibrium phase stability[129] – through tuning donor and acceptor ratios, their solubility and crystallinity, deposition solvents and processing temperatures, film thicknesses[21, 46, 130-132]– as well as significant effort devoted to characterising complex and disordered film morphologies on many lengthscales from large phases to crystal domains and buried interface orientations.[133-134] The challenge in optimising the BHJ for a given set of materials has led to insufficient focus on intrinsic optoelectronic properties, as well as lack of ability to perform any form of interfacial engineering.[133] This means that materials designed for their favourable absorption and electronic properties often perform poorly in OPVs due to unfavourable morphologies, resulting in just a handful of OPV materials setting efficiency records, out of >35,000 publications to date.[135]

Bilayer, rather than BHJ, OPVs have been studied to elucidate intrinsic material and interfacial properties, despite their low efficiencies (around 3%).[136-137] However, even this effort has been severely hindered by the difficulty of achieving clean interfaces free from percolation and interpenetration between the donor and acceptor layers[138], and so it is difficult to state a definitive record PCE. Recently, sequential deposition methods have achieved high PCEs (> 11%) through the use of similar solvents or by intentionally adding good solvents, resulting in strong phase separation for donor and acceptor layers, but still only pseudo-bilayers.[139-140] For perfect bilayer heterojunctions, orthogonal solvents for donor and acceptor layers are required to avoid swelling or dissolution of the bottom layer. If high PCEs can be achieved by genuine bilayer heterojunctions, large area devices could be more easily fabricated due

to reduced device optimization variables[141], leading to higher reproducibility, even with solution-processing.

The recent invention of fused-ring electron acceptors (FREAs) has sparked a step-change, propelling the PCE of BHJ devices beyond fullerene-based devices.[142-144] Key factors that have powered this rise, such as high absorption coefficients[145] (greater than 2×10^5 cm^{-1}), complementary donor and acceptor absorption profiles,[146] and high exciton diffusion lengths (exceeding 30 nm), [147] along with the steady improvement of polymeric donor materials, lend themselves to the potential for drastically increasing the PCEs of bilayer OPVs.

With the advent of FREAs, the concept of using Förster resonant energy transfer (FRET) to enhance OPV efficiency has also seen increased interest.[148-151] But without creating clean bilayers, and considering the low absorption coefficients and low molecular densities of the previously used fullerene acceptor layers, the potential for efficient 'slab to slab' energy transfer[152-153] has so far gone largely unexplored and unrealised.

In this work, we fabricated a variety of different bilayer devices based on simple design principles: we used orthogonal solvents for clean bilayer layer deposition, and chose active materials with high absorption coefficients and low Stokes shifts to maximise exciton diffusion lengths relative to absorption length within layers, and sought to increase long-range donor-to-acceptor FRET between layers. **Figure 5.1c** illustrates the key excitonic processes – exciton diffusion through self-FRET shown by green arrows, long-range donor-to-acceptor FRET by the white arrow, and charge separation at the three active layer interfaces. This approach results in bilayer devices with PCEs up to 11%. Through transmission electron microscopy (TEM) and grazing-incidence wide-angle X-ray scattering (GIWAXS), we confirm that our devices have clean bilayer interfaces with minimal percolation. Alongside our electrical characterisations of the device efficiencies and bimolecular recombination, we rationalise our record-breaking efficiency values through a combination of ultrafast transient absorption spectroscopy and optical modelling to independently account for exciton diffusion lengths and interlayer FRET. This study shows that efficient photovoltaic devices can be fabricated from organic materials without requiring the complexities of the BHJ architecture, and paves the way for a new wave of advancement through new and simplified material and device design rules.

.

5.2 Experimental Details

General: UV-Vis absorption spectra were obtained using Carry 5000 (Agilent) and a Cary 50 Bio UV-vis spectrometer in the range 190 – 1100 nm. Photoluminescence spectra were obtained using a Cary Eclipse (Varian). Photoluminescence quantum efficiency measurements were obtained in an integrating sphere using the method of de Mello et al.[154] AFM images were obtained using a Veeco AFM microscope in a tapping mode. Cross-sectional TEM samples were prepared using a focused ion beam (FIB) instrument of Helios 450HP FIB (FEI) and HR- TEM images were obtained using a JEM-2100F (JEOL). GIWAXS measurements were carried out at the PLS-II 9A U-SAXS beam line of Pohang Accelerator Laboratory. Refractive indices were obtained by ellipsometer using an Elli-SE-UaM8 (Elipso Technology) with quartz substrates. Al_2O_3 layer was deposited by atomic layer deposition method using a Lucida D100 (NCD). Thickness was measured by surface profiler of P6 (KLA Tencor).

Fabrication and characterization of OPV devices: Pre-patterned ITO on glass substrates were sequentially cleaned by ultrasonication with distilled water, acetone, and isopropanol. PEDOT:PSS (AI4083) was spin-coated onto the ITO substrate and annealed at 150 °C for 10 min. For bilayer devices, PBDB-T-2F was{de Mello, 1997 #20} dissolved in chlorobenzene (CB):1,8-octanedithol (ODT) (100:1 volume ratio) with a concentration of 10 mg mL^{-1} at 100 °C. IDIC, ITIC and NIDCS-HO were dissolved in dichloromethane (DCM) with a concentration of 6.5 mg mL^{-1} at the room temperature (RT). IDICO1 and IDICO2 were dissolved in DCM:ODT (100:0.5 volume ratio) and DCM:1-chloronaphthalene (CN) (100:0.5 volume ratio) with a concentration of 6.5 mg mL^{-1} at the RT, respectively. PBDB-T-2F solutions were spin-cast on top of the PEDOT:PSS layer and thermal annealed at 100 °C for 5 minutes in an N_2-filled glove box. Then, the acceptor layer was spin-coated on top of PBDB-T-2F layer, and the ZnO layer was spin-coated, sequentially. For BHJ devices, D:A ratio is fixed to 1:1 (w/w). PBDB-T-2F:ITIC-Th1 and IDIC were dissolved in CB:ODT (100:0.01 volume ratio). PBDB-T-2F:IDICO1 was dissolved in 1,2-dichlorobenzene. PBDB-T-2F:IDICO2 and NIDCS-HO were dissolved in CB. After spin-coating, the BHJ films were annealed at 100 °C for 5 minutes. To deposit Al (100 nm) electrodes by thermal evaporation, a vacuum chamber was pumped down under ~10^{-7} Torr. The area of the Al electrode defined an active area of 4 mm^2. *J-V* characteristics were collected with a Keithley 2635A source measurement unit inside the N_2-filled glove box using a high quality optical fiber to guide the light from a solar simulator to the device. Light intensities were modulated with neutral density filters to measure the light intensity dependent photovoltaic parameters. EQE measurements were performed using a PV measurement QE system using monochromatic light from a xenon lamp under ambient conditions. The monochromatic light was chopped at 100 Hz and the device was measured relative to a standard Si photodiode using a lock-in-amplifier.

Transient absorption spectroscopy: Femtosecond transient absorption (TA) measurements are performed using a homebuilt experimental setup illuminated by an amplified Ti:sapphire laser emitting pulses of 100 fs time duration, centred around 800 nm and at a repetition rate of 3 kHz. The excitation pulses are generated using an optical parametric amplifier (TOPAS) with the 800 nm fundamental input and then chopped at $\omega/2$ (1.5 kHz). Photoexcitations in the materials were probed via a broadband white light continuum generated by focusing a portion of the fundamental to an undoped YAG (Yttrium Aluminium Garnet) crystal. Pump-probe polarizations were kept under magic angle (54.7^0) configuration to avoid orientational dynamics. After passing through the photoexcited sample, the probe pulses were spectrally dispersed using a prism spectrometer and are then collected using a CMOS camera (visible components) or an InGaAs photodiode array (IR components). The time resolution is obtained via introducing time delays in the pump path which is achieved using a retroreflector connected to a motorized translational stage. The differential transmission signals at various time delays are calculated from the sequential probe shots corresponding to the pump on versus off. For typical measurements, 8000 shots were averaged at each time point and were repeated at least four times. The data were saved as binary files and then processed via MATLAB software including chirp and background corrections. To avoid degradation, all the samples were measured under a vacuum environment.

.

5.3 Results and Discussion

Results

For bilayer organic solar cells, light harvesting efficiency is governed by the ratio between exciton diffusion length and absorption length. Larger self-FRET radii can be a good proxy for longer diffusion lengths[2] (L_D) and hence enhanced exciton harvesting. Self-FRET is governed by overlap of absorption and emission. As a first step in device design, we therefore focused on materials with high self-overlap (low Stokes shifts), high molecular densities, and large absorption coefficients (short absorption lengths). We fixed PBDB-T-2F as a donor polymer (proven as a highly efficient conjugated polymer in non-fullerene BHJ OPVs[155-158]), and compared 5 non-fullerene acceptors that have shown high PCEs in non-fullerene OPVs; ITIC-Th1[159], IDIC[160-161], IDICO1, IDICO2 and NIDCS-HO[162] (synthesis details of IDICO1 and IDICO2 are given in the experimental section). The first four, ITIC-Th1, IDIC, IDICO1 and IDICO2 have low Stokes shifts (~40 nm) and have a lower bandgap than the donor polymer, with NIDCS-HO chosen as a high Stokes shift (133 nm) control for contrast, which also has a different energetic alignment (a higher bandgap than the donor material).
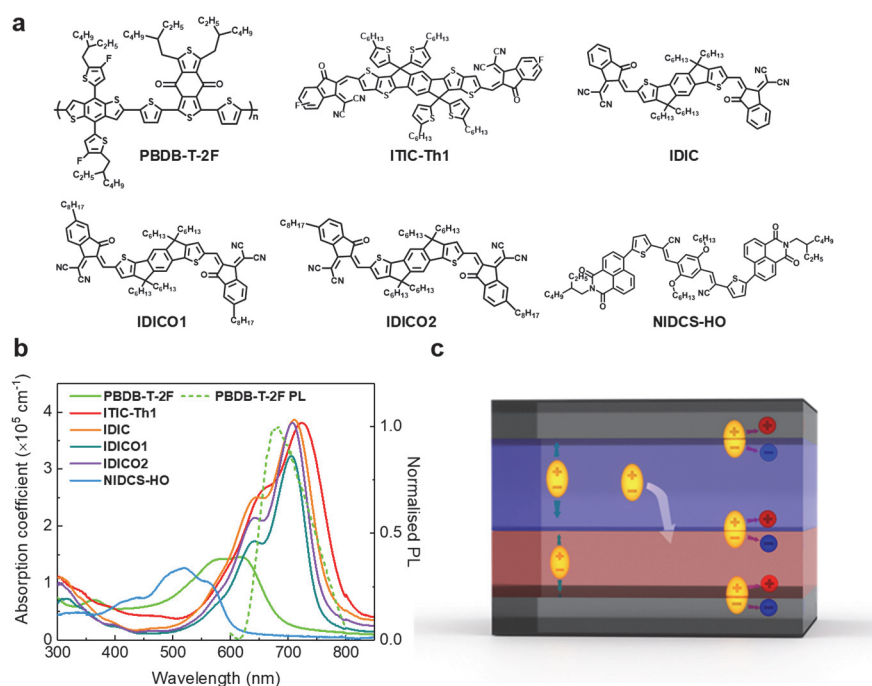
Figure 5. 1. (a) Molecular structures of PBDB-T-2F, ITIC-Th1, IDIC, IDICO1, IDICO2 and NIDCS-HO. (b) Absorption coefficient spectra of PBDB-T-2F, ITIC-Th1, IDIC, IDICO1, IDICO2 and NIDCS-HO pristine thin films, as obtained through ellipsometry, and PL of PBDB-T-2F donor. (c) Conceptual illustration of key excitonic processes in bilayer devices. Green arrows illustrate exciton diffusion through self-FRET, white arrow shows long-range donor-to-acceptor FRET and purple arrows show charge separation at the interfaces.
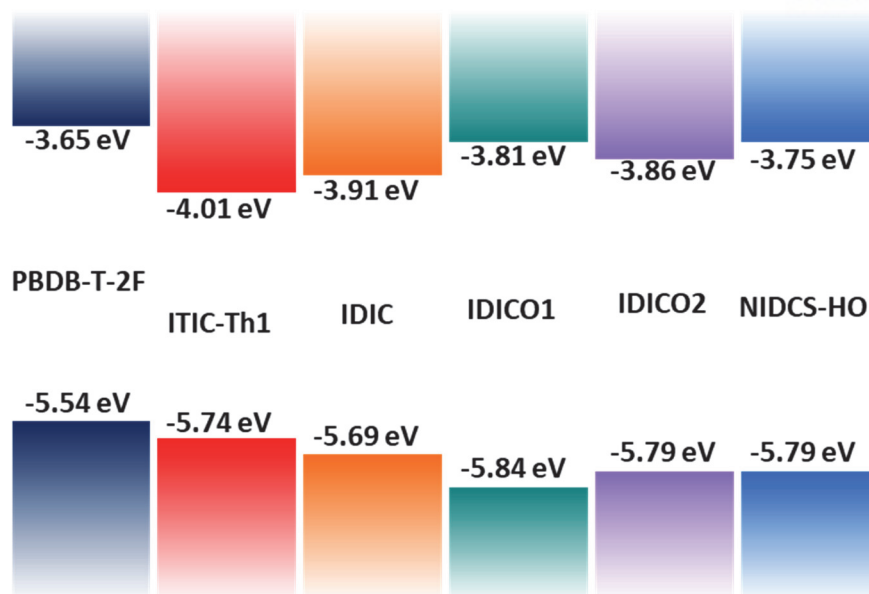
Figure 5. 2. Energy band diagram of PBDB-T-2F, ITIC-Th1, IDIC, IDICO1, IDICO2 and NIDCS-HO.

Detailed molecular structures of the materials are shown in **Figure 5.1a**. The energy band diagram of donor and acceptors is shown in **Figure 5.2**. Each combination of donor and acceptor is energetically appropriate for photovoltaic function. **Figure 5.1b** shows the exceptionally high absorption coefficients of the donor and acceptor materials. This enables a high absorption fraction across the visible spectrum for very thin layers of the active materials. The absorption lengths are characterised in more detail below (in sections '*exciton diffusion lengths',* and *'D-A energy transfer'*), in relation to optical cavity effects, exciton diffusion lengths, and D-A FRET.

We fabricated bilayer films of donor-acceptor layers using orthogonal solvents, and confirmed via structural and spectroscopic measurements that a clean bilayer heterojunction was achieved. Donor and acceptor layers were deposited with chlorobenzene and dichloromethane (DCM), respectively. These are different enough solvents to enable selective solvation of the acceptor small molecules (in DCM) without affecting the deposited PBDB-T-2F layer. **Figure 5.3a** shows a representative cross-sectional TEM image of a bilayer film of PBDB-T-2F and IDIC. In the magnified image, PBDB-T-2F and IDIC layers are well distinguished with different contrasts (originating from the different molecular structure of the conjugated polymer and small molecules).

We also confirmed formation of clean bilayer-heterojunctions by grazing incidence wide angle X-ray scattering (GIWAXS) for our materials combinations, as shown in **Figure 5.3b,** with PBDB-T-2F/IDIC chosen as a representative example (crystallographic parameters summarized in **Table 5.1** and **5.2**).
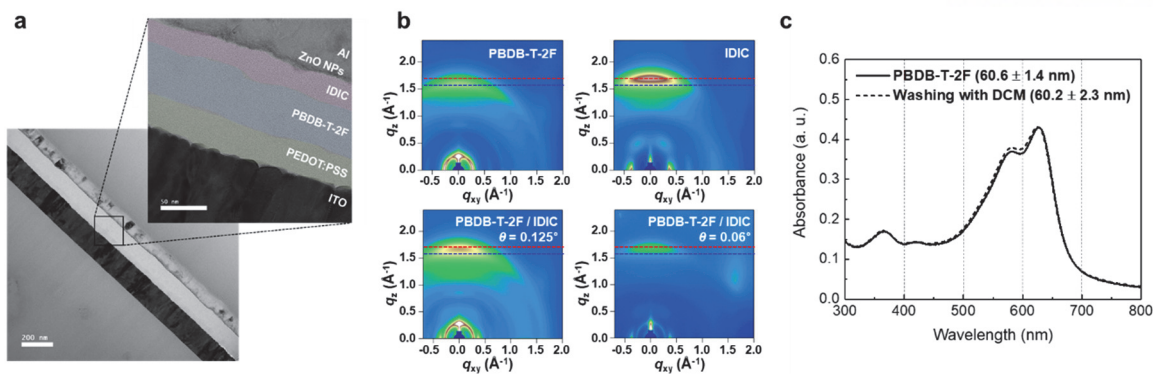
Figure 5. 3. Confirmation of bilayer structures. (a) Cross-section TEM images for PBDB-T-2F/IDIC bilayer OPVs. (b) GIWAXS pattern images for PBDB-T-2F, IDIC pristine films and PBDB-T-2F/IDIC bilayer film with different incident angle of X-ray of 0.125° and 0.06°. (c) Absorption of PBDB-T-2F neat film before and after washing with dichloromethane (DCM) which is solvent of acceptor layer deposition.

For each donor/acceptor pair, we compared crystalline properties of neat donor PBDB-T-2F, neat acceptor and a PBDB-T-2F/acceptor bilayer. In the case of the bilayer sample, different X-ray angles (θ) of 0.125° and 0.06° were used to distinguish the top and bottom layers. Using IDIC as a characteristic example acceptor layer, at higher θ = 0.125°, all crystalline packing peaks originated from pristine PBDB-T-2F. At smaller θ = 0.06°, identical crystalline peaks with pristine IDIC were observed. The identical packing structures of pristine IDIC and IDIC in the bilayers imply that donor and acceptor layers are well distinguished in our bilayer system. The other bilayer systems showed the same characteristics as the PBDB-T-2F/IDIC layer (**Figure 5.4-5.8**). Furthermore, the surface morphology (**Figure 5.9**) of the bottom of the bilayer film (PBDB-T-2F) after washing out the IDIC layer was almost identical compared to pristine PBDB-T-2F films, as were the PBDB-T-2F film absorption spectrum and total film thickness, as shown in **Figure 5.3c**. This indicates that PBDB-T-2F film was not affected during film formation of the top acceptor layer.
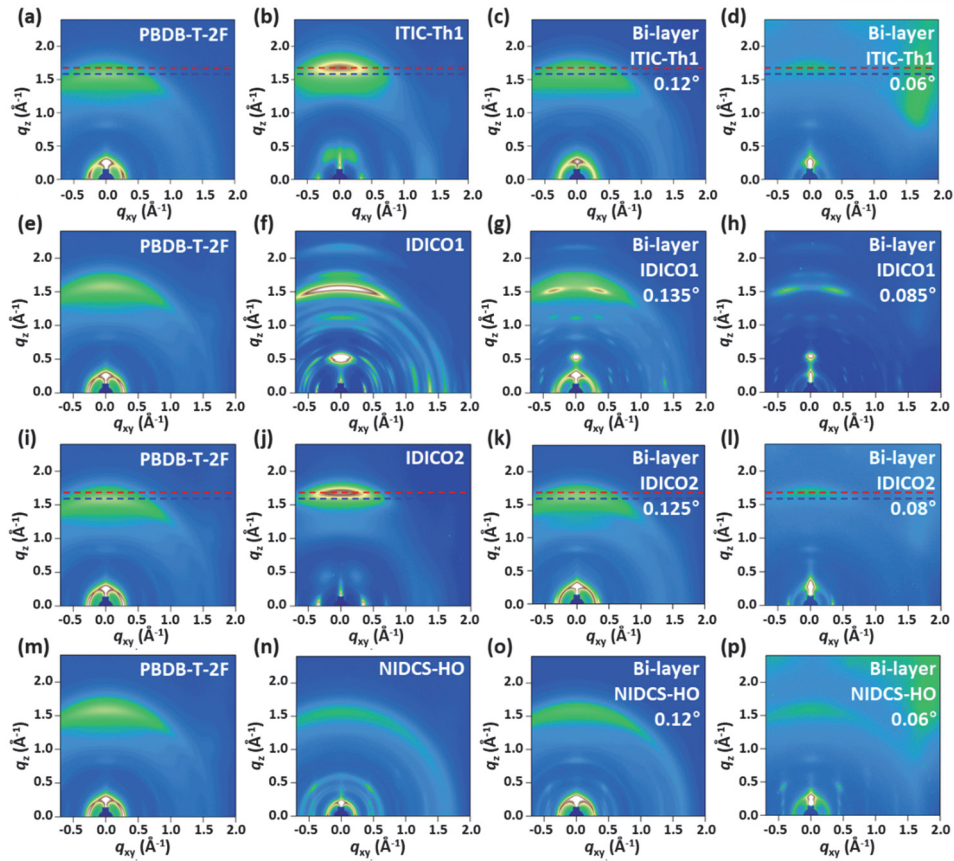
Figure 5. 4. GIWAXS patterns of pristine PBDB-T-2F, ITIC-Th1, IDICO1, IDICO2 and NIDCS-HO films and PBDB-T-2F/ITIC-Th1, IDICO1, IDICO2 and NIDCS-HO bilayer films.
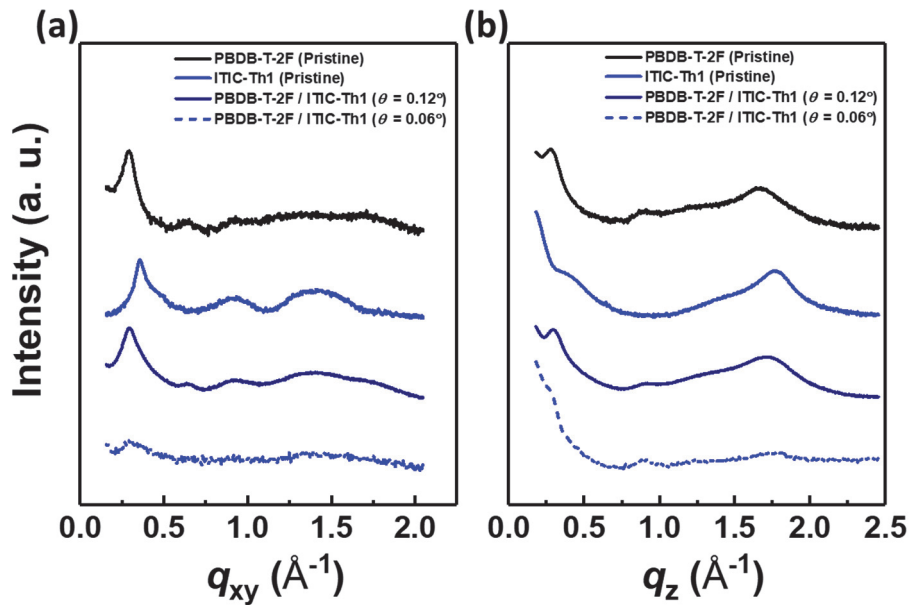
Figure 5. 5. GIWAXS line-cut profiles along (a) in-plane (qxy) and (b) out-of-plane (qz) direction for PBDB-T-2F, ITIC-Th1 pristine films and PBDB-T-2F/ITIC-Th1 bilayer films.
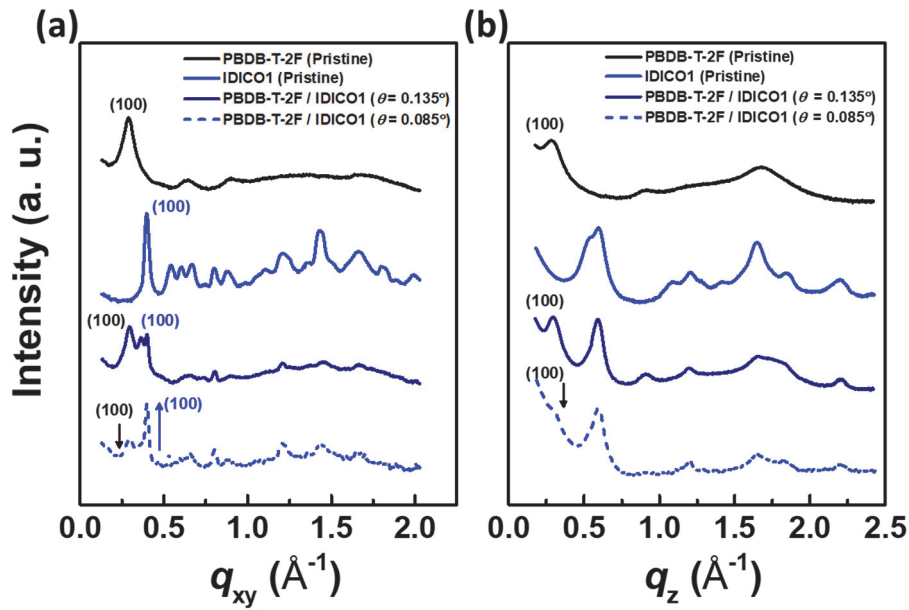
Figure 5. 6. GIWAXS line-cut profiles along (a) in-plane (q_{xy}) and (b) out-of-plane (q_z) direction for PBDB-T-2F, IDICO1 pristine films and PBDB-T-2F/IDICO1 bi-layer films.
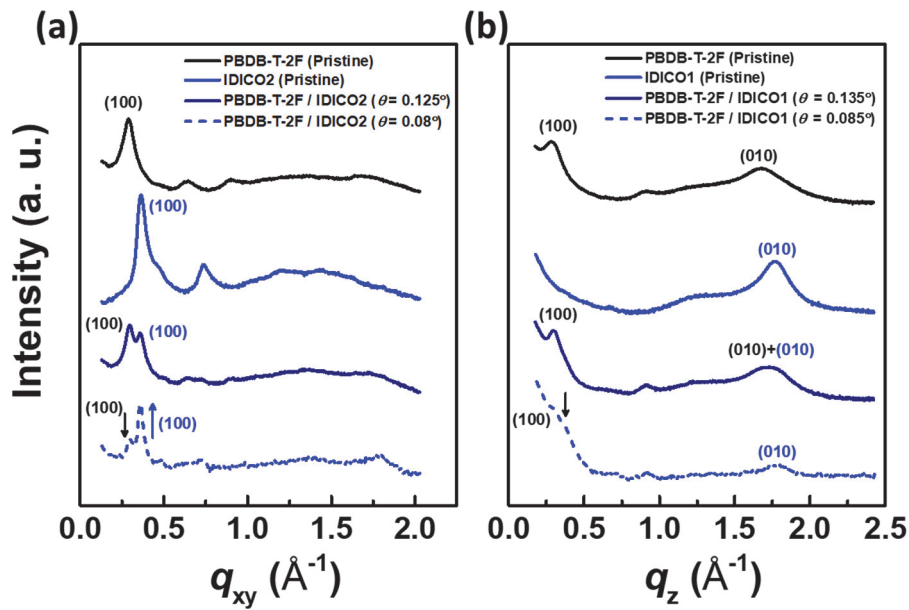
Figure 5. 7. GIWAXS line-cut profiles along (a) in-plane (q_{xy}) and (b) out-of-plane (q_z) direction for PBDB-T-2F, IDICO2 pristine films and PBDB-T-2F/IDICO2 bi-layer films.
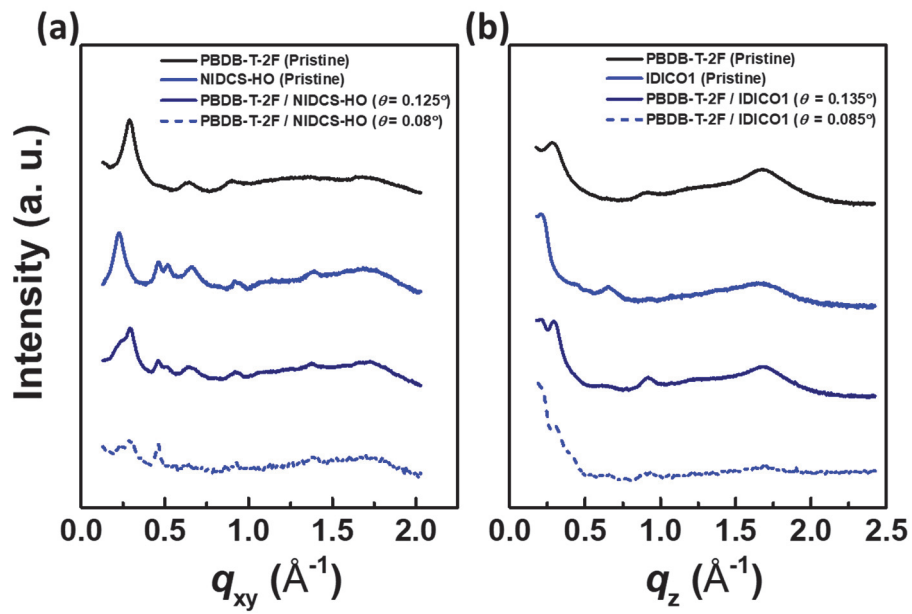
Figure 5. 8. GIWAXS line-cut profiles along (a) in-plane (q_{xy}) and (b) out-of-plane (q_z) direction for PBDB-T-2F, NIDCS-HO pristine films and PBDB-T-2F / NIDCS-HO bi-layer films.

Table 5. 1. Summary of crystallographic parameters of PBDB-T-2F, ITIC-Th1 and PBDB-T-2F/ITIC-Th1 bilayers with different incident angles (θ) of 0.125° and 0.06°. At $\theta \sim 0.12°$, incident X-rays can penetrate the bilayer films deeply, so crystalline structure information of both donor and acceptor layer is obtained. With lowered $\theta \sim 0.06°$, incident X-rays graze the surface of bilayer films, giving crystalline structure information on the top of the bilayer.)

Film	In-plane (Lamellar)		Out-of-plane (Lamellar)	
	q_{xy} (Å^{-1})	d-spacing (Å)	q_z (Å^{-1})	d-spacing (Å)
PBDB-T-2F	0.291	21.6	0.282	22.3
ITIC-Th1	0.356	17.6	-	-
PBDB-T-2F/ITIC-Th1 (θ=0.125°)	0.295	21.3	0.297	21.2
PBDB-T-2F/ITIC-Th1 (θ=0.06°)	0.293	21.4	-	-
Film	In-plane (π-π stacking)		Out-of-plane (π-π stacking)	
	q_{xy} (Å^{-1})	d-spacing (Å)	q_z (Å^{-1})	d-spacing (Å)
PBDB-T-2F	-	-	1.663	3.78
ITIC-Th1	-	-	1.773	3.54
PBDB-T-2F/ITIC-Th1 (θ=0.12°)	-	-	1.704	3.69
PBDB-T-2F/ITIC-Th1 (θ=0.06°)	-	-	1.769	3.55

Table 5. 2. Summary of crystallographic parameters of PBDB-T-2F, IDIC and PBDB-T-2F/IDIC bilayer with different incident angle of 0.125° and 0.06°. At $\theta \sim 0.12°$, incident X-rays can penetrate the bilayer films deeply, so crystalline structure information of both donor and acceptor layer is obtained. With lowered $\theta \sim 0.06°$, incident X-rays graze the surface of bilayer films, giving crystalline structure information on the top of the bilayer.)

Film	In-plane (Lamellar)				Out-of-plane (Lamellar)	
	q_{xy} (Å^{-1})		d-spacing (Å)		q_z (Å^{-1})	d-spacing (Å)
PBDB-T-2F	0.289		21.7		0.287	21.9
IDIC	0.383		16.4		-	-
PBDB-T-2F/IDIC (θ=0.125°)	0.289	0.388	21.7	16.2	0.306	20.5
PBDB-T-2F/IDIC (θ=0.06°)	0.288	0.390	21.8	16.1	-	-

Film	In-plane (π-π stacking)		Out-of-plane (π-π stacking)	
	q_{xy} (Å^{-1})	d-spacing (Å)	q_z (Å^{-1})	d-spacing (Å)
PBDB-T-2F	-	-	1.678	3.74
IDIC	-	-	1.775	3.54
PBDB-T-2F/IDIC (θ=0.125°)	-	-	1.751	3.59
PBDB-T-2F/IDIC (θ=0.06°)	-	-	1.773	3.54
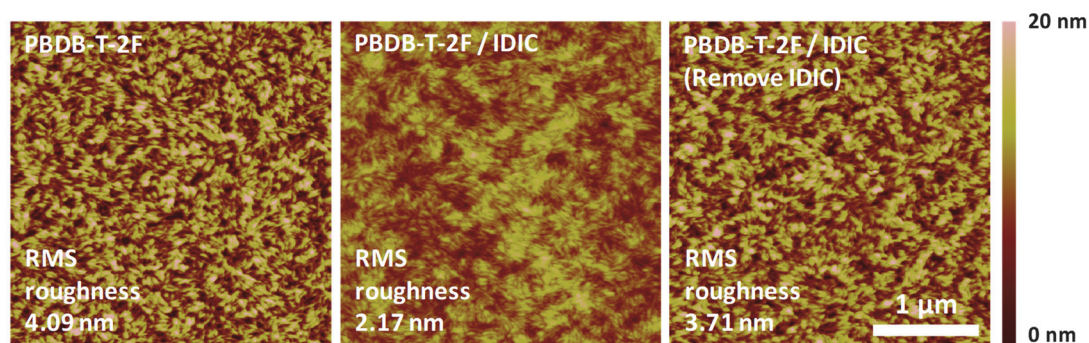
Figure 5. 9. Surface roughness and morphologies for PBDB-T-2F pristine, PBDB-T-2F/IDIC bilayer films and PBDB-T-2F/IDIC bilayer film after IDIC removal.

With this confirmation of clean bilayer structure, we fabricated complete bilayer solar cells. Remarkably, PBDB-T-2F/ITIC-Th1, IDIC, IDICO1 and IDICO2 bilayer OPVs exhibited excellent device performances of around 9-11%. Current density–voltage (*J-V*) curves and external quantum efficiency (EQE) spectra are shown in **Figure 5.10**, and photovoltaic parameters are summarized in **Table 5.3,** along with active layer thicknesses. Specifically, PBDB-T-2F/ITIC-Th1 devices showed the best PCE of 11% with J_{SC} of 16.9 mA cm^{-2}, V_{OC} of 0.94 V and FF of 0.69. These are the highest reported efficiencies for a clean bilayer OPV. PBDB-T-2F/NIDCS-HO devices exhibited the lowest PCE of 2.57% and a low FF of 0.35.
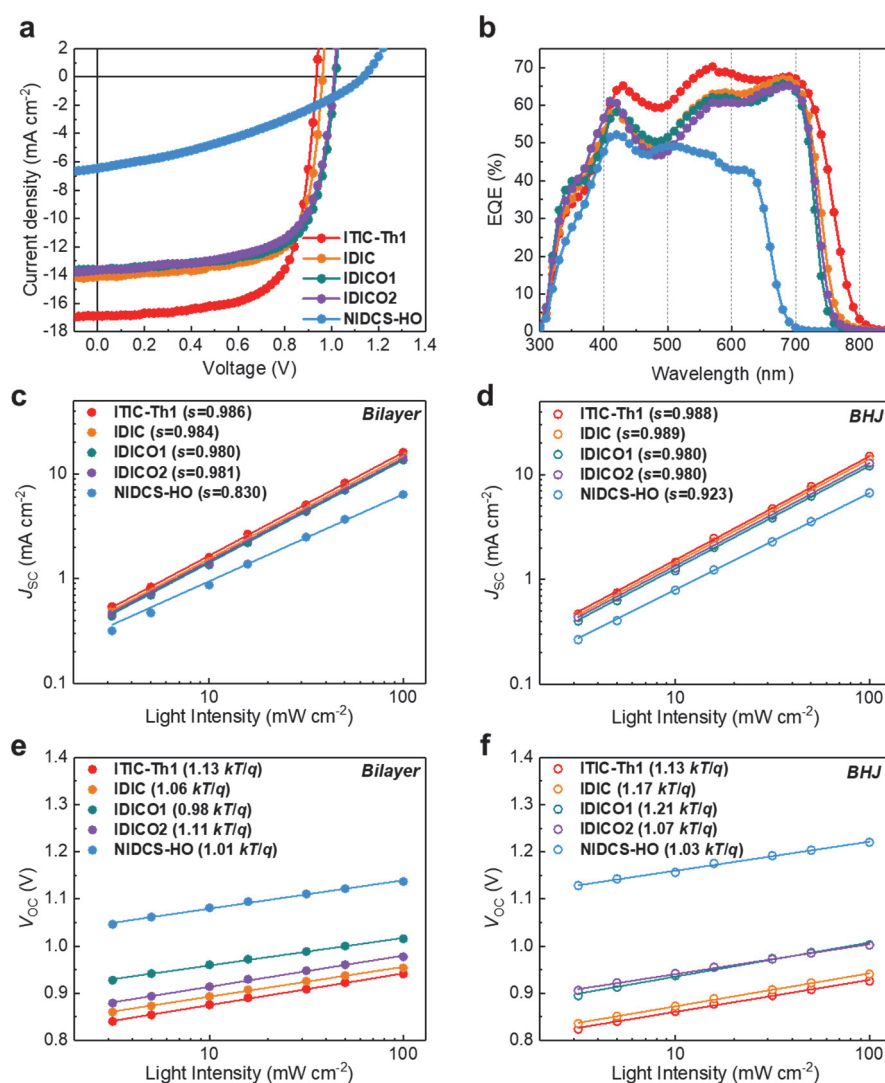
Figure 5. 10. Photovoltaic device performance of bilayer devices, and bimolecular and SRH recombination properties of bilayer- and bulk-heterojunctions. (a) *J-V* characteristics and (b) EQE spectra of PBDB-T-2F/Acceptors bilayer OPVs. (c, d) J_{SC} vs. I_{light} of bilayer and BHJ devices, respectively, showing bimolecular recombination characteristics. (e, f) V_{OC} vs. I_{light} of bilayer and BHJ devices, respectively, quantifying degree of SRH recombination.

Table 5. 3. Summary of photovoltaic parameters for PBDB-T-2F/Acceptor bilayer and PBDB-T-2F:Acceptor bulk-heterojunction organic solar cells.

Active layer	Acceptor	Bilayer Thickness (D/A) [nm]	J_{SC} [mA cm^{-2}]	V_{OC} [V]	FF	PCE[a] [%]
	ITIC-Th1	50/35	16.9	0.94	0.69	11.0 (10.5 ± 0.36)
	IDIC	50/30	14.1	0.96	0.71	9.59 (9.30 ± 0.17)
Bilayer	IDICO1	50/20	13.6	1.02	0.69	9.51 (9.14 ± 0.28)
	IDICO2	50/18	13.7	1.01	0.66	9.15 (8.93 ± 0.13)
	NIDCS-HO	50/33	6.46	1.13	0.35	2.57 (2.32 ± 0.20)
Active layer	Acceptor	BHJ Thickness [nm]	J_{SC} [mA cm^{-2}]	V_{OC} [V]	FF	PCE[a] [%]
	ITIC-Th1	124	16.9	0.93	0.71	11.2 (10.7 ± 0.26)
	IDIC	113	14.4	0.95	0.72	9.87 (9.62 ± 0.15)
BHJ	IDICO1	114	11.8	1.01	0.64	7.57 (7.33 ± 0.17)
	IDICO2	125	13.8	1.00	0.66	9.19 (8.70 ± 0.28)
	NIDCS-HO	120	6.35	1.23	0.61	4.78 (4.29 ± 0.22)

[a]Average PCE and standard deviation obtained from 10 devices.

We compared these bilayer efficiency results with those of bulk heterojunction solar cells made from the same materials. For BHJ devices, we fixed the donor:acceptor ratio at 1:1, and used pre-annealing or solvent additive strategies to optimize film morphologies. Both sets of devices were fabricated with conventional structures. Detailed fabrication procedures are described in the *Experimental Section*, and corresponding photovoltaic characteristic is shown in **Figure 5.11**. PBDB-T-2F:ITIC-Th1 bulk heterojunction (BHJ) devices showed the best power conversion efficiencies (PCEs) of 11.2% with a high short-circuit current density (J_{SC}) of 16.9 mA cm^{-2}, open-circuit voltage (V_{OC}) of 0.93V and fill factor (FF) of 0.71. PBDB-T-2F:IDIC, IDICO1 and IDICO2 BHJ devices showed also high PCEs of 9.87%, 7.57% and 9.19%, respectively, while PBDB-T-2F:NIDCS-HO BHJ devices showed relatively low PCE of 4.78% due to limited light absorption and J_{SC} with its large bandgap. Nonetheless, all of the BHJ devices exhibited adequate FF over 0.60 even in the PBDB-T-2F:NIDCS-HO devices.

Comparisons of the fill factor and PCE ratio of bilayer/BHJ are shown in **Figures 5.11c** and **5.11d**, respectively. Both FF and PCE ratio for the devices of PBDB-T-2F with ITIC-Th1, IDIC, IDICO1 and IDICO2 are around 1. In contrast, PBDB-T-2F with NIDCS-HO devices, both FF and PCE ratio were poor of 0.57 and 0.55, respectively. This indicates this system is not appropriate in bilayer-heterojunction OSCs due to inefficient exciton diffusion and lack of interlayer energy transfer.
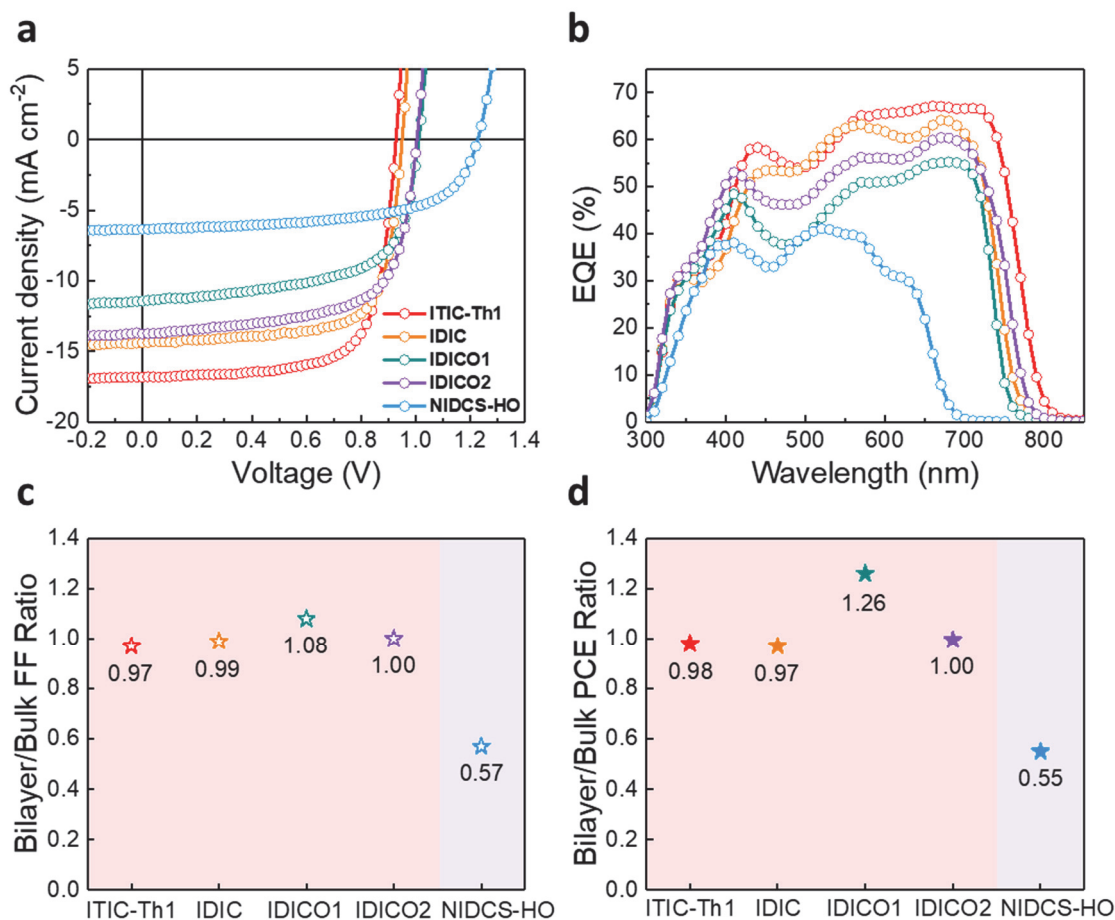
Figure 5. 11. Photovoltaic device performance of bulk-heterojunctions. (a) Current density-voltage (*J-V*) characteristics and (b) external quantum efficiency (EQE) spectra of PBDB-T-2F/Acceptor bulk-heterojunction solar cells. (c) Fill factor and (d) PCE ratios of bilayer/bulk-heterojunction solar cells with different acceptor materials.

Figures 5.3c and **5.3d** indicate the degree of bimolecular recombination in bilayer vs BHJ devices. In general, J_{SC} is proportional to $(I_{light})^s$. If the exponent *s* is close to unity, the system has negligible bimolecular recombination.[94] In contrast, *s* is lower than 1 when significant bimolecular recombination or space charge effects exist in the system.[163-164] PBDB-T-2F/ITIC-Th1, IDIC, IDICO1 and IDICO2 bilayer OPVs exhibited almost identical *s* values within the range of 0.980~0.986 – comparable to the BHJs – implying balanced charge carrier densities in the bilayer devices and that charge carriers are efficiently extracted without bimolecular recombination and space charge effects. However, PBDB-T-

2F/NIDCS-HO bilayer devices exhibited a low *s* value of 0.830, compared to a higher *s* of 0.923 in their BHJ counterparts.

Figures 5.3e and **5.3f** assesses the levels of Shockey-Read-Hall recombination present in our devices. From the slope of V_{OC} vs. the natural logarithm of I_{light} (close to kT/q), we see low levels of SRH recombination in both bilayer and BHJ devices.[94]

Monomolecular recombination mechanisms were investigated by normalized photocurrent density–voltage (J_{ph}-V) characteristics and V_{OC} dependence on incident light intensities (I_{light}) as shown in **Figure 5.12**. J_{ph} was obtained through $J_{ph}=J_{total}–J_{dark}$, where J_{total} is total current density and J_{dark} is dark diode current. By normalizing J_{ph} with reverse saturation photocurrent ($J_{ph,sat}$), charge collection probability can be obtained. In the voltage range from reverse bias to voltage at maximum power point (V_{MPP}), $P_C(I,V)$ curves are highly influenced by monomolecular recombination instead of bimolecular recombination, since free charge carriers can be quickly swept out to the electrodes due to the high electric field in the devices.
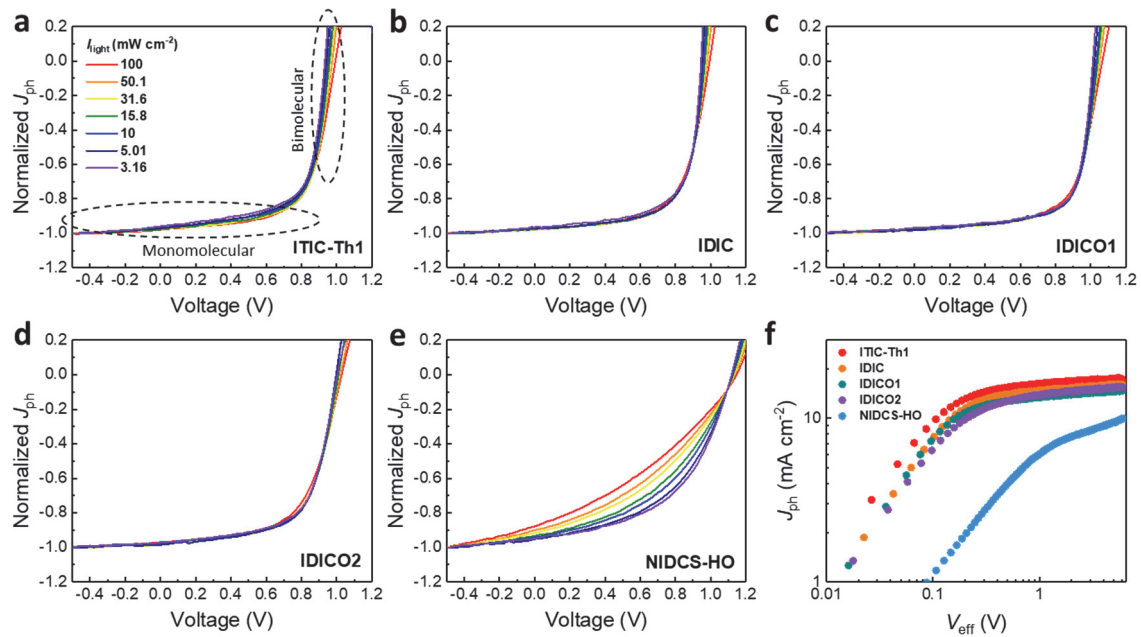
Figure 5. 12. Monomolecular recombination mechanisms in bilayer solar cells. Normalized photocurrent density–voltage (J_{ph}–V) characteristics as a function of incident light intensity of the bilayer OSCs of (a) ITIC-Th1, (b) IDIC, (c) IDICO1, (d) IDICO2, (e) NIDCS-HO acceptors with PBDB-T-2F donor. (f) J_{ph}-V_{eff} characteristics of the bilayer OSCs.

Conversely, in the voltage range from V_{MPP} to V_{OC}, $P_C(I,V)$ curves are dependent on $I_{light,}$ indicating bimolecular recombination predominates. This is generally attributed to low internal potential in the devices due to the large applied forward bias.[1–3] For bilayer OPVs with acceptors comprised of ITIC-Th1, IDIC, IDICO1 and IDICO2, normalized J_{ph} curves were almost identical and well saturated in the voltage range from -0.5 V to V_{MPP} regardless of I_{light} as shown in **Figures 5.12a-d**, respectively. Charge carriers can be efficiently extracted to the electrodes with balanced charge carrier densities. In contrast, a wide spread of normalized J_{ph} characteristics in the voltage range from 0.5 V to V_{MPP} was observed for the PBDB-T-2F/NIDCS-HO devices as shown in **Figure 5.12e**.

Charge collection probability ($P(E,T)$) at short circuit condition was obtained from photocurrent density–effective voltage (J_{ph}–V_{eff}) characteristics, as shown in **Figure 5.12f**. (In this case, the curves were scanned from ~ 0.01 V to sufficiently high V_{eff} ~ 6 V to extract all free charge carriers fully under AM1.5G intensity.) For the devices with IDIC group, free charge carriers were efficiently collected at the electrodes with over 90% $P(E,T)$ at short-circuit condition. On the other hand,, very poor $P(E,T)$ of 65% was obtained in NIDCS-HO bilayer devices. In summary, negligible monomolecular and bimolecular recombination result in excellent device performance of over 9% PCEs for the bilayer OPVs through using IDIC-type acceptors. For the bilayer devices with NIDCS-HO (larger Stokes shifts and minimal donor-to-acceptor FRET), both monomolecular and bimolecular recombination negatively influence device performance.

Having demonstrated these exceptional efficiencies for bilayer OPV devices, we now interrogate the key parameters that make these efficiencies possible.

The crucial factor determining light harvesting efficiency is the ratio of diffusion length to absorption length. Based on the absorption coefficients already presented in **Figure 5.1c**, we show, in the first row of **Table 5.4,** the characteristic peak absorption lengths (the length at which 1/e of incident light is transmitted) for the donor and acceptor materials. Considering optical cavity effects, for PBDB-T-2F/ITIC-Th1 devices for instance, these values translate into high fractions (>80%) of absorbed light over a broad wavelength range for thin (80 nm) active layer thicknesses (**Figure 5.15**).

Table 5.4 also summarises the predicted exciton diffusion lengths of the donor and acceptor materials (based on our initial self-FRET analysis for nearest-neighbour hopping), as illustrated by the overlaps depicted in the inset of **Figures 5.13a, b** and **c**. However, there are well known limitations to this analysis[165-166], (such as assumed nearest-neighbour hopping, and the point-dipole approximation) particularly for materials exhibiting longer exciton diffusion lengths. We therefore verified the exciton diffusion lengths through intensity-dependent transient absorption measurements. We probe the singlet state (spectra are shown in **Figure 5.14**) of the neat materials, and the intensity-dependent exciton decays are modelled with a global fit to an exciton rate equation accounting for both diffusion-driven
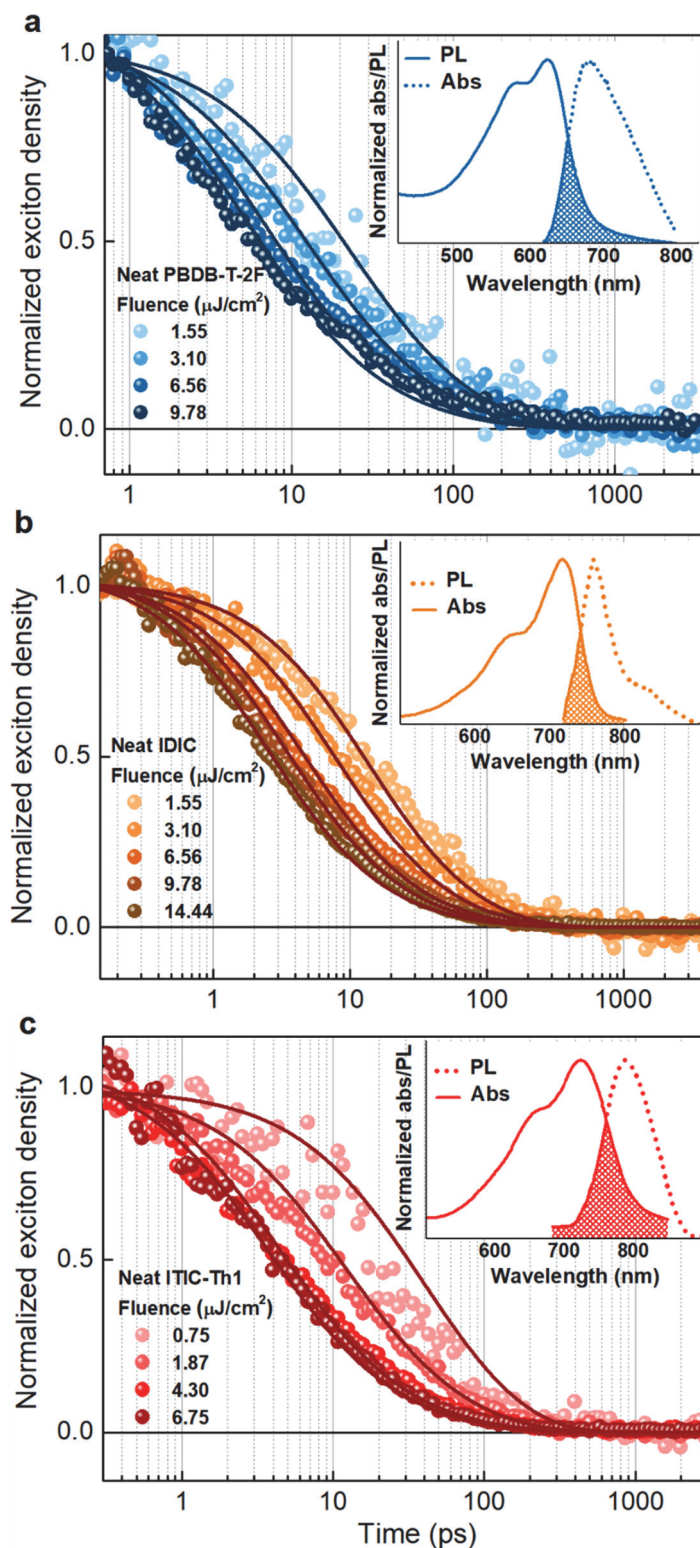
Figure 5. 13. FRET induced exciton diffusion in neat donor and acceptor materials. Singlet-singlet exciton annihilation model applied to fluence dependent exciton decays in the neat films of (**b**) PBDB-T-2F, (**c**) IDIC and (**d**) ITIC-Th1 (excited at 560 nm, 712 nm and 665 nm respectively) with the corresponding absorption and emission spectral overlaps in the inset.
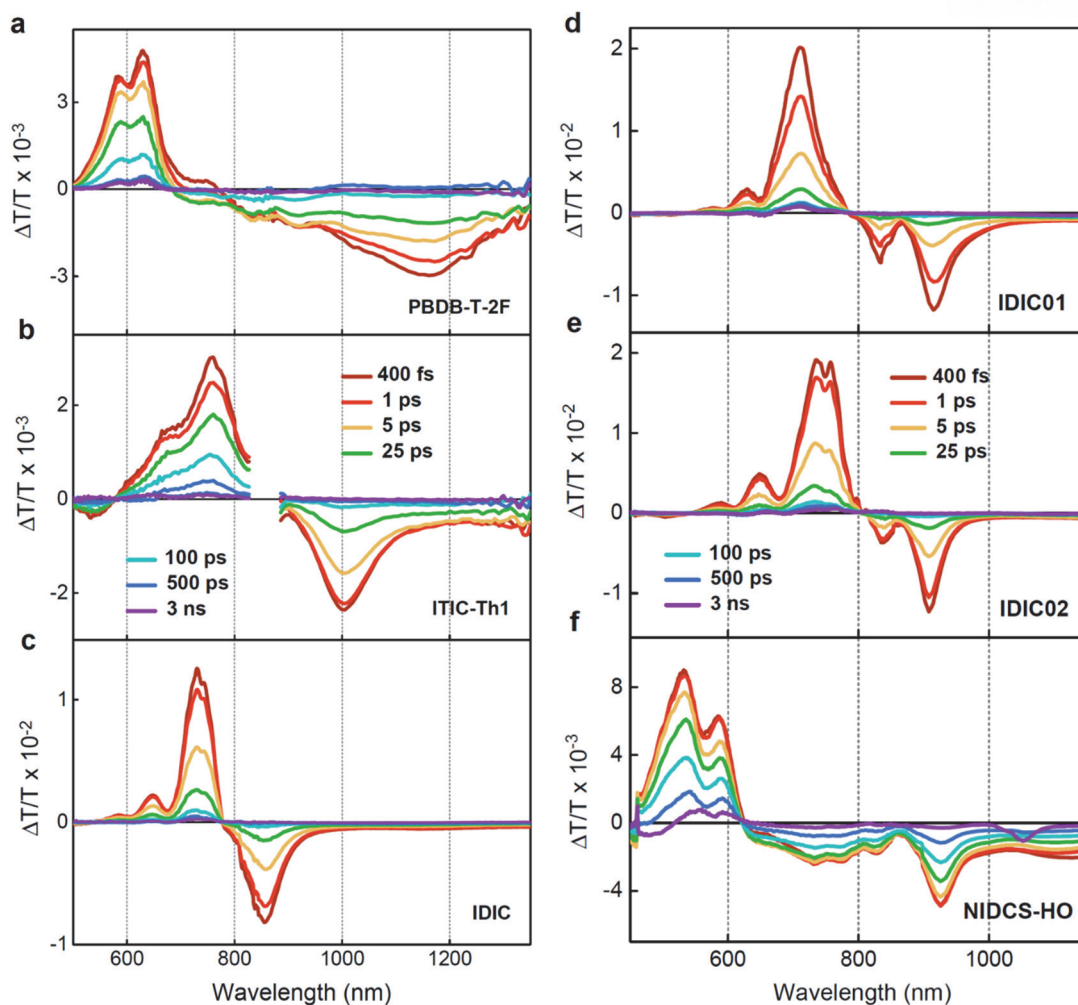
Figure 5. 14. Transient absorption spectra of neat donor, acceptor films. Series of Transient absorption spectra of (**a**) PBDB-T-2F (excited at 560 nm, at a pump fluence of 1.65 µJ/cm²), (**b**) ITIC-Th1 (excited at 665 nm, at a pump fluence of 1.87 µJ/cm²),   (**c**) IDIC (excited at 712 nm, at a pump fluence of 6.56 µJ/cm²), (d) IDICO1 (excited at 665 nm, at a pump fluence of 4.3 µJ/cm²), (e) IDICO2 (excited at 665 nm, at a pump fluence of 3.5 µJ/cm²) and (f) NIDCS-HO (excited at 600 nm, at a pump fluence of 13.8 µJ/cm²).
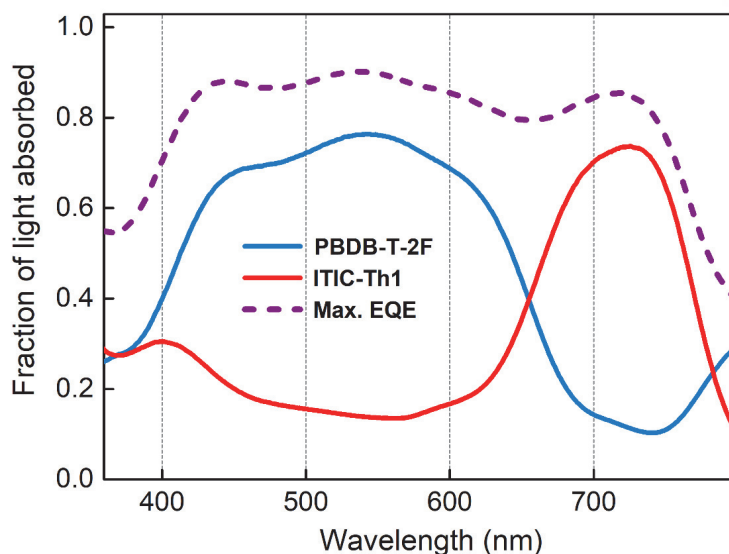
Figure 5. 15. Simulated light fractions absorbed by different active layers in a PBDB-T-2F/ITIC-Th1 bilayer device. Light fraction absorbed based on optical cavity calculation as per Burkhard *et al.*[4], based on measured absorption coefficients and refractive indices (**Figure 5.14**), and which includes contributions from parasitic absorption of interlayers, with 50 nm thickness of PBDB-T-2F and 35 nm ITIC-Th1. The blue curve is the total light absorbed in the active layers, thus representing the maximum possible EQE that can be achieved with this configuration if no recombination is present.
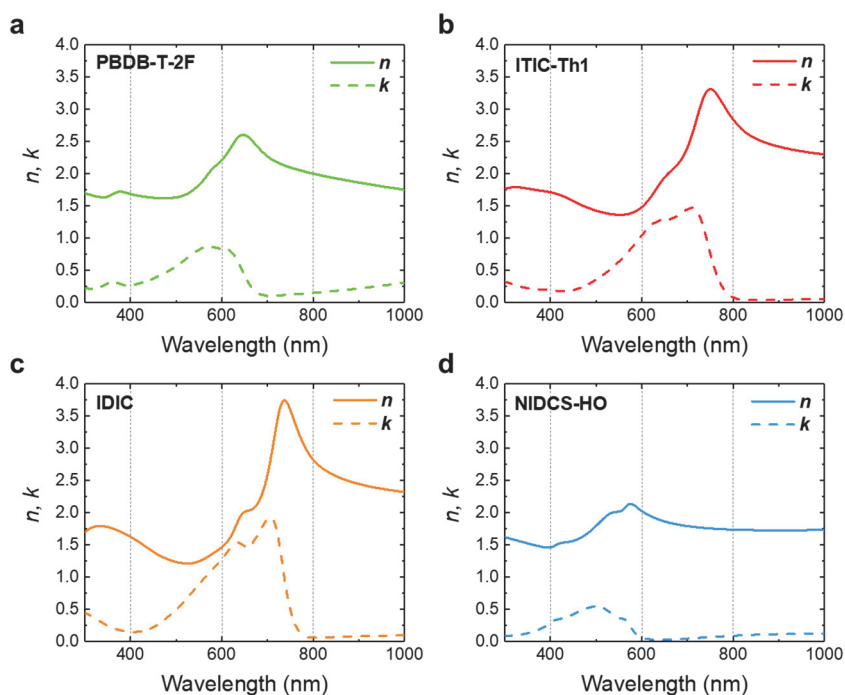
Figure 5. 16. Real and imaginary parts of the refractive index of donor and acceptor thin films.

Table 5. 4. Table of key optical parameters. For PBDB-T-2F, IDIC, ITIC-Th1, IDICO1, IDICO2 and NIDCS-HO. L_D (predicted) are based on self-overlap. L_D and D (the diffusion constant) in the adjacent columns are measured from TA annihilation kinetics, based on either a 3-D or 1-D diffusion model. $R_{1/2}$ is the donor (PBDB-T-2F) to acceptor distance for a 50% probability of donor-to-acceptor FRET.

Material	α [10^5 cm^{-1}]	Abs. length [nm]	Stokes shift [nm]	PLQE [%]	Lifetime [ps]	D_{3D} [10^{-2} cm^2 s^{-1}]	L_D predicted [nm]	L_D [nm]	R_0 [nm]	$R_{1/2}$ [nm]
PBDB-T-2F	1.48	67.6	55	1.4	178	7.2	3.8	35.8	2.1	-
ITIC-Th1	3.44	29.0	66	2.5	28-800[a]	4.0	5.0	10.6-56.6[a]	3.0	7.6
IDIC	4.95	20.2	48	3.0	126	10.0	5.6	35	2.4	5.1
IDICO1	5.3	18.9	38	8.4	62	8.0	17.5	20.3	3.5	5.6
IDICO2	4.9	20.4	40	9.3	52	8.9	16.0	23.5	3.4	5.8
NIDCS-HO	1.56	64.0	133	8.4	685	0.11	10.0	8.7[b]	2.9	-

a) Lower limits give experimental values while higher limits are from literature.

b) Diffusion coefficient and length from 3D diffusion model which is not fitted well with the data. But 1D diffusion model is fitted well and the details are given in the supporting information.

exciton annihilation and monomolecular decay pathways. The exciton annihilation method is particularly well-suited to measuring diffusion within bulk films without requiring dopants or interfaces, and for resolving fast exciton diffusion on short timescales. **Figures 5.13a, b** and **c** show the annihilation kinetics in neat films of PBDBT-2F, IDIC, and ITIC-Th1 respectively. Column 8 of **Table 5.4** summarizes the diffusion lengths obtained through this analysis, for these and the other specified electron acceptors NIDSC-HO, IDICO1 and IDICO2. These measurements confirm the high diffusion lengths (>30 nm) of the donor and best performing acceptor materials, affirming the vital importance of this parameter on the performance of bilayer architectured OPV. We note that there is substantial uncertainty in the lifetime of ITIC-Th1, and hence its diffusion length due to the possibility of a portion of intrinsic charge generation in the neat film[167], and limitations on the lowest excitation fluence we are able to achieve in transient absorption measurements. We also note that NIDCS-HO annihilation kinetics appear more accurately fit to a 1-D annihilation model, which would give an increased diffusion length of 39 nm.

The third key factor to which we attribute our high efficiencies is long-range Förster resonance energy transfer between donor and acceptor layers. Our best performing bilayer devices are highly favored for donor to acceptor (D-A) FRET, as illustrated by the large overlaps between the donor PBDBT-2F emission and absorption of ITIC-Th1 in **Figure 5.1b**. For PBDB-T-2F/ITIC-Th1 bilayers,

the estimated Förster radius is ~4 nm. While bulk heterojunction OPVs will also benefit from this effect[149, 168], the bilayer configuration lends itself to easier optimization of this process through dipole alignment, and also to easier quantification[150] of the degree of   D-A FRET, as exemplified in this study.

To confirm the presence of long-range energy transfer we constructed bilayer stacks with an inorganic charge blocking interlayer of atomic layer deposited Al_2O_3 between the donor and acceptor slabs. This Al_2O_3 layer prevents charge transfer/exciton separation at the interface, but allows donor to acceptor (D-A) FRET for thin enough blocking layers.

We applied ultrafast transient absorption spectroscopy to probe this D-A energy transfer in interlayer bilayer films. **Figure 5.17a** shows the TA spectra (at 5 ps) of a bilayer made with PBDB-T-2F and IDIC, excited by a 560-nm wavelength pump from the donor side, so that minimal light absorption occurs in the acceptor layer. The dotted curve is of a sample without a blocking layer, and shows a broader spectrum that includes contributions from donor charges, as well as excitons from both layers, making analysis difficult. However, for the sample with a 7 nm thick Al_2O_3 charge blocking layer, the spectrum is dominated by acceptor IDIC singlet excitons (which we identify by comparison with the neat film, non-bilayer TA spectra (**Figure 5.14**)), thus proving energy transfer without charge transfer. The sample with the thickest blocking layer (10 nm, dashed line) shows minimal IDIC excitonic signal, indicating suppressed D-A FRET.

By simultaneously probing the donor PBDBT-2F exciton signature and IDIC acceptor signature, we resolve the picosecond energy transfer kinetics from the donor to acceptor, due to exciton diffusion within the donor layer and FRET into the acceptor. In **Figure 5.17b** we see this transfer by the decay in donor exciton signal and concomitant rise in the acceptor signal that occurs within 30 ps. The acceptor signal is long-lived compared to that of the neat films as the exciton photo-induced absorption overlaps with that of charges formed at later time scales. Further evidence of efficient transfer is shown by the increased quenching (decreased lifetime) of the donor exciton signal in PBDBT-2F/IDIC bilayer films, as the thickness of the blocking interlayers is decreased (**Figure 5.18**).

We modelled the exciton dynamics with a 1-dimensional diffusion model[153] that includes a contribution from Förster resonance energy transfer from donor to acceptor, for a given interlayer thickness. Using the measured neat donor exciton lifetime and diffusion length, and the calculated Förster radius from PBDBT-2F to IDIC, of $R_0 = 2.8$ nm, we obtain good agreement with our measured transient absorption kinetics of donor and acceptor excitations, as seen by the solid lines in **Figure 5.17c**.
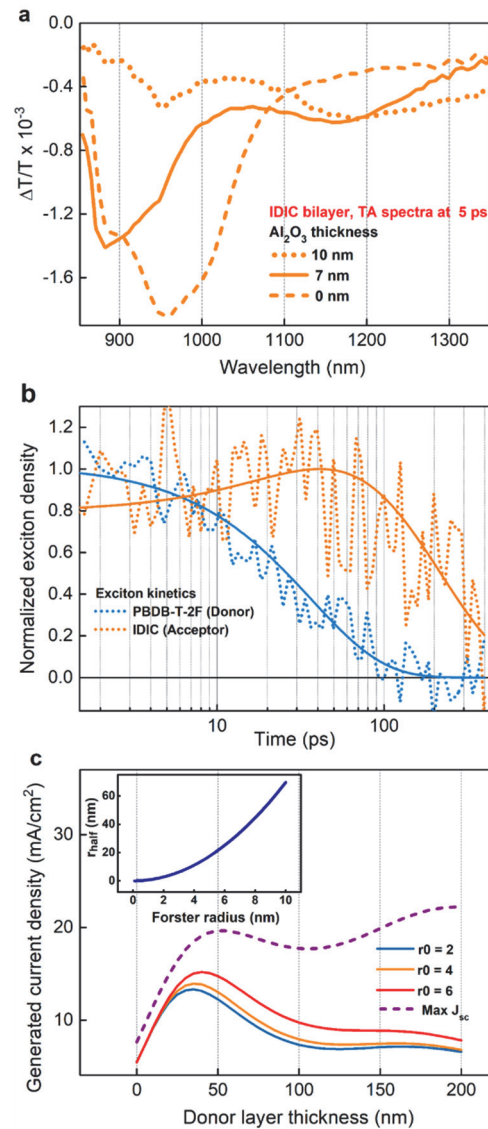
Figure 5. 17. Donor to acceptor layer FRET in bilayer devices. (a) Transient absorption spectra of IDIC bilayers with Al_2O_3 interlayer thicknesses of 10nm, 7 nm and 0 nm, averaged at a time-delay of 5 ps, and (b) Donor exciton kinetics of PBDB-T-2F (dashed blue line), and acceptor photoexcitation kinetics of IDIC (dashed orange), for a bilayer with a 7 nm thick interlayer. Solid lines show simulated kinetics based on exciton diffusion and long-range donor to acceptor FRET. (c) Inset: Relationship between dipole-dipole Forster radius, R_0, to 'slab-to-slab' radius, $R_{1/2}$, the distance at which there is a 50% chance for energy transfer from a donor layer to an acceptor layer. As R_0 increases, $R_{1/2}$ increases quadratically Main: Simulated maximum short circuit photocurrent for a PBDBT-2F/ITIC-Th bilayer, using measured optical values of n and k, for an ITIC-Th acceptor layer thickness of 30 nm, and varying the donor PBDBT-2F thickness. The dashed curve is the maximum J_{sc} with no exciton or charge recombination. The solid curves show the J_{sc} obtained when exciton diffusion is included, using exciton diffusion lengths measured from transient absorption, and showing the effect of larger donor-to acceptor FRET radii on generated current.
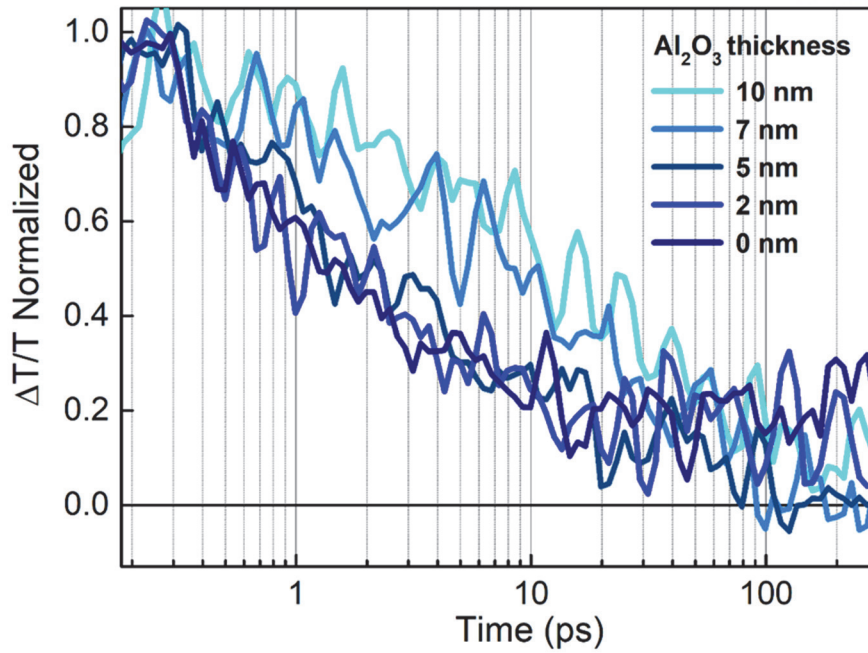
Figure 5. 18. Donor exciton quenching in bilayers with varying interlayer thickness. Donor exciton quenching in PBDB-T-2F/IDIC bilayer series with varying Al_2O_3 interlayer thickness. Here, all the films were excited with 562 nm pump pulses at a fluence of 2.47 µJ/cm². The kinetic traces are obtained by integrating the corresponding spectra at 0.95 eV.

Discussion

In light of the new properties outlined above (high acceptor absorption coefficients and molecular densities, large donor/acceptor spectral overlaps, and true slab-to-slab architecture) it is worth re-presenting the high potential of FRET as a means for efficient exciton harvesting. For a donor exciton in a bilayer configuration device, the distance, $R_{1/2}$, at which there is a 50% probability of undergoing FRET to the acceptor layer is approximately given by,

$$R_{\frac{1}{2}} = \left(\frac{\pi C_a}{6} \right)^{\frac{1}{3}} R_0{}^2 \qquad (5\text{-}1)$$

where, R_0, is the standard point-to-point Förster radius, and C_a is the acceptor layer molecular density. As illustrated in the inset of **Figure 5.18c**, this non-linear dependence means that even small increases in R_0 will result in large increases in $R_{1/2}$. For instance, with our materials, an R_0 of 5 nm will give

93

an $R_{1/2}$ of 20 nm - a substantial portion of the depth of our bilayer devices due to their high absorption coefficients.

As a final rationalisation of our exceptional bilayer device efficiencies, and to show the significant effect of D-A FRET, we combine our exciton diffusion model with a full treatment of the optical cavity effects present in our devices, based on their optical constants.[169] The dashed curve in **Figure 5c** shows the predicted short circuit current, J_{SC}, of a PBDB-T-2F/ITIC-Th1 bilayer device under AM1.5 illumination for a range of donor layer thicknesses, with the acceptor layer thickness held constant at 35 nm, assuming no exciton or charge recombination (i.e. 100% internal quantum efficiency - IQE). The solid curves show the predicted short circuit currents versus donor layer thicknesses when exciton recombination is included, using our measured diffusion lengths and assuming charge separation occurs at all three active layer interfaces (as illustrated in **Figure 5.1c**).

The optimal donor layer thickness from this model agrees well with the experimentally gathered thickness for peak device efficiency (**Table 5.1**). We can see, also, from this figure the large effect on device current that varying the D-A FRET radius can achieve. Specifically, the D-A FRET enables a thicker donor layer for enhanced light absorption.

Encouragingly, the predicted short circuit current from this model, and the measured J_{SC} from the best performing device, match well with each other, which is consistent with our electronic measurements of minimal bimolecular charge recombination. Reduced bimolecular charge recombination is a key advantage of the bilayer solar cell architecture over the bulk heterojunction. Already for the case of PBDB-T-2F/IDICO2 bilayer, we see improved performance in the bilayer configuration compared to the bulk heterojunction, further confirming this approach (**Figure 5.11**). In a well-defined bilayer device in which all important optical and electronic parameters can be independently measured, the ability to explicitly model the photovoltaic response of new materials will be an important benefit of bilayer architectures that could accelerate the design and discovery or more effective materials.

5.4 Conclusion

With these results, we can suggest clear new materials and device design rules, and depart from the complexity of bulk heterojunction OPVs. As illustrated in **Figure 5.1c**, and as shown by our spectroscopic measurements, models, and device efficiencies of 11%, our bilayers benefit from both efficient excitonic transport within the donor and acceptor layers, and significant to acceptor long-range energy transfer between layers. Aiding these processes are strong absorption coefficients in both the donor and acceptor materials, and small levels of non-geminate charge recombination. Combined with a treatment of optical cavity effects, we fully account for the efficient light harvesting within our devices through this combination of short absorption length, large diffusion lengths and donor-to-acceptor FRET.

Paths to future efficiency improvements (without the need to optimise disordered heterojunction morphology) therefore lie in the direction of: increasing intermolecular packing for high absorption coefficients and solubility contrast for bilayer fabrication, maximising exciton diffusion length through decreasing energetic disorder, maximising self-overlap, enhancing radiative lifetimes, and maximising donor to acceptor FRET though increasing donor PL efficiencies, and tuning dipole alignment in both donor and acceptor layers. With an efficient bilayer device in which donor and acceptor components are sequentially deposited, opportunities for interfacial engineering are also vastly improved.

Chapter 6. Summary

In this thesis, charge recombination and transport properties are studied to enhance power conversion efficiency and apply various photovoltaic applications in organic solar cells. Bimolecular recombination in active layer is successfully suppressed by effective non-halogenated solvent processing additives, diphenyl ether and sulfide. It is investigated that charge carriers are efficiently transported even in low light intensity by using compact molecular packing structured polymer. Furthermore, by using small Stokes shift non-fullerene acceptors which have long exciton diffusion lengths by self-energy transfer, high power conversion efficiency over 9% is achieved with suppressed monomolecular (dominantly, exciton) recombination and bimolecular recombination.

In chapter 2 and 3, a widely beneficial and non-halogenated solvent processing additive effects are investigated with various conjugated polymers. To optimize performances of polymer solar cells (PSCs), various techniques have been developed and reported from research fields. Introduction of processing additives in polymer:PCBM bulk-heterojunction solution is one of the efficient strategy to improve the cell performances. Although many solvents have been presented as processing additives, an appropriate processing additive is always different to each polymer solar cell. In this manuscript, we demonstrate diphenyl ether (DPE) works as a widely beneficial processing additive which provides high-performance polymer solar cells to all kinds of photovoltaic polymers. DPE acts like theta solvent to photovoltaic polymers, helps to form ideal bulk-heterojunction film morphologies and suppress bimolecular charge recombination. Furthermore, we have fabricated PSCs and investigated photovoltaic device characteristics using the series of non-halogenated, diphenyl-chalcogenide solvent additives; DPE, diphenyl sulfide (DPS) and diphenyl selenide (DPSe). DPS devices showed optimal power conversion efficiencies (PCEs) of up to 9.08%, and DPE devices also showed similarly high PCEs of up to 8.85%. In contrast, DPSe devices showed relatively low PCEs (5.45% at best) which we attribute to significant surface recombination and high series resistance, which led to limited open-circuit voltage. In the case of DPS, fast, field-independent photocurrent saturation with negligible bimolecular recombination led to efficient charge separation and collection, which resulted in the highest PCEs. Additionally, using 1,2,4-trimethylbenzene and DPS as an entirely non-halogenated solvent / additive system, we successfully demonstrated device fabrication with comparably high PCEs of up to 8.4%. From these works, I suggested efficient way to optimize device performance by using DPE regardless of photovoltaic polymers, and DPS is also effective as non-halogenated solvent additive from further study of diphenyl-chalcogenides.

In chapter 4, photovoltaic characteristics are studied under various light intensities with three semi-crystalline polymers (PTTBT$_{BO}$, PDTBT$_{BO}$, and P2FDTBT$_{BO}$) by modulating the intra- and intermolecular noncovalent coulombic interactions. Low series (R_s) and high shunt (R_{sh}) resistances are essential prerequisites for good device properties under standard illumination (100 mW cm^{-2}).

Considering these factors, among three polymers PDTBT$_{BO}$ polymer solar cells (PSCs) exhibited the most desirable characteristics, with peak power conversion efficiencies (PCE) of 7.52% and 9.60% by blending with PC$_{71}$BM under standard and dim light (2.5 mW cm^{-2}), respectively. P2FDTBT$_{BO}$ PSCs exhibited a low PCE of 3.69% under standard light due to significant charge recombination with high R_s (9.42 Ω cm^2). However the PCE was remarkably improved by 2.3 times (8.33% PCE) under dim light, showing negligible decrease in open-circuit voltage and remarkable increase in fill factor, which is due to an exceptionally high R_{sh} of over 1000 kΩ cm^2. R_s is less significant under dim light, because the generated current is too small to cause noticeable R_s–induced voltage losses. Instead, high R_{sh} becomes more important to avoid leakage currents. This work may provide important tips to further optimize PSCs for indoor applications with low-power electronic devices such as Internet of Things (IoT) sensors, etc.

In chapter 5, by pairing the donor polymer PBDB-T-2F with a range of fused-ring electron acceptors, efficient bilayer organic solar cells (OSCs) are enabled by the combination of high molecular packing densities and absorption coefficients, long exciton diffusion lengths, and efficient, resonant, long-range energy transfer between donor and acceptor layers. Conventional bulk-heterojunction organic solar cells (BHJ OSCs) generally guarantee high power conversion efficiency (PCE), but poor reproducibility of active layer's morphologies and complicated device optimization processes limit further commercialization. I demonstrated efficient bilayer-heterojunction OSCs with a simple strategy to introduce small Stokes shift non-fullerene acceptors which has long exciton diffusion length (L_D) by self-FRET. ITIC-Th1, IDIC and its derivatives (small Stoke shift 38~74 nm) provides 9-11% PCEs in bilayer-heterojunction OSCs with high fill factor ~0.70 which are very similar with BHJ OSCs with the same active layer materials. On the other hand, large Stokes shift materials (133 nm) showed poor PCEs ~ 2.5% due to relatively short L_Ds. Monomolecular recombination was negligible when small Stokes shift materials are used as acceptor, whereas the monomolecular recombination was significant when large Stokes shift materials are used. Furthermore, significant spectral overlap between PL of donor and absorption of acceptor also enables efficient exciton diffusion even in bilayer devices. This work suggest that small Stokes shift materials have a great potential for high-performance bilayer-heterojunction OSCs with long L_Ds.

References

1. Tang, C. W., Two-layer organic photovoltaic cell. *Appl. Phys. Lett.s* **1986,** *48* (2), 183-185.

2. Kraabel, B.; Lee, C. H.; McBranch, D.; Moses, D.; Sariciftci, N. S.; Heeger, A. J., Ultrafast Photoinduced Electron Transfer in Conducting Polymer—Buckminsterfullerene Composites. *Chem. Phys. Lett.* **1993,** *213* (3), 389-394.

3. Sariciftci, N. S.; Smilowitz, L.; Heeger, A. J.; Wudl, F., Photoinduced Electron Transfer from a Conducting Polymer to Buckminsterfullerene. *Science* **1992,** *258* (5087), 1474-1476.

4. Halls, J. J. M.; Walsh, C. A.; Greenham, N. C.; Marseglia, E. A.; Friend, R. H.; Moratti, S. C.; Holmes, A. B., Efficient Photodiodes from Interpenetrating Polymer Networks. *Nat.* **1995,** *376* (6540), 498-500.

5. Yu, G.; Gao, J.; Hummelen, J. C.; Wudl, F.; Heeger, A. J., Polymer Photovoltaic Cells: Enhanced Efficiencies via a Network of Internal Donor-Acceptor Heterojunctions. *Science* **1995,** *270* (5243), 1789.

6. Shaheen, S. E.; Brabec, C. J.; Sariciftci, N. S.; Padinger, F.; Fromherz, T.; Hummelen, J. C., 2.5% Efficient Organic Plastic Solar Cells. *Appl. Phys. Lett.s* **2001,** *78* (6), 841-843.

7. Lee, J. K.; Ma, W. L.; Brabec, C. J.; Yuen, J.; Moon, J. S.; Kim, J. Y.; Lee, K.; Bazan, G. C.; Heeger, A. J., Processing Additives for Improved Efficiency from Bulk Heterojunction Solar Cells. *J. Am. Chem. Soc.* **2008,** *130* (11), 3619-3623.

8. Peet, J.; Kim, J. Y.; Coates, N. E.; Ma, W. L.; Moses, D.; Heeger, A. J.; Bazan, G. C., Efficiency Enhancement in Low-Bandgap Polymer Solar Cells by Processing with Alkane Dithiols. *Nat. Mater.* **2007,** *6* (7), 497-500.

9. Kim, J. Y.; Kim, S. H.; Lee, H.-H.; Lee, K.; Ma, W.; Gong, X.; Heeger, A. J., New Architecture for High-Efficiency Polymer Photovoltaic Cells Using Solution-Based Titanium Oxide as an Optical Spacer. *Adv. Mater.* **2006,** *18* (5), 572-576.

10. Kim, J. Y.; Lee, K.; Coates, N. E.; Moses, D.; Nguyen, T.-Q.; Dante, M.; Heeger, A. J., Efficient Tandem Polymer Solar Cells Fabricated by All-Solution Processing. *Science* **2007,** *317* (5835), 222.

11. Lee, T. H.; Uddin, M. A.; Zhong, C.; Ko, S.-J.; Walker, B.; Kim, T.; Yoon, Y. J.; Park, S. Y.; Heeger, A. J.; Woo, H. Y.; Kim, J. Y., Investigation of Charge Carrier Behavior in High Performance Ternary Blend Polymer Solar Cells. *Adv. Energy Mater.* **2016,** *6* (19), 1600637.

12. Lu, L.; Xu, T.; Chen, W.; Landry, E. S.; Yu, L., Ternary blend polymer solar cells with enhanced power conversion efficiency. *Nat. Photonics* **2014,** *8*, 716.

13. Li, K.; Wu, Y.; Tang, Y.; Pan, M.-A.; Ma, W.; Fu, H.; Zhan, C.; Yao, J., Ternary Blended Fullerene-Free Polymer Solar Cells with 16.5% Efficiency Enabled with a Higher-LUMO-Level

Acceptor to Improve Film Morphology. *Adv. Energy Mater.* **2019,** *9* (33), 1901728.

14. Yuan, J.; Zhang, Y.; Zhou, L.; Zhang, G.; Yip, H.-L.; Lau, T.-K.; Lu, X.; Zhu, C.; Peng, H.; Johnson, P. A.; Leclerc, M.; Cao, Y.; Ulanski, J.; Li, Y.; Zou, Y., Single-Junction Organic Solar Cell with over 15% Efficiency Using Fused-Ring Acceptor with Electron-Deficient Core. *Joule* **2019,** *3* (4), 1140-1151.

15. Blom, P. W. M.; Mihailetchi, V. D.; Koster, L. J. A.; Markov, D. E., Device Physics of Polymer:Fullerene Bulk Heterojunction Solar Cells. *Adv. Mater.* **2007,** *19* (12), 1551-1566.

16. Choi, H.; Ko, S.-J.; Kim, T.; Morin, P.-O.; Walker, B.; Lee, B. H.; Leclerc, M.; Kim, J. Y.; Heeger, A. J., Small-Bandgap Polymer Solar Cells with Unprecedented Short-Circuit Current Density and High Fill Factor. *Adv. Mater.* **2015,** *27* (21), 3318-3324.

17. Choi, H.; Ko, S.-J.; Choi, Y.; Joo, P.; Kim, T.; Lee, B. R.; Jung, J.-W.; Choi, H. J.; Cha, M.; Jeong, J.-R.; Hwang, I.-W.; Song, M. H.; Kim, B.-S.; Kim, J. Y., Versatile Surface Plasmon Resonance of Carbon-Dot-Supported Silver Nanoparticles in Polymer Optoelectronic Devices. *Nat. Photonics* **2013,** *7*, 732.

18. Kim, T.; Kang, S.; Heo, J.; Cho, S.; Kim, J. W.; Choe, A.; Walker, B.; Shanker, R.; Ko, H.; Kim, J. Y., Nanoparticle-Enhanced Silver-Nanowire Plasmonic Electrodes for High-Performance Organic Optoelectronic Devices. *Adv. Mater.* **2018,** *30* (28), 1800659.

19. Ko, S.-J.; Choi, H.; Lee, W.; Kim, T.; Lee, B. R.; Jung, J.-W.; Jeong, J.-R.; Song, M. H.; Lee, J. C.; Woo, H. Y.; Kim, J. Y., Highly Efficient Plasmonic Organic Optoelectronic Devices based on a Conducting Polymer Electrode Incorporated with Silver Nanoparticles. *Energy Environ. Sci.* **2013,** *6* (6), 1949-1955.

20. Lee, T. H.; Park, S. Y.; Walker, B.; Ko, S.-J.; Heo, J.; Woo, H. Y.; Choi, H.; Kim, J. Y., A Universal Processing Additive for High-Performance Polymer Solar Cells. *RSC Adv.* **2017,** *7* (13), 7476-7482.

21. Park, S. Y.; Song, S.; Yoon, Y. J.; Lee, T. H.; An, N. G.; Walker, B.; Kim, J. Y., Non-Halogenated Diphenyl-Chalcogenide Solvent Processing Additives for High-Performance Polymer Bulk-Heterojunction Solar Cells. *RSC Adv.* **2018,** *8* (69), 39777-39783.

22. Elumalai, N. K.; Uddin, A., Open Circuit Voltage of Organic Solar Cells: An In-Depth Review. *Energy Environ. Sci.* **2016,** *9* (2), 391-410.

23. Deibel, C.; Strobel, T.; Dyakonov, V., Role of the Charge Transfer State in Organic Donor–Acceptor Solar Cells. *Adv. Mater.* **2010,** *22* (37), 4097-4111.

24.   Zusan, A.; Vandewal, K.; Allendorf, B.; Hansen, N. H.; Pflaum, J.; Salleo, A.; Dyakonov, V.; Deibel, C., The Crucial Influence of Fullerene Phases on Photogeneration in Organic Bulk Heterojunction Solar Cells. *Adv. Energy Mater.* **2014,** *4* (17), 1400922.

25.   Liu, Y.; Zojer, K.; Lassen, B.; Kjelstrup-Hansen, J.; Rubahn, H.-G.; Madsen, M., Role of the Charge-Transfer State in Reduced Langevin Recombination in Organic Solar Cells: A Theoretical Study. *J. Phys. Chem. C* **2015,** *119* (47), 26588-26597.

26.   Ross, R. T., Some Thermodynamics of Photochemical Systems. *J. Chem. Phys.* **1967,** *46* (12), 4590-4593.

27.   Sokel, R.; Hughes, R. C., Numerical Analysis of Transient Photoconductivity in Insulators. *J. Appl. Phys.* **1982,** *53* (11), 7414-7424.

28.   Kim, J. Y.; Kim, S. H.; Lee, H. H.; Lee, K.; Ma, W.; Gong, X.; Heeger, A. J., New Architecture for High-Efficiency Polymer Photovoltaic Cells Using Solution-Based Titanium Oxide as an Optical Spacer. *Adv. Mater.* **2006,** *18* (5), 572-576.

29.   Kim, J. Y.; Lee, K.; Coates, N. E.; Moses, D.; Nguyen, T. Q.; Dante, M.; Heeger, A. J., Efficient Tandem Polymer Solar Cells Fabricated by All-Solution Processing. *Science* **2007,** *317* (5835), 222-225.

30.   Peet, J.; Kim, J. Y.; Coates, N. E.; Ma, W. L.; Moses, D.; Heeger, A. J.; Bazan, G. C., Efficiency Enhancement in Low-Bandgap Polymer Solar Cells by Processing with Alkane Dithiols. *Nat Mater* **2007,** *6* (7), 497-500.

31.   Liu, Y.; Zhao, J.; Li, Z.; Mu, C.; Ma, W.; Hu, H.; Jiang, K.; Lin, H.; Ade, H.; Yan, H., Aggregation and Morphology Control Enables Multiple Cases of High-Efficiency Polymer Solar Cells. *Nat Commun.* **2014,** *5*, 5293.

32.   Nguyen, T. L.; Choi, H.; Ko, S. J.; Uddin, M. A.; Walker, B.; Yum, S.; Jeong, J. E.; Yun, M. H.; Shin, T. J.; Hwang, S.; Kim, J. Y.; Woo, H. Y., Semi-Crystalline Photovoltaic Polymers with Efficiency Exceeding 9% in a ~300 nm Thick Conventional Single-Cell Device. *Energy Environ. Sci.* **2014,** *7* (9), 3040-3051.

33.   Li, M.; Gao, K.; Wan, X.; Zhang, Q.; Kan, B.; Xia, R.; Liu, F.; Yang, X.; Feng, H.; Ni, W.; Wang, Y.; Peng, J.; Zhang, H.; Liang, Z.; Yip, H.-L.; Peng, X.; Cao, Y.; Chen, Y., Solution-Processed Organic Tandem Solar Cells with Power Conversion Efficiencies >12%. *Nat. Photonics* **2016,** *11*, 85.

34. Wang, Y.; Zhu, H.; Shi, Z.; Wang, F.; Zhang, B.; Dai, S.; Tan, Z. a., Engineering the Vertical Concentration Distribution within the Polymer:Fullerene Blends for High Performance Inverted Polymer Solar Cells. *J. Mater. Chem. A* **2016**.

35. Yu, L.; Li, C.; Li, Q.; Wang, F.; Lin, J.; Liu, J.; Hu, S.; Zheng, H.; Tan, Z. a., Performance Improvement of Conventional and Inverted Polymer Solar Cells with Hydrophobic Fluoropolymer as Nonvolatile Processing Additive. *Org. Electron.* **2015,** *23*, 99-104.

36. Guo, X.; Cui, C.; Zhang, M.; Huo, L.; Huang, Y.; Hou, J.; Li, Y., High Efficiency Polymer Solar Cells Based on Poly(3-hexylthiophene)/Indene-C$_{70}$ Bisadduct with Solvent Additive. *Energy Environ. Sci.* **2012,** *5* (7), 7943.

37. Liu, T.; Huo, L.; Sun, X.; Fan, B.; Cai, Y.; Kim, T.; Kim, J. Y.; Choi, H.; Sun, Y., Ternary Organic Solar Cells Based on Two Highly Efficient Polymer Donors with Enhanced Power Conversion Efficiency. *Adv. Energy Mater.* **2016**, 6, 1502109.

38. Lu, L.; Chen, W.; Xu, T.; Yu, L., High-Performance Ternary Blend Polymer Solar Cells Involving Both Energy Transfer and Hole Relay Processes. *Nat Commun.* **2015,** *6*.

39. Uddin, M. A.; Kim, Y.; Younts, R.; Lee, W.; Gautam, B.; Choi, J.; Wang, C.; Gundogdu, K.; Kim, B. J.; Woo, H. Y., Controlling Energy Levels and Blend Morphology for All-Polymer Solar Cells via Fluorination of a Naphthalene Diimide-Based Copolymer Acceptor. *Macromolecules* **2016,** *49* (17), 6374-6383.

40. Choi, H.; Lee, J.; Lee, W.; Ko, S.-J.; Yang, R.; Lee, J. C.; Woo, H. Y.; Yang, C.; Kim, J. Y., Acid-Functionalized Fullerenes Used as Interfacial Layer Materials in Inverted Polymer Solar Cells. *Org. Electron.* **2013,** *14* (11), 3138-3145.

41. Dou, L.; Gao, J.; Richard, E.; You, J.; Chen, C.-C.; Cha, K. C.; He, Y.; Li, G.; Yang, Y., Systematic Investigation of Benzodithiophene- and Diketopyrrolopyrrole-Based Low-Bandgap Polymers Designed for Single Junction and Tandem Polymer Solar Cells. *J. Am. Chem. Soc.* **2012,** *134* (24), 10071-10079.

42. Yip, H.-L.; Jen, A. K. Y., Recent Advances in Solution-Processed Interfacial Materials for Efficient and Stable Polymer Solar Cells. *Energy Environ. Sci.* **2012,** *5* (3), 5994-6011.

43. Yusoff, A. R. b. M.; Kim, D.; Kim, H. P.; Shneider, F. K.; da Silva, W. J.; Jang, J., A High Efficiency Solution Processed Polymer Inverted Triple-Junction Solar Cell Exhibiting a Power Conversion Efficiency of 11.83%. *Energy Environ. Sci.* **2015,** *8* (1), 303-316.

44.   Zhang, J.; Zhang, Y.; Fang, J.; Lu, K.; Wang, Z.; Ma, W.; Wei, Z., Conjugated Polymer-Small Molecule Alloy Leads to High Efficient Ternary Organic Solar Cells. *J. Am. Chem. Soc.* **2015,** *137* (25), 8176-83.

45.   Erb, T.; Zhokhavets, U.; Gobsch, G.; Raleva, S.; Stühn, B.; Schilinsky, P.; Waldauf, C.; Brabec, C. J., Correlation Between Structural and Optical Properties of Composite Polymer/Fullerene Films for Organic Solar Cells. *Adv. Funct. Mater.* **2005,** *15* (7), 1193-1196.

46.   Li, G.; Shrotriya, V.; Yao, Y.; Yang, Y., Investigation of Annealing Effects and Film Thickness Dependence of Polymer Solar Cells Based on Poly(3-hexylthiophene). *J. Appl. Phys.* **2005,** *98* (4), 43704-43704.

47.   Li, G.; Yao, Y.; Yang, H.; Shrotriya, V.; Yang, G.; Yang, Y., "Solvent Annealing" Effect in Polymer Solar Cells Based on Poly(3-hexylthiophene) and Methanofullerenes. *Adv. Funct. Mater.* **2007,** *17* (10), 1636-1644.

48.   Verploegen, E.; Miller, C. E.; Schmidt, K.; Bao, Z.; Toney, M. F., Manipulating the Morphology of P3HT–PCBM Bulk Heterojunction Blends with Solvent Vapor Annealing. *Chem. Mater.* **2012,** *24* (20), 3923-3931.

49.   Chambon, S.; Mens, R.; Vandewal, K.; Clodic, E.; Scharber, M.; Lutsen, L.; Gelan, J.; Manca, J.; Vanderzande, D.; Adriaensens, P., Influence of Octanedithiol on the Nanomorphology of PCPDTBT:PCBM Blends Studied by Solid-State NMR. *Sol. Energy Mater. Sol. Cells* **2012,** *96*, 210-217.

50.   Lee, C.-Y.; Kim, B.; Kim, K. H.; Yoon, Y.; Lee, M. W.; Choi, D. H.; Ko, M. J.; Kim, H.; Lee, D.-K.; Kim, K., Synthesis and characterization of Wide Range Light Absorbing Poly(dithieno[3,2-b:2′,3′-d]thiophene-alt-3,6-bis(thiophen-2-yl)-2,5-di-n-octyl-pyrrolo[3,4-c]pyrrole-1,4-dione) for Polymer Solar Cells. *Synth. Met.* **2013,** *164*, 64-68.

51.   Park, K. H.; Kim, Y. J.; Lee, G. B.; An, T. K.; Park, C. E.; Kwon, S.-K.; Kim, Y.-H., Recently Advanced Polymer Materials Containing Dithieno[3,2-b:2′,3′-d]phosphole Oxide for Efficient Charge Transfer in High-Performance Solar Cells. *Adv. Funct. Mater.* **2015,** *25* (26), 3991-3997.

52.   Kim, Y.; Hong, J.; Oh, J. H.; Yang, C., Naphthalene Diimide Incorporated Thiophene-Free Copolymers with Acene and Heteroacene Units: Comparison of Geometric Features and Electron-Donating Strength of Co-units. *Chem. Mater.* **2013,** *25* (15), 3251-3259.

53.   Kim, Y.; Yeom, H. R.; Kim, J. Y.; Yang, C., High-efficiency Polymer Solar Cells with a Cost-Effective Quinoxaline Polymer through Nanoscale Morphology Control Induced by Practical Processing Additives. *Energy Environ. Sci.* **2013,** *6* (6), 1909-1916.

54. Kwon, S.; Park, J. K.; Kim, J.; Kim, G.; Yu, K.; Lee, J.; Jo, Y.-R.; Kim, B.-J.; Kang, H.; Kim, J.; Kim, H.; Lee, K., In Situ Studies of the Molecular Packing Dynamics of Bulk-Heterojunction Solar Cells Induced by the Processing Additive 1-Chloronaphthalene. *J. Mater. Chem. A* **2015,** *3* (15), 7719-7726.

55. Yi, C.; Hu, X.; Liu, H. C.; Hu, R.; Hsu, C.-H.; Zheng, J.; Gong, X., Efficient Polymer Solar Cells Fabricated from Solvent Processing Additive Solution. *J. Mater. Chem. C* **2015,** *3* (1), 26-32.

56. He, Z.; Xiao, B.; Liu, F.; Wu, H.; Yang, Y.; Xiao, S.; Wang, C.; Russell, T. P.; Cao, Y., Single-Junction Polymer Solar Cells with High Efficiency and Photovoltage. *Nat. Photon.* **2015,** *9* (3), 174-179.

57. Ho, C. H. Y.; Dong, Q.; Yin, H.; Leung, W. W. K.; Yang, Q.; Lee, H. K. H.; Tsang, S. W.; So, S. K., Impact of Solvent Additive on Carrier Transport in Polymer:Fullerene Bulk Heterojunction Photovoltaic Cells. *Adv. Mater. Interfaces* **2015,** *2* (12), 1500166.

58. Lou, S. J.; Szarko, J. M.; Xu, T.; Yu, L.; Marks, T. J.; Chen, L. X., Effects of Additives on the Morphology of Solution Phase Aggregates Formed by Active Layer Components of High-Efficiency Organic Solar Cells. *J. Am. Chem. Soc.* **2011,** *133* (51), 20661-20663.

59. Ouyang, X.; Peng, R.; Ai, L.; Zhang, X.; Ge, Z., Efficient Polymer Solar Cells Employing a Non-Conjugated Small-Molecule Electrolyte. *Nat Photon* **2015,** *9* (8), 520-524.

60. Uddin, M. A.; Lee, T. H.; Xu, S.; Park, S. Y.; Kim, T.; Song, S.; Nguyen, T. L.; Ko, S.-j.; Hwang, S.; Kim, J. Y.; Woo, H. Y., Interplay of Intramolecular Noncovalent Coulomb Interactions for Semicrystalline Photovoltaic Polymers. *Chem. Mater.* **2015,** *27* (17), 5997-6007.

61. Liu, D.; Wang, Z.; Zhang, S.; Zheng, Z.; Yang, B.; Ma, W.; Hou, J., Rational Selection of Solvents and Fine Tuning of Morphologies toward Highly Efficient Polymer Solar Cells Fabricated Using Green Solvents. *RSC Adv.* **2015,** *5* (85), 69567-69572.

62. Raegen, A.; Chowdhury, M.; Calers, C.; Schmatulla, A.; Steiner, U.; Reiter, G., Aging of Thin Polymer Films Cast from a Near-Theta Solvent. *Phys. Rev. Lett.* **2010,** *105* (22), 227801.

63. Brochard, F.; Degennes, P. G., Dynamical Scaling for Polymers in Theta-Solvents. *Macromolecules* **1977,** *10* (5), 1157-1161.

64. Zhang, H.; Yao, H.; Zhao, W.; Ye, L.; Hou, J., High-Efficiency Polymer Solar Cells Enabled by Environment-Friendly Single-Solvent Processing. *Adv. Energy Mater.* **2016,** *6* (6), 1502177.

65. Koster, L. J. A.; Mihailetchi, V. D.; Xie, H.; Blom, P. W. M., Origin of the Light Intensity Dependence of The Short-Circuit Current of Polymer/Fullerene Solar Cells. *Appl. Phys. Lett.* **2005,** *87* (20), 203502.

66. Kaltenbrunner, M.; White, M. S.; Głowacki, E. D.; Sekitani, T.; Someya, T.; Sariciftci, N. S.; Bauer, S., Ultrathin and Lightweight Organic Solar Cells with High Flexibility. *Nat. Commun.* **2012,** *3*, 770.

67. Krebs, F. C.; Gevorgyan, S. A.; Alstrup, J., A Roll-To-Roll Process to Flexible Polymer Solar Cells: Model Studies, Manufacture and Operational Stability Studies. *J. Mater. Chem.* **2009,** *19* (30), 5442-5451.

68. Fan, Q.; Wang, Y.; Zhang, M.; Wu, B.; Guo, X.; Jiang, Y.; Li, W.; Guo, B.; Ye, C.; Su, W.; Fang, J.; Ou, X.; Liu, F.; Wei, Z.; Sum, T. C.; Russell, T. P.; Li, Y., High-Performance As-Cast Nonfullerene Polymer Solar Cells with Thicker Active Layer and Large Area Exceeding 11% Power Conversion Efficiency. *Adv. Mater.* **2018,** *30* (6), 1704546.

69. Zhao, W.; Qian, D.; Zhang, S.; Li, S.; Inganäs, O.; Gao, F.; Hou, J., Fullerene-Free Polymer Solar Cells with over 11% Efficiency and Excellent Thermal Stability. *Adv. Mater.* **2016,** *28* (23), 4734-4739.

70. Ouyang, X.; Peng, R.; Ai, L.; Zhang, X.; Ge, Z., Efficient Polymer Solar Cells Employing a Non-Conjugated Small-Molecule Electrolyte. *Nat. Photonics* **2015,** *9*, 520.

71. Zhang, K.; Hu, Z.; Xu, R.; Jiang, X. F.; Yip, H. L.; Huang, F.; Cao, Y., High-Performance Polymer Solar Cells with Electrostatic Layer-by-Layer Self-Assembled Conjugated Polyelectrolytes as the Cathode Interlayer. *Adv. Mater.* **2015,** *27* (24), 3607-3613.

72. Liu, Y.; Zhao, J.; Li, Z.; Mu, C.; Ma, W.; Hu, H.; Jiang, K.; Lin, H.; Ade, H.; Yan, H., Aggregation and Morphology Control Enables Multiple Cases of High-Efficiency Polymer Solar Cells. *Nat. Commun.* **2014,** *5*, 5293.

73. Peet, J.; Kim, J. Y.; Coates, N. E.; Ma, W. L.; Moses, D.; Heeger, A. J.; Bazan, G. C., Efficiency Enhancement in Low-Bandgap Polymer Solar Cells by Processing with Alkane Dithiols. *Nat. Mater.* **2007,** *6*, 497.

74. Song, S.; Heo, J.; Lee, T. K.; Park, S.; Walker, B.; Kwak, S. K.; Kim, J. Y., Optically Tunable Plasmonic Two-Dimensional Ag Quantum Dot Arrays for Optimal Light Absorption in Polymer Solar Cells. *J. Phys. Chem. C* **2017,** *121* (33), 17569-17576.

75. Wu, J.-L.; Chen, F.-C.; Hsiao, Y.-S.; Chien, F.-C.; Chen, P.; Kuo, C.-H.; Huang, M. H.; Hsu, C.-S., Surface Plasmonic Effects of Metallic Nanoparticles on the Performance of Polymer Bulk Heterojunction Solar Cells. *ACS Nano* **2011,** *5* (2), 959-967.

76. Xu, B.; Sai-Anand, G.; Gopalan, A.-I.; Qiao, Q.; Kang, S.-W., Improving Photovoltaic Properties of P3HT:IC60BA through the Incorporation of Small Molecules. *Polymers* **2018,** *10* (2), 121.

77. Venkatesan, S.; Chen, J.; Ngo, E. C.; Dubey, A.; Khatiwada, D.; Zhang, C.; Qiao, Q., Critical Role of Domain Crystallinity, Domain Purity and Domain Interface Sharpness for Reduced Bimolecular Recombination in Polymer Solar Cells. *Nano Energy* **2015,** *12*, 457-467.

78. Venkatesan, S.; Adhikari, N.; Chen, J.; Ngo, E. C.; Dubey, A.; Galipeau, D. W.; Qiao, Q., Interplay of Nanoscale Domain Purity and Size on Charge Transport and Recombination Dynamics in Polymer Solar Cells. *Nanoscale* **2014,** *6* (2), 1011-1019.

79. Seongyu, L.; Jaemin, K.; Kwanghee, L., Air-Stable Organic Solar Cells Using an Iodine-Free Solvent Additive. *Adv. Energy Mater.* **2016,** *6* (21), 1600970.

80. Sai-Anand, G.; Dubey, A.; Gopalan, A.-I.; Venkatesan, S.; Ruban, S.; Reza, K. M.; Choi, J.; Lakhi, K. S.; Xu, B.; Qiao, Q.; Vinu, A., Additive Assisted Morphological Optimization of Photoactive Layer in Polymer Solar Cells. *Sol. Energy Mater. Sol. Cells* **2018,** *182*, 246-254.

81. Lee, T. H.; Uddin, M. A.; Zhong, C.; Ko, S. J.; Walker, B.; Kim, T.; Yoon, Y. J.; Park, S. Y.; Heeger, A. J.; Woo, H. Y.; Kim, J. Y., Investigation of Charge Carrier Behavior in High Performance Ternary Blend Polymer Solar Cells. *Adv. Energy Mater.* **2016,** *6* (19), 1600637.

82. Hoven, C. V.; Dang, X. D.; Coffin, R. C.; Peet, J.; Nguyen, T. Q.; Bazan, G. C., Improved Performance of Polymer Bulk Heterojunction Solar Cells Through the Reduction of Phase Separation via Solvent Additives. *Adv. Mater.* **2010,** *22* (8), E63-E66.

83. Zhao, J.; Li, Y.; Yang, G.; Jiang, K.; Lin, H.; Ade, H.; Ma, W.; Yan, H., Efficient Organic Solar Cells Processed from Hydrocarbon Solvents. *Nat. Energy* **2016,** *1* (2), 15027.

84. Zhang, H.; Yao, H.; Zhao, W.; Ye, L.; Hou, J., High-Efficiency Polymer Solar Cells Enabled by Environment-Friendly Single-Solvent Processing. *Adv. Energy Mater.* **2016,** *6* (6), 1502177.

85. Wu, Y.; Zou, Y.; Yang, H.; Li, Y.; Li, H.; Cui, C.; Li, Y., Achieving over 9.8% Efficiency in Nonfullerene Polymer Solar Cells by Environmentally Friendly Solvent Processing. *ACS Appl. Mater. Interfaces* **2017,** *9* (42), 37078-37086.

86. Venkatesan, S.; Chen, Q.; Ngo, E. C.; Adhikari, N.; Nelson, K.; Dubey, A.; Sun, J.; Bommisetty, V.; Zhang, C.; Galipeau, D.; Qiao, Q., Polymer Solar Cells Processed Using Anisole as a Relatively Nontoxic Solvent. *Energy Technology* **2014,** *2* (3), 269-274.

87. Chueh, C.-C.; Yao, K.; Yip, H.-L.; Chang, C.-Y.; Xu, Y.-X.; Chen, K.-S.; Li, C.-Z.; Liu, P.; Huang, F.; Chen, Y.; Chen, W.-C.; Jen, A. K. Y., Non-Halogenated Solvents for Environmentally Friendly Processing of High-Performance Bulk-Heterojunction Polymer Solar Cells. *Energy Environ. Sci.* **2013,** *6* (11), 3241-3248.

88. Ko, S. J.; Walker, B.; Nguyen, T. L.; Choi, H.; Seifter, J.; Uddin, M. A.; Kim, T.; Kim, S.; Heo, J.; Kim, G. H.; Cho, S.; Heeger, A. J.; Woo, H. Y.; Kim, J. Y., Photocurrent Extraction Efficiency near Unity in a Thick Polymer Bulk Heterojunction. *Adv. Funct. Mater.* **2016,** *26* (19), 3324-3330.

89. Zheng, Y.; Goh, T.; Fan, P.; Shi, W.; Yu, J.; Taylor, A. D., Toward Efficient Thick Active PTB7 Photovoltaic Layers Using Diphenyl Ether as a Solvent Additive. *ACS Appl. Mater. Interfaces* **2016,** *8* (24), 15724-15731.

90. Li, Y.; Ko, S.-J.; Park, S. Y.; Choi, H.; Nguyen, T. L.; Uddin, M. A.; Kim, T.; Hwang, S.; Kim, J. Y.; Woo, H. Y., Quinoxaline-Thiophene Based Thick Photovoltaic Devices with an Efficiency of ~8%. *J. Mater. Chem. A* **2016,** *4* (25), 9967-9976.

91. Xia, Y.; Zhang, H.; Li, J.; Tong, J.; Zhang, P.; Yang, C., Synthesis of Dithieno[2,3-d:2',3'-d']benzo[1,2-b:4,5-b']dithiophene-alt-isoindigo Conjugated Polymer and Enhancement of Photovoltaic Property with Diphenyl Sulfide Additives. *J. Polym. Res.* **2014,** *22* (1), 633.

92. Kong, J.; Hwang, I. W.; Lee, K., Top-Down Approach for Nanophase Reconstruction in Bulk Heterojunction Solar Cells. *Adv. Mater.* **2014,** *26* (36), 6275-6283.

93. Zhao, L.; Zhao, S.; Xu, Z.; Yang, Q.; Huang, D.; Xu, X., A Simple Method to Adjust the Morphology of Gradient Three-Dimensional PTB7-Th:PC$_{71}$BM Polymer Solar Cells. *Nanoscale* **2015,** *7* (12), 5537-5544.

94. Kyaw, A. K. K.; Wang, D. H.; Gupta, V.; Leong, W. L.; Ke, L.; Bazan, G. C.; Heeger, A. J., Intensity Dependence of Current–Voltage Characteristics and Recombination in High-Efficiency Solution-Processed Small-Molecule Solar Cells. *ACS Nano* **2013,** *7* (5), 4569-4577.

95. Koster, L. J. A.; Mihailetchi, V. D.; Ramaker, R.; Blom, P. W. M., Light Intensity Dependence of Open-Circuit Voltage of Polymer:Fullerene Solar Cells. *Appl. Phys. Lett.* **2005,** *86* (12), 123509.

96. Brus, V. V., Light Dependent Open-Circuit Voltage of Organic Bulk Heterojunction Solar Cells in the Presence of Surface Recombination. *Org. Electron.* **2016,** *29*, 1-6.

97. Bauer, N.; Zhang, Q.; Zhao, J.; Ye, L.; Kim, J.-H.; Constantinou, I.; Yan, L.; So, F.; Ade, H.; Yan, H.; You, W., Comparing Non-Fullerene Acceptors with Fullerene in Polymer Solar Cells: a Case Study with FTAZ and PyCNTAZ. *J. Mater. Chem. A* **2017,** *5* (10), 4886-4893.

98. Park, S. Y.; Li, Y.; Kim, J.; Lee, T. H.; Walker, B.; Woo, H. Y.; Kim, J. Y., Alkoxybenzothiadiazole-Based Fullerene and Nonfullerene Polymer Solar Cells with High Shunt Resistance for Indoor Photovoltaic Applications. *ACS Appl. Mater. Interfaces* **2018,** *10* (4), 3885-3894.

99. Ye, L.; Jing, Y.; Guo, X.; Sun, H.; Zhang, S.; Zhang, M.; Huo, L.; Hou, J., Remove the Residual Additives toward Enhanced Efficiency with Higher Reproducibility in Polymer Solar Cells. *J. Phys. Chem. C* **2013,** *117* (29), 14920-14928.

100. Armin, A.; Hambsch, M.; Wolfer, P.; Jin, H.; Li, J.; Shi, Z.; Burn, P. L.; Meredith, P., Efficient, Large Area, and Thick Junction Polymer Solar Cells with Balanced Mobilities and Low Defect Densities. *Adv. Energy Mater.* **2015,** *5* (3), 1401221.

101. Roth, B.; dos Reis Benatto, G. A.; Corazza, M.; Søndergaard, R. R.; Gevorgyan, S. A.; Jørgensen, M.; Krebs, F. C., The Critical Choice of PEDOT:PSS Additives for Long Term Stability of Roll-to-Roll Processed OPVs. *Adv. Energy Mater.* **2015,** *5* (9), 1401912.

102. Yao, H.; Ye, L.; Hou, J.; Jang, B.; Han, G.; Cui, Y.; Su, G. M.; Wang, C.; Gao, B.; Yu, R.; Zhang, H.; Yi, Y.; Woo, H. Y.; Ade, H.; Hou, J., Achieving Highly Efficient Nonfullerene Organic Solar Cells with Improved Intermolecular Interaction and Open-Circuit Voltage. *Adv. Mater.* **2017,** *29* (21), 1700254.

103. Yu, R.; Zhang, S.; Yao, H.; Guo, B.; Li, S.; Zhang, H.; Zhang, M.; Hou, J., Two Well-Miscible Acceptors Work as One for Efficient Fullerene-Free Organic Solar Cells. *Adv. Mater.* **2017,** *29* (26), 1700437.

104. Rühle, K.; Juhl, M. K.; Abbott, M. D.; Kasemann, M., Evaluating Crystalline Silicon Solar Cells at Low Light Intensities Using Intensity-Dependent Analysis of I–V Parameters. *IEEE Journal of Photovoltaics* **2015,** *5* (3), 926-931.

105. Reich, N. H.; van Sark, W. G. J. H. M.; Alsema, E. A.; Lof, R. W.; Schropp, R. E. I.; Sinke, W. C.; Turkenburg, W. C., Crystalline Silicon Cell Performance at Low Light Intensities. *Sol. Energy Mater. Sol. Cells* **2009,** *93* (9), 1471-1481.

106. Gorlatova, M.; Kinget, P.; Kymissis, I.; Rubenstein, D.; Wang, X.; Zussman, G., Energy Harvesting Active Networked Tags (Enhants) for Ubiquitous Object Networking. *IEEE Wireless Communications* **2010,** *17* (6), 18-25.

107. Nasiri, A.; Zabalawi, S. A.; Mandic, G., Indoor Power Harvesting Using Photovoltaic Cells for Low-Power Applications. *IEEE Transactions on Industrial Electronics* **2009,** *56* (11), 4502-4509.

108. Steim, R.; Ameri, T.; Schilinsky, P.; Waldauf, C.; Dennler, G.; Scharber, M.; Brabec, C. J., Organic photovoltaics for low light applications. *Sol. Energy Mater. Sol. Cells* **2011,** *95* (12), 3256-3261.

109. Lee, H. K. H.; Li, Z.; Durrant, J. R.; Tsoi, W. C., Is Organic Photovoltaics Promising for Indoor Applications? *Appl. Phys. Lett.* **2016,** *108* (25), 253301.

110. Ko, S.-J.; Hoang, Q. V.; Song, C. E.; Uddin, M. A.; Lim, E.; Park, S. Y.; Lee, B. H.; Song, S.; Moon, S.-J.; Hwang, S.; Morin, P.-O.; Leclerc, M.; Su, G. M.; Chabinyc, M. L.; Woo, H. Y.; Shin, W. S.; Kim, J. Y., High-Efficiency Photovoltaic Cells with Wide Optical Band Gap Polymers Based on Fluorinated Phenylene-Alkoxybenzothiadiazole. *Energy Environ. Sci.* **2017,** *10* (6), 1443-1455.

111. Lee, W.; Kim, G.-H.; Ko, S.-J.; Yum, S.; Hwang, S.; Cho, S.; Shin, Y.-H.; Kim, J. Y.; Woo, H. Y., Semicrystalline D–A Copolymers with Different Chain Curvature for Applications in Polymer Optoelectronic Devices. *Macromolecules* **2014,** *47* (5), 1604-1612.

112. Li, Y.; Lee, T. H.; Park, S. Y.; Uddin, M. A.; Kim, T.; Hwang, S.; Kim, J. Y.; Woo, H. Y., Straight Chain D–A Copolymers Based on Thienothiophene and Benzothiadiazole for Efficient Polymer Field Effect Transistors and Photovoltaic Cells. *Polym. Chem.* **2016,** *7* (28), 4638-4646.

113. Ko, S.-J.; Walker, B.; Nguyen, T. L.; Choi, H.; Seifter, J.; Uddin, M. A.; Kim, T.; Kim, S.; Heo, J.; Kim, G.-H.; Cho, S.; Heeger, A. J.; Woo, H. Y.; Kim, J. Y., Photocurrent Extraction Efficiency near Unity in a Thick Polymer Bulk Heterojunction. *Adv. Funct. Mater.* **2016,** *26* (19), 3324-3330.

114. Li, S.; Ye, L.; Zhao, W.; Zhang, S.; Mukherjee, S.; Ade, H.; Hou, J., Energy-Level Modulation of Small-Molecule Electron Acceptors to Achieve over 12% Efficiency in Polymer Solar Cells. *Adv. Mater.* **2016,** *28* (42), 9423-9429.

115. Zhao, W.; Qian, D.; Zhang, S.; Li, S.; Inganäs, O.; Gao, F.; Hou, J., Fullerene-Free Polymer Solar Cells with over 11% Efficiency and Excellent Thermal Stability. *Adv. Mater.* **2016,** *28* (23), 4734-4739.

116. Kim, G.; Song, S.; Lee, J.; Kim, T.; Lee, T. H.; Walker, B.; Kim, J. Y.; Yang, C., Control of Charge Dynamics via Use of Nonionic Phosphonate Chains and Their Effectiveness for Inverted Structure Solar Cells. *Adv. Energy Mater.* **2015,** *5* (18), 1500844.

117. Dacuña, J.; Salleo, A., Modeling Space-Charge-Limited Currents in Organic Semiconductors: Extracting Trap Density and Mobility. *Phys. Rev. B* **2011,** *84* (19), 195209.

118.   Shi, D.; Adinolfi, V.; Comin, R.; Yuan, M.; Alarousu, E.; Buin, A.; Chen, Y.; Hoogland, S.; Rothenberger, A.; Katsiev, K.; Losovyj, Y.; Zhang, X.; Dowben, P. A.; Mohammed, O. F.; Sargent, E. H.; Bakr, O. M., Low Trap-State Density and Long Carrier Diffusion in Organolead Trihalide Perovskite Single Crystals. *Science* **2015,** *347* (6221), 519-522.

119.   Ripolles, T. S.; Guerrero, A.; Garcia-Belmonte, G., Polymer Defect States Modulate Open-Circuit Voltage in Bulk-Heterojunction Solar Cells. *Appl. Phys. Lett.* **2013,** *103* (24), 243306.

120.   Karak, S.; Homnick, P. J.; Della Pelle, A. M.; Bae, Y.; Duzhko, V. V.; Liu, F.; Russell, T. P.; Lahti, P. M.; Thayumanavan, S., Crystallinity and Morphology Effects on a Solvent-Processed Solar Cell Using a Triarylamine-Substituted Squaraine. *ACS Appl. Mater. Interfaces* **2014,** *6* (14), 11376-11384.

121.   Mayer, A. C.; Lloyd, M. T.; Herman, D. J.; Kasen, T. G.; Malliaras, G. G., Postfabrication Annealing of Pentacene-Based Photovoltaic Cells. *Appl. Phys. Lett.* **2004,** *85* (25), 6272-6274.

122.   Guo, B.; Zhou, W.; Wu, M.; Lv, J.; Yu, C.; Li, F.; Hu, Z., Improving the Efficiency of Polymer Solar Cells via a Treatment of Methanol : Water on the Active Layers. *J. Mater. Chem. A* **2016,** *4* (24), 9644-9652.

123.   Menke, S. M.; Holmes, R. J., Exciton Diffusion in Organic Photovoltaic Cells. *Energy Environ. Sci.* **2014,** 7, 499-512.

124.   Mikhnenko, O. V.; Blom, P. W. M.; Nguyen, T.-Q., Exciton Diffusion in Organic Semiconductors. *Energy Environ. Sci.* **2015,** *8* (7), 1867-1888.

125.   Erb, T.; Zhokhavets, U.; Gobsch, G.; Raleva, S.; Stühn, B.; Schilinsky, P.; Waldauf, C.; Brabec, C. J., Correlation between Structural and Optical Properties of Composite Polymer/Fullerene Films for Organic Solar Cells. *Adv. Funct. Mater.* **2005**, 15, 1193-1196.

126.   Walker, B.; Tamayo, A. B.; Dang, X. D.; Zalar, P.; Seo, J. H.; Garcia, A.; Tantiwiwat, M.; Nguyen, T. Q., Nanoscale Phase Separation and High Photovoltaic Efficiency in Solution-Processed, Small-Molecule Bulk Heterojunction Solar Cells. *Adv. Funct. Mater.* **2009**, 19, 3065-3069.

127.   Yu, G.; Gao, J.; Hummelen, J. C.; Wudl, F.; Heeger, A. J., Polymer Photovoltaic Cells: Enhanced Efficiencies via a Network of Internal Donor-Acceptor Heterojunctions. *Science* **1995**, *270* (5243), 1789-1791.

128.   Campbell, A. R.; Hodgkiss, J. M.; Westenhoff, S.; Howard, I. A.; Marsh, R. A.; McNeill, C. R.; Friend, R. H.; Greenham, N. C., Low-Temperature Control of Nanoscale Morphology for High Performance Polymer Photovoltaics. *Nano Lett.* **2008,** *8* (11), 3942-3947.

129. Dang, M. T.; Hirsch, L.; Wantz, G., P3HT:PCBM, Best Seller in Polymer Photovoltaic Research. *Adv. Mater.* **2011**, 23, 3597-3602.

130. Li, Y.; Ko, S.-J.; Park, S. Y.; Choi, H.; Nguyen, T. L.; Uddin, M. A.; Kim, T.; Hwang, S.; Kim, J. Y.; Woo, H. Y., Quinoxaline–Thiophene Based Thick Photovoltaic Devices with an Efficiency of ~8%. *J. Mater. Chem. A* **2016,** *4* (25), 9967-9976.

131. Sun, Y.; Welch, G. C.; Leong, W. L.; Takacs, C. J.; Bazan, G. C.; Heeger, A. J., Solution-Processed Small-Molecule Solar Cells with 6.7% Efficiency. *Nat. Mater.* **2011,** *11*, 44-44.

132. Lee, T. H.; Choi, H.; Walker, B.; Kim, T.; Kim, H.-B.; Kim, J. Y., Replacing the Metal Oxide Layer with a Polymer Surface Modifier for High-Performance Inverted Polymer Solar Cells. *RSC Adv.* **2014,** *4* (9), 4791-4795.

133. Walker, B.; Choi, H.; Kim, J. Y., Interfacial Engineering for Highly Efficient Organic Solar Cells. *Curr. Appl. Phys.* **2017,** *17* (3), 370-391.

134. Jackson, N. E.; Savoie, B. M.; Marks, T. J.; Chen, L. X.; Ratner, M. A., The Next Breakthrough for Organic Photovoltaics? *J. Phys. Chem. Lett.* **2015,** *6* (1), 77-84.

135. Xiao, F.; Li, C.; Sun, J.; Zhang, L., Knowledge Domain and Emerging Trends in Organic Photovoltaic Technology: a Scientometric Review Based on Citespace Analysis. *Front. Chem.***2017,** *5*, 1-12.

136. Sánchez-Díaz, A.; Burtone, L.; Riede, M.; Palomares, E., Measurements of Efficiency Losses in Blend and Bilayer-Type Zinc Phthalocyanine/C_{60} High-Vacuum-Processed Organic Solar Cells. *J. Phys. Chem. C* **2012,** *116* (31), 16384-16390.

137. Lin, C. F.; Nichols, V. M.; Cheng, Y. C.; Bardeen, C. J.; Wei, M. K.; Liu, S. W.; Lee, C. C.; Su, W. C.; Chiu, T. L.; Han, H. C.; Chen, L. C.; Chen, C. T.; Lee, J. H., Chloroboron Subphthalocyanine/C_{60} Planar Heterojunction Organic Solar Cell with N,N-Dicarbazolyl-3,5-Benzene Blocking Layer. *Sol. Energy Mater. Sol. Cells* **2014,** *122*, 264-270.

138. Lee, K. H.; Schwenn, P. E.; Smith, A. R. G.; Cavaye, H.; Shaw, P. E.; James, M.; Krueger, K. B.; Gentle, I. R.; Meredith, P.; Burn, P. L., Morphology of All-Solution-Processed "Bilayer" Organic Solar Cells. *Adv. Mater.* **2011**, 23, 766-770.

139. Cui, Y.; Zhang, S.; Liang, N.; Kong, J.; Yang, C.; Yao, H.; Ma, L.; Hou, J., Toward Efficient Polymer Solar Cells Processed by a Solution-Processed Layer-By-Layer Approach. *Adv. Mater.* **2018,** *30* (34), 1802499.

140. Sun, R.; Guo, J.; Sun, C.; Wang, T.; Luo, Z.; Zhang, Z.; Jiao, X.; Tang, W.; Yang, C.; Li, Y.; Min, J., A Universal Layer-By-Layer Solution-Processing Approach for Efficient Non-Fullerene Organic Solar Cells. *Energy Environ. Sci.* **2019,** *12* (1), 384-395.

141. Dong, S.; Zhang, K.; Xie, B.; Xiao, J.; Yip, H. L.; Yan, H.; Huang, F.; Cao, Y., High-Performance Large-Area Organic Solar Cells Enabled by Sequential Bilayer Processing via Nonhalogenated Solvents. *Adv. Energy Mater.* **2019,** *9* (1), 1-7.

142. Lin, Y.; He, Q.; Zhao, F.; Huo, L.; Mai, J.; Lu, X.; Su, C. J.; Li, T.; Wang, J.; Zhu, J.; Sun, Y.; Wang, C.; Zhan, X., A Facile Planar Fused-Ring Electron Acceptor for As-Cast Polymer Solar Cells with 8.71% Efficiency. *J. Am. Chem. Soc.* **2016**, *138* (9), 2973-2976.

143. Lin, Y.; Wang, J.; Zhang, Z. G.; Bai, H.; Li, Y.; Zhu, D.; Zhan, X., An Electron Acceptor Challenging Fullerenes for Efficient Polymer Solar Cells. *Adv. Mater.* **2015,** 27, 1170-1174.

144. Lin, Y.; Zhao, F.; He, Q.; Huo, L.; Wu, Y.; Parker, T. C.; Ma, W.; Sun, Y.; Wang, C.; Zhu, D.; Heeger, A. J.; Marder, S. R.; Zhan, X., High-Performance Electron Acceptor with Thienyl Side Chains for Organic Photovoltaics. *J. Am. Chem. Soc.* **2016**, *138* (14), 4955-4961.

145. Liu, Q.; Toudert, J.; Ciammaruchi, L.; Martínez-Denegri, G.; Martorell, J., High Open-Circuit Voltage and Short-Circuit Current Flexible Polymer Solar Cells Using Ternary Blends and Ultrathin Ag-Based Transparent Electrodes. *J. Mater. Chem. A* **2017,** *5* (48), 25476-25484.

146. Yan, C.; Barlow, S.; Wang, Z.; Yan, H.; Jen, A. K. Y.; Marder, S. R.; Zhan, X., Non-Fullerene Acceptors for Organic Solar Cells. *Nat. Rev. Mater.* **2018,** *3*, 18003.

147. Chandrabose, S.; Chen, K.; Barker, A. J.; Sutton, J. J.; Prasad, S. K. K.; Zhu, J.; Zhou, J.; Gordon, K. C.; Xie, Z.; Zhan, X.; Hodgkiss, J. M., High Exciton Diffusion Coefficients in Fused Ring Electron Acceptor Films. *J. Am. Chem. Soc.* **2019,** *141* (17), 6922-6929.

148. Li, T.; Chen, K.; Xin, J.; Hodgkiss, J. M.; Ma, W.; Chandrabose, S.; Xue, P.; Dai, S.; Zhou, K.; Zhan, X.; Liu, K., High-Performance Organic Solar Cells Based on Polymer Donor/Small Molecule Donor/Nonfullerene Acceptor Ternary Blends. *J. Mater. Chem. A* **2019,** *7* (5), 2268-2274.

149. Gautam, B. R.; Younts, R.; Carpenter, J.; Ade, H.; Gundogdu, K., The Role of FRET in Non-Fullerene Organic Solar Cells: Implications for Molecular Design. *J. Phys. Chem. A* **2018**, *122* (15), 3764-3771.

150. Eisenmenger, N. D.; Delaney, K. T.; Ganesan, V.; Fredrickson, G. H.; Chabinyc, M. L., Energy Transfer Directly to Bilayer Interfaces to Improve Exciton Collection in Organic Photovoltaics. *J. Phys. Chem. C* **2015,** *119* (33), 19011-19021.

151. Cnops, K.; Rand, B. P.; Cheyns, D.; Verreet, B.; Empl, M. A.; Heremans, P., 8.4% Efficient Fullerene-Free Organic Solar Cells Exploiting Long-Range Exciton Energy Transfer. *Nat. Commun.* **2014,** *5*, 3406.

152. Luhman, W. A.; Holmes, R. J., Investigation of Energy Transfer in Organic Photovoltaic Cells and Impact on Exciton Diffusion Length Measurements. *Adv. Funct. Mater.* **2011,** *21* (4), 764-771.

153. Scully, S. R.; McGehee, M. D., Effects of Optical Interference and Energy Transfer on Exciton Diffusion Length Measurements in Organic Semiconductors. *J. Appl. Phys.* **2006,** *100* (3), 034907.

154. de Mello, J. C.; Wittmann, H. F.; Friend, R. H., An Improved Experimental Determination of External Photoluminescence Quantum Efficiency. *Adv. Mater.* **1997,** *9* (3), 230-232.

155. Zhang, S.; Qin, Y.; Zhu, J.; Hou, J., Over 14% Efficiency in Polymer Solar Cells Enabled by a Chlorinated Polymer Donor. *Adv. Mater.* **2018,** *30* (20), 1800868.

156. Yuan, J.; Zhang, Y.; Zhou, L.; Zhang, G.; Yip, H. L.; Lau, T. K.; Lu, X.; Zhu, C.; Peng, H.; Johnson, P. A.; Leclerc, M.; Cao, Y.; Ulanski, J.; Li, Y.; Zou, Y., Single-Junction Organic Solar Cell with over 15% Efficiency Using Fused-Ring Acceptor with Electron-Deficient Core. *Joule* **2019**, *3* (4), 1140-1151.

157. Li, K.; Wu, Y.; Tang, Y.; Pan, M.-A.; Ma, W.; Fu, H.; Zhan, C.; Yao, J., Ternary Blended Fullerene-Free Polymer Solar Cells with 16.5% Efficiency Enabled with a Higher-LUMO-Level Acceptor to Improve Film Morphology. *Adv. Energy Mater.* **2019,** 9 1901728.

158. Fan, Q.; Wang, Y.; Zhang, M.; Wu, B.; Guo, X.; Jiang, Y.; Li, W.; Guo, B.; Ye, C.; Su, W.; Fang, J.; Ou, X.; Liu, F.; Wei, Z.; Sum, T. C.; Russell, T. P.; Li, Y., High-Performance As-Cast Nonfullerene Polymer Solar Cells with Thicker Active Layer and Large Area Exceeding 11% Power Conversion Efficiency. *Adv. Mater.* **2018,** *30* (6), 1704546.

159. Zhao, F.; Dai, S.; Wu, Y.; Zhang, Q.; Wang, J.; Jiang, L.; Ling, Q.; Wei, Z.; Ma, W.; You, W.; Wang, C.; Zhan, X., Single-Junction Binary-Blend Nonfullerene Polymer Solar Cells with 12.1% Efficiency. *Adv. Mater.* **2017,** *29* (18), 1700144.

160. Guo, B.; Li, W.; Guo, X.; Meng, X.; Ma, W.; Zhang, M.; Li, Y., High Efficiency Nonfullerene Polymer Solar Cells with Thick Active Layer and Large Area. *Adv. Mater.* **2017,** *29* (36), 1702291.

161. Lin, Y.; Zhao, F.; Prasad, S. K. K.; Chen, J. D.; Cai, W.; Zhang, Q.; Chen, K.; Wu, Y.; Ma, W.; Gao, F.; Tang, J. X.; Wang, C.; You, W.; Hodgkiss, J. M.; Zhan, X., Balanced Partnership between

Donor and Acceptor Components in Nonfullerene Organic Solar Cells with >12% Efficiency. *Adv. Mater.* **2018**, 30, 1706363

162. Kwon, O. K.; Uddin, M. A.; Park, J.-H.; Park, S. K.; Nguyen, T. L.; Woo, H. Y.; Park, S. Y., A High Efficiency Nonfullerene Organic Solar Cell with Optimized Crystalline Organizations. *Adv. Mater.* **2016,** *28* (5), 910-916.

163. Mihailetchi, V. D.; Wildeman, J.; Blom, P. W. M., Space-Charge Limited Photocurrent. *Phys. Rev. Lett.* **2005,** *94* (12), 1-4.

164. Cowan, S. R.; Roy, A.; Heeger, A. J., Recombination in Polymer-Fullerene Bulk Heterojunction Solar Cells. *Phys. Rev. B: Condens. Matter Mater. Phys.* **2010,** *82* (24), 1-10.

165. Wiesenhofer, H.; Beljonne, D.; Schales, G. D.; Hennebicq, E.; Brédas, J. L.; Zojer, E., Limitations of the Förster Description of Singlet Exciton Migration: The Illustrative Example of Energy Transfer to Ketonic Defects in Ladder-Type Poly(para-phenylenes). *Adv. Funct. Mater.* **2005,** *15* (1), 155-160.

166. Scholes, G. D., Long-Range Resonance Energy Transfer in Molecular Systems. *Annu. Rev. Phys. Chem.* **2003,** *54* (1), 57-87.

167. Liu, X.; Yan, Y.; Honarfar, A.; Yao, Y.; Zheng, K.; Liang, Z., Unveiling Excitonic Dynamics in High-Efficiency Nonfullerene Organic Solar Cells to Direct Morphological Optimization for Suppressing Charge Recombination. *Advanced Science* **2019,** *6* (8), 1802103.

168. Gupta, V.; Bharti, V.; Kumar, M.; Chand, S.; Heeger, A. J., Polymer-Polymer Förster Resonance Energy Transfer Significantly Boosts the Power Conversion Efficiency of Bulk-Heterojunction Solar Cells. *Adv. Mater.* **2015**, 27, 4398-4404.

169. Burkhard, G. F.; Hoke, E. T.; McGehee, M. D., Accounting for Interference, Scattering, and Electrode Absorption to Make Accurate Internal Quantum Efficiency Measurements in Organic and Other Thin Solar Cells. *Adv. Mater.* **2010**, 22, 3293-3297.

Acknowledgements

훌륭한 과학자가 되리라는 꿈을 안고 UNIST에 온 지 벌써 7년이 흘렀고 마침내 박사 학위를 받게 되었습니다. '연구'라는 행위는 저에게 너무 낯설었고, 학부 시절 배웠던 전공 공부와 실험을 하는 것은 전혀 다른 일이었습니다. 그래도 다행히 실험을 하는 것은 재미가 있었고, 많은 교수님들 그리고 연구실 선배, 후배들의 도움과 조언 덕분에 무사히 학위 과정을 마칠 수 있었던 것 같습니다.

먼저 저를 자립적인 연구자로서 잘 성장할 수 있게 7년 동안 지도해주신 김진영 교수님께 감사의 말씀을 전합니다. 제가 일을 마무리하는 것이 서툴러서 분명 많이 답답하셨을 텐데 항상 내색 않으시고 함께 문제 해결에 대해 고민해주시고 잘 마무리하도록 끝까지 믿어 주셔서 너무나 감사했습니다. 교수님의 믿음 덕분에 제가 포기하지 않고 끝까지 올 수 있었던 것 같습니다. 이 글을 빌어 교수님께 존경한다는 말씀 전하고 싶습니다.

그리고 항상 논문을 꼼꼼하게 봐주셨던 현재 경희대에 계시는 Bright Walker 교수님께 감사의 인사 전하고 싶습니다. 임팩트가 적은 연구도 본인 일처럼 적극적으로 도와주시고, 용기를 북돋아 주셔서 주눅들지 않고 일들을 하나 하나씩 잘 마무리할 수 있었습니다. 바쁘신 와중에도 학위 논문을 심사 해주시고 잘 마무리할 수 있도록 도와주신 송명훈 교수님, 권태혁 교수님, 서정화 교수님께도 감사드리며, 학위 기간의 절반 이상을 함께 공동 연구를 하면서 많은 가르침 주신 고려대 우한영 교수님께도 감사드립니다. 학부 시절, 졸업을 6개월 앞두고 졸업 논문을 쓰고 싶다는 저의 무리한 부탁에도 흔쾌히 지도해주시고, 너무나 좋은 연구실을 소개해주신 울산대 조신욱 교수님께도 감사드립니다.

우리 연구실, NGEL 멤버들에게도 감사의 인사 전하고 싶습니다. 1, 2년차 일 때 정말 다양한 실험들을 하면서 연구 스펙트럼을 넓힐 수 있게 해주신 현재 강원대에 계시는 김성범 교수님, 연구실 생활 잘 적응할 수 있게 많이 도와주시고 챙겨 주신 효성 오빠, 기환 오빠, 서진 오빠, 명희 언니 다들 너무 감사합니다. 그리고 학위 기간 동안 함께 동고동락하면서 여러가지로 많이 도와주시고 힘들 때 커피 타임 가지면서 같이 지낸 선배-동료들, 많은 걸 알려주신 태효 오빠, 항상 편하게 해주시는 재기 오빠, 옆자리에서 함께 지냈던 학범 오빠, 배울 점이 많고 저의 자존감을 지켜 주시는 혜림 언니, 분위기를 항상 밝게 만들어 주시고 힘들 때 의지가 됐던 세영 언니, 같이 논문 2개나 쓴 착하고 똑똑한 정우, 만년 막내 착한 영진이에게 감사의 인사 전합니다. 박사 마지막 년도에 정말 많은 도움 주셨던 송수희 박사님께도 감사드립니다. 그리고 저를 많이 도와주었던 나경이, 강택 오빠, 재원이, 형수, 윤섭이, 혜원이 덕분에 즐겁고 조금 더 편하게 연구할 수 있었습니다. 모두 고맙고, 떠오르는 샛별들 종득씨, 지우, 우진, 찬범, 도훈, 현서, 중건이, 진희 다들 열심히 해서 좋은 논문 많이 쓰길 바랍니다. 화이팅!

함께 공동연구를 했던 고려대 OOML의 Yuxiang, Afsar, 화숙, Ziang, 동아대의 유정이, 함께 박사 과정을 하면서 서로 힘이 되어 주었던 울산대 수정이에게도 감사 인사 전합니다.

소중한 저의 친구들 예슬이, 정하 그리고 09물리 수정이, 선희, 세연이, 성아, 혜민이, 지혜, 지원이 모두 응원해주고 격려해줘서 고맙습니다.

저희 친척들, 외할머니, 외할아버지, 이모, 이모부, 삼촌들, 숙모들, 큰어머니, 큰아버지, 작은아버지, 고모들, 사촌 오빠, 언니, 동생들 저를 응원해 주셔서 감사하고, 특히 제가 대학교, 대학원 진학할 때 많은 조언 주시고 관심 가져 주신 막내 외삼촌에게 감사드립니다.

그리고 대학원 생활 내내 함께 연구실 생활하면서 많이 의지가 되었고, 항상 저를 챙겨주고 아껴주는, 사랑하는 택호에게 감사 인사 전합니다.

마지막으로 제가 무엇을 하든 항상 믿어 주시고 적극적으로 지지해 주시는 사랑하는 우리 엄마, 아빠 그리고 동생 혜림이 모두 진심으로 감사합니다.

많은 분들의 도움 덕분에 학위를 받게 된 것 같습니다. UNIST에서의 좋은 경험을 밑거름으로 하여 항상 겸손한 마음으로 정진하겠습니다. 다시 한 번 모든 분들께 감사드립니다.